Master's thesis

NTNU
Norwegian University of Science and Technology
Faculty of Natural Sciences
Department of Materials Science and Engineering

Simen Skurdal

Characterization of Aluminium TiC nano-composite filler wire inoculated weld metal

Master's thesis in Materials science and engineering
Supervisor: Jens Christofer Werenskiold
Co-supervisor: Geir Kvam-Langelandsvik and Tor Inge Thorsen
June 2023

NTNU
Norwegian University of
Science and Technology

Simen Skurdal

Characterization of Aluminium TiC nano-composite filler wire inoculated weld metal

Master's thesis in Materials science and engineering
Supervisor: Jens Christofer Werenskiold
Co-supervisor: Geir Kvam-Langelandsvik and Tor Inge Thorsen
June 2023

Norwegian University of Science and Technology
Faculty of Natural Sciences
Department of Materials Science and Engineering

NTNU
Norwegian University of
Science and Technology

Preface

The research presented in this Master's thesis was conducted at the Department of Materials Science and Engineering (IMA) at the Norwegian University of Science and Technology (NTNU) during the spring semester of 2023.

First, I want to thank my main supervisor Assoc. Prof. Jens Christofer Werenskiold (NTNU), as well as my co-supervisors Dr. Geir Kvam-Langelandsvik (SINTEF) and PHD candidate Tor Inge Thorsen (IFY) for their invaluable assistance and enthusiasm for the duration of the project period. A special thanks to Tor Inge for the numerous hours spent to help out with the experimental parts of the work. I would also like to thank senior engineers at IFY: Emil Frang Christiansen and Bjørn Gunnar Soleim for their helpful tutorials at NORTEM labs. I would also like to thank NTNU Nanolab for the access and usage of their equipment.

Last, but not least, thanks to all of my classmates for making the everyday student life a lot more enjoyable.

Simen Skurdal
NTNU, Trondheim
June 2023

Abstract

The recently developed production method metal screw extrusion (MSE), has shown to be a viable method for producing nano-composite filler wires (FWs). AA1370 FW containing TiC nanoparticles (NPs) supported by titanium (Ti) powder has been produced via MSE. These have been used to arc-weld sheets of AA1050-H14. During previous work this has shown to strongly grain refine the weld metal (WM). During this work, site specific focused ion beam (FIB) transmission electron microscope (TEM) lamellas were produced. These were characterized using different transmission electron microscopy techniques, with a special focus on nucleation mechanism and TiC NP distribution, in addition to their effect on grain refinement.

The TiC NPs were found to generally be distributed along grain boundaries (GBs) and the α-Al grains had nucleated on large $TiAl_3$ particles found in the centers of grains. The large $TiAl_3$ particles are thought to have formed on smaller $TiAl_3$ particles precipitated in the melt and grown supported by the high concentration of solute Ti at the solidifying front. The grain refining effect can be attributed to a combination of the segregating effect of Ti, precipitation of $TiAl_3$ particles in the melt creating ideal nucleation sites for α-Al, and the growth restricting effect of the TiC NPs.

Sammendrag

Den nylig utviklede produksjonsmetoden metall skruekstrudering har vist seg å være en mulig metode for å produsere nano-kompositt fylltråder. AA1370 fylltråd som inneholder TiC nanopartikler støttet av titan pulver er blitt produsert via skruekstrudering. Disse har blitt brukt til å lysbuesveise plater av AA1050-H14. Tidligere arbeid har vist at dette forfiner sveisemetallet godt. I løpet av dette arbeidet ble det produsert lameller av utvalgte områder ved hjelp av et fokusert ionestrålesystem for transmisjonselektronmikroskopi. Disse ble karakterisert ved hjelp av ulike teknikker for transmisjonselektronmikroskopi, med spesielt fokus på nukleasjonsmekanismer og fordelingen av TiC nanopartikler, samt deres effekt på kornforfining.

TiC nanopartikler ble generelt funnet å være fordelt langs kornegrensene, og α-Al-kornene hadde nukleert på store $TiAl_3$-partikler som ble funnet i midten av kornene. De store $TiAl_3$-partiklene antas å ha blitt dannet på mindre $TiAl_3$-partikler som ble presipitert i smelten og vokste ved hjelp av den høye konsentrasjonen av Ti løst i smelten ved grenseflaten smelte/solid. Kornforfiningseffekten kan tilskrives en kombinasjon av den segregerende effekten av Ti, presipitering av $TiAl_3$-partikler i smelten som skaper ideelle nukleeringspunkter for α-Al, og den veksthemmende effekten av TiC nanopartikler.

Table of Contents

1 Introduction

Welding of heat treatable high strength aluminum (Al) alloys, the 2xxx-, 6xxx- and 7xxx-series is a process with well known difficulties. Particularly at peak strength (T6 condition) they exhibit very low arc-weldability. Thus, the joining and assembling of larger components of these alloys becomes a difficult and costly process due to the need of using other joining techniques such as riveting, bolting, friction stir welding or laser beam welding [1]. For complex structures, arc-welding might even be the only possible joining method [2]. This has effectively limited any large-scale implementation of these alloys as light-weight structural materials. New, lighter options for use as structural materials is a must in order to reduce the emissions and energy consumption particularly in the transport and aerospace sector [3, 4, 5]. These Al alloys may offer a solution with regards to their high strength-to-weight ratio and low cost, if the difficulties with arc-welding can be circumvented.

The low weldability of these alloys is generally due to two factors: (1) Dissolution or overaging of strengthening particles in the heat affected zone (HAZ), and (2) A high susceptibility to hot-cracking (WM cracking during solidification). The weakness suffered in the HAZ can ruin the mechanical integrity of a structure and may be close to impossible to recover during post welding heat treatments in complex structures [6]. Perhaps the most important factor for determining the susceptibility to hot-cracking is the microstructure of the WM. As small, equiaxed grains is preferable over large columnar ones, achieving sufficient grain refinement in the WM is crucial. A way of achieving this effect is by adding grain refiners to the FW.

The use of ceramic NPs for grain refining and strengthening of light-weight metals has gained attention lately [7, 8, 9], forming so-called metal matrix nano composites (MMNCs). Amongst the most promising particles of use is TiC NPs [2, 10]. In general, the most important factor determining the effect of the ceramic NPs is how uniformly dispersed they are. Because of this, the successful production of MMNC FWs has previously proved difficult. However, recently developed methods such as accumulative roll bonding, and in-situ salt-melt reaction has made the production of such FWs viable [11, 12, 13].

The MSE process patented by Werenskiold et al. [14] in 2008, is a relatively new and an interesting candidate for producing MMNC FWs. Compared to other alternatives, it is a cost- and energy effective method. Recently, a work by Langelandsvik [15] utilized a prototype situated at NTNU to successfully produce Al metal matrix composite (MMC) FWs. This was followed by another work by Langelandsvik et al. [16], proving its viability of producing Al MMNC FWs.

Building on this, a previous masters thesis by Kirkbakk [17] investigated the efficiency of different grain refining particles in FWs produced by MSE. Amongst these particles, TiC NPs were found to be very effective grain refiners. During EDS scans in a SEM, some carbon (C) signals were found in the centers of $TiAl_3$ particles located in centers of and thought to have nucleated α- Al grains. Thus, the TiC NPs were proposed as nucleation cites for the $TiAl_3$ particles which in turn nucleated the α-Al grains. Though no conclusive evidence was found and investigations in a transmission electron microscope (TEM) was the proposed solution. The Al TiC NP welded samples which were produced will be used in this work to produce FIB site specific TEM samples. These samples will then be characterized in a TEM with a special focus on the grain refining effect of TiC NPs, the nucleation mechanism and the distribution of different particles found in the sample. The finds will be compared to relevant literature.

2 Theory

2.1 Aluminium arc-welding and microstructure

The microstructure in WM resulting from Al arc-welding usually has a very distinct pattern which can be divided into the columnar zone and the equiaxed zone. The columnar zone is found at the fusion boundary and consists of columnar dendrites growing in parallel to the maximum temperature gradient. The growth and resulting size of the dendrites can be restricted by nucleation and growth of new grains. Thus, the higher extent of nucleation, the more refined the resulting grain structure [18].

Such a refined, equiaxed microstructure yields a stronger weld and lessens the risk of solidification cracking, as was proven by Schempp et al. [19] for Al alloy A1050. It was performed by casting ingots with additions of grain refiner which were subsequently machined into weld coupons and then welded by tungsten inert gas (TIG) welding. Through an addition of grain refiner Al Ti_5B_1, the mean grain size in the WM was reduced by 86%, and the microstructure changed from columnar to equiaxed. On the other hand, this work looks into the addition of grain refiner through the filler wire, a method that will be explained in further detail in the following sections.

2.1.1 MIG welding

Metal inert gas welding (MIG), also known as gas metal arc-welding (GMAW), is an arc-welding process in which a continuously fed wire is utilized as both filler metal and electrode. All while the arc and the weld pool is shielded by an inert gas. MIG welding is the most widely used manual arc-welding process for the joining of aluminium. This is due to several advantageous capabilities such as high welding speeds, smaller heat affected zone (HAZ) than for TIG welding, excellent oxide film removal while welding, and its dynamic, all-positional welding [6].

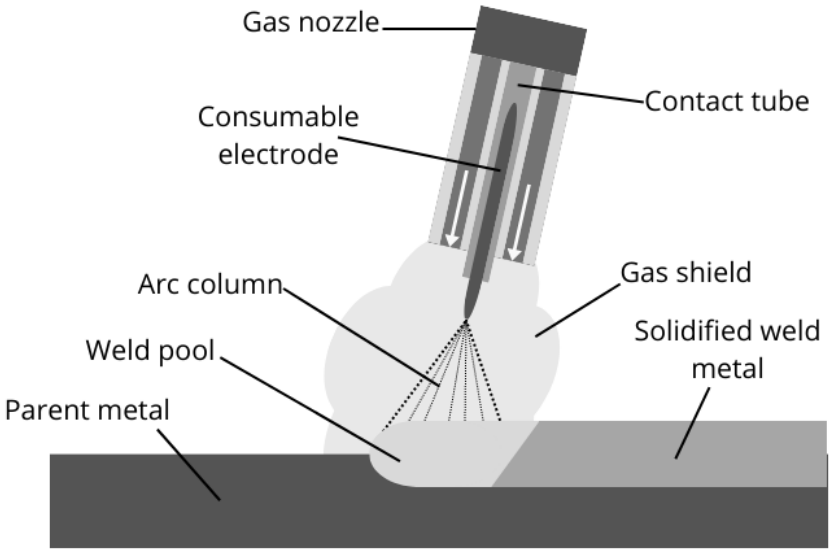

Figure 1: Conceptual sketch showing the fundamental features of the MIG process. Figure adapted from Mathers [6].

The largest part of the heat development in the arc occurs at the positive pole, which is the electrode (FW), in the case of MIG welding. This gives a high wire burn-rate, yielding an efficient transfer of heat through the FW into the weld pool. There are two modes for which metal can be transferred from wire to weld pool, dip transfer mode and spray transfer mode. When using dip transfer mode, low welding currents are applied, which results in the tip of the FW not being melted sufficiently fast to maintain the arc. However, the wire will dip into the weld pool and short-circuit, causing the wire to melt. The effects of surface tension will the draw this molten metal into the weld pool. Subsequently, the arc re-establishes and the cycle is repeated. This method does however have its downsides, if the welding parameters are sub-optimal, it might lead to excessive spattering and lack-of-fusion defects due to the low heat input. In spray transfer mode, a higher welding current is applied. This effectively melts the metal at the wire tip, transferring it across the arc as small molten droplets. This yields far lower spattering and deeper penetration into the parent metal compared to dip transfer mode. Also, due to the low melting temperature of Al, spray transfer is possible at relatively low current, while still achieving a joint free of spatter [6].

2.1.2 TIG welding

Tungsten inert gas (TIG), also known as gas tungsten arc-welding (GTAW), is an arc-welding process in which a non-consumable tungsten electrode is utilized. The welding arc is the only heat source and an inert gas is used to shield both the arc-column, weld pool and electrode. The application of FW is optional. It is capable of sustaining a stable arc at very low welding currents. This enables the possibility of welding very thin components and the production of very high quality WM. Though, in order to acquire the very best results, a highly skilled welder is required. However, compared to MIG welding, the TIG process does not achieve the same depth of penetration into the parent metal, while also having difficulties penetrating into corners [6].

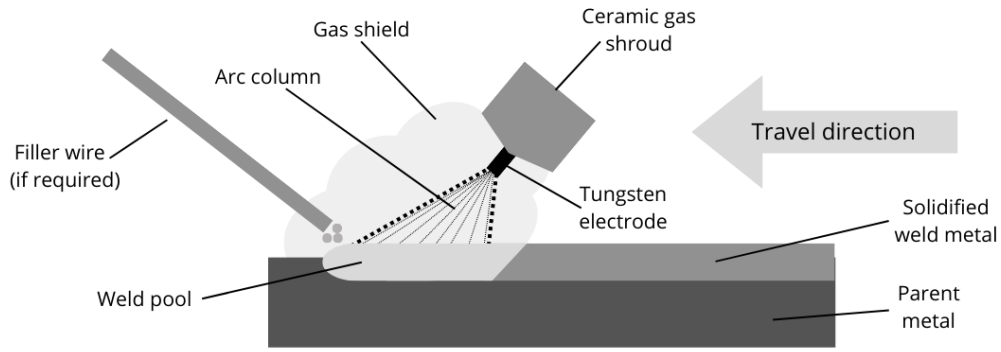

Figure 2: Conceptual sketch showing the fundamental features of the TIG process. Figure adapted from Mathers [6].

TIG welding is usually performed using alternating current. As when using direct current, neither direction is optimal. When the electrode is connected to the negative pole, the applied polarity does not result in sufficient oxide removal. When it is connected to the positive pole, which is also where the bulk heat is generated, the electrode becomes overheated and melts. Thus, by applying an alternating current, the oxide film removal is performed during the electrode positive half-cycle and electrode cooling and weld bead penetration during the electrode negative half-cycle. For every time the AC sine wave passes through zero, the arc extinguishes and reignites [6].

2.1.3 Porosity

Porosity is a defect arising from gas dissolved in the molten WM becoming trapped as it solidifies. The produced pores has sizes which can range from extremely fine micro-porosity to being at the millimeter-scale. For Al, hydrogen (H) gas poses the largest issue. This is due to the solubility of H in molten Al being approximately 20 times higher than in solid Al. This causes the production of porosity-free welds of Al to be rather challenging, as extensive shielding with an inert gas through-out the process is required from the production of FW to the welding itself. Comparing MIG and TIG welding, TIG produces the lowest level of porosity [6].

Throughout the process, many possible sources of H exists. The shielding gas might be contaminated with moisture which will decompose in the arc forming H gas. Therefore, it is important to use a gas of high purity with a dew point ideally less than -50^{o}C. Another possible source is the FW which might be carrying a hydrated oxide layer and H-forming compounds such as grease on the surface. It should therefore be degreased, and ideally shaved to remove the oxide layer in addition to any contaminants that may be pressed into the surface. Yet another possible source is the parent metal, which might also carry a hydrated oxide layer and H-forming compounds, and should therefore ideally be treated similarly to the FW [6].

2.2 Nucleation in welding

2.2.1 Heterogeneous nucleation

The first observation of weld pool heterogeneous nuclei was made in a 1986 work by Kou and Le [18]. In their work they discussed three different mechanisms of WM nucleation and grain refinement: dendrite fragmentation, grain detachment and heterogeneous nucleation. The only mechanism that will be discussed further in this work is heterogeneous nucleation. Though, it is worth noting that achieving some grain refinement of the WM is possible without the addition of inoculants. According to classical nucleation theory, the free energy barrier that must be overcome for nucleation on heterogeneous substrates, will follow the equation: [20]

$$\Delta G_n^0 = (\frac{16\pi}{3})(\frac{\sigma^3}{\Delta s_t \Delta T^2}) f(\Theta) \tag{1}$$

Where σ is the new surface energy, Δs_t, the fusion entropy, ΔT^2, the undercooling below liquidus temperature and Θ, the wetting angle between the liquid phase and the heterogeneous nucleation substrate. St. John et al. [21] noted in their work that successful nucleation depended on both the generation of sufficient undercooling and the potency and distribution of heterogeneous nucleant particles.

2.2.2 Constitutional undercooling

In a work investigating grain refined castings, Easton and St. John [22] stated that there can be at least two mechanisms of grain refinement, with the most relevant for this work being the model of constitutional undercooling in the bulk melt. Constitutional undercooling results from solute segregation at the liquid/solid interface of alloys. Due to the resulting compositional difference between the liquid and the initially formed solid, a re-distribution of solute in the liquid occurs. As such, a diffusional zone ahead of the solidification front enriched with solutes is formed. As illustrated in figure 3, for hypo-eutectic alloys this diffusional zone locally lowers the liquidus temperature, T_l. When the actual temperature in the area, T_q, which is governed by temperature gradient, G, becomes lower, the area becomes constitutionally undercooled, ΔT_c. If a nucleating particle is in this area, it will act as a heterogeneous nucleation point if the constitutional undercooling, ΔT_c exceeds the activation temperature of the nuclei, ΔT_N. Thus, if a sufficient amount of potent particles is present in the melt, repeated nucleation events will occur in the weld pool, effectively refining the microstructure.

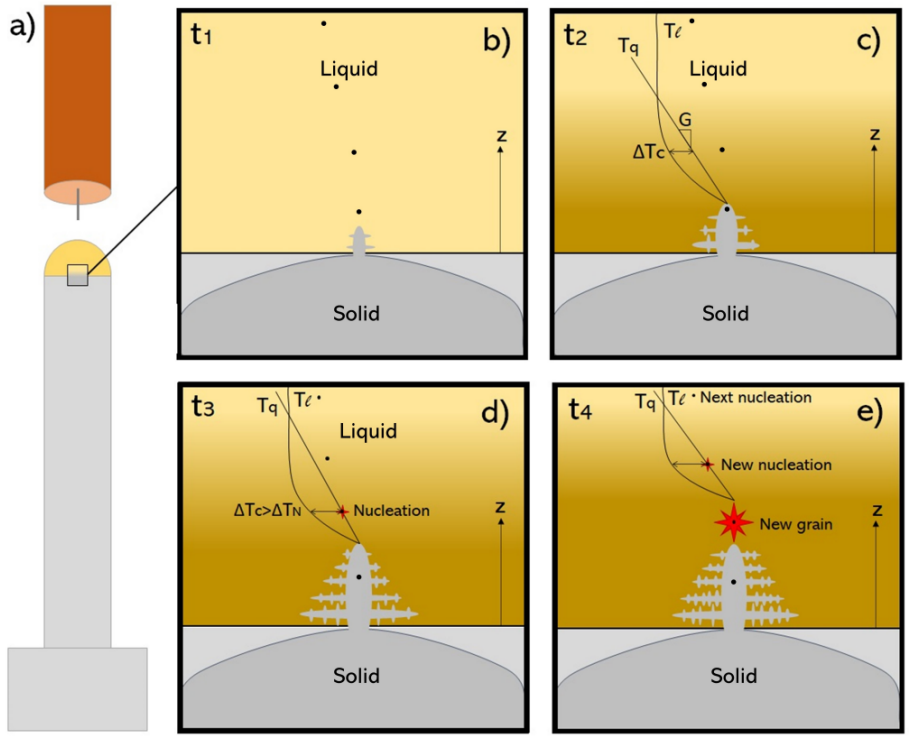

Figure 3: Schematic illustration of epitaxial growth, development of the constitutionally undercooled zone and the heterogeneous nucleation during solidification. (a) Showing a solidification front with solid in grey and liquid in yellow. (b) Showing a newly formed dendrite in the melt grown epitaxially from the solid. (c) Showing the formation of a constitutionally undercooled zone resulting from solute re-distribution. (d) Showing heterogeneous nucleation of a new grain. (e) Showing growth of the new grain and development of a new constitutionally undercooled zone ahead of it. Reprinted from Langelandsvik [15].

To quantify the effect of solute on the grain size of castings, two parameter were considered: the growth restriction factor, Q, which is a measure of how rapidly the constitutionally undercooled zone is formed at the earliest stages of growth:

$$Q = m_l c_0 (k - 1) \tag{2}$$

and the supercooling parameter, P, which equals the amount of constitutional undercooling that can be generated:

$$P = m_l c_0 (k - 1) k \tag{3}$$

where m_l is the gradient of the liquidus slope, c_0 is the concentration of the solute in a binary alloy and k is the partition coefficient.

The basis of both is found by assuming the thermal gradient being zero and there being no thermal undercooling, the maximum constitutional undercooling, ΔT_c can be found by:

$$\Delta T_c = m_l (c_0 - c_l) \tag{4}$$

where c_l is the composition of the solute element in the liquid phase.

By substituting in the Scheil equation,

$$c_l = c_0(1 - f_s)^p \tag{5}$$

Where p=k-1, and f_s is the fraction solid. Into equation 4 and differentiate at f_s=0, Q is obtained.

By substituting in the Lever rule,

$$c_l = c_0(1 - (1 - k)f_s) \tag{6}$$

Into equation 4, and set f_s=1, P is obtained.

Further, a new parameter f_{sn} was defined as being f_s at which further nucleation occurs. Thus this parameter is related to the size a grain will grow to before a subsequent nucleation event occurs. The grain size of the final microstructure is determined by the distance between nucleation events. To compare and determine the effect of solute content and additions on the grain size, a new term, relative grain size(RGS) was defined as the fraction solid, f_{sn}, at which ΔT_c reaches ΔT_n. By substituting into equation 4 and solving for f_{sn}, an expression for RGS in obtained:

$$RGS = f_{sn} = 1 - m_l c_0 m_l c_0 - \Delta T_n^{1/p} \tag{7}$$

This equation is applicable for any binary alloy system. Though it does not take into account latent heat and thermal gradients.

2.3 Ti/TiC nanoparticles as grain refiner

The use of ceramic particles as a means of grain refining metals, forming MMCs, is a well known strengthener for light-weight metals [7, 8, 9]. However, with higher concentrations of ceramic particles the ductility of these MMCs deteriorate [23]. Thus, the use of ceramic NPs has gained attention as a means of bypassing the problem, forming MMNCs. The defining factor for the performance of these MMNCs is how uniformly the NPs are distributed, which can be rather difficult to achieve. Especially in a casting process, as the general poor wettability between metal and ceramic complicates the goal of acquiring a uniform distribution of ceramic particles in the metal matrix [24]. In this work however, the MSE process(described in the next section) is used to produce MMNC filler wire.

The possibility of using TiC as Al grain refiner was first postulated by Cibula as early as 1949 [25]. However, Al-Ti-C master alloys for grain refinement was not successfully produced until the mid 1980s by Banerji and Reif [26]. It has since gradually gained interest due to the more widely used Al-Ti-B grain refiner being prone to boride agglomeration in addition to poisoning by elements as Zr, V and Cr [27].

Still, the exact nucleation mechanism of α-Al on TiC is a bit disputed. Experimental observations by Wang et al. [28] found chrysanthemum-like structures of Ti segregates surrounding TiC particles located in the center of grains. This pointed to an excess of Ti being vital for the occurrence of

nucleation. Yu and Liu [27] further investigated this phenomenon for rapid solidification. The observations made in their work, provided the basis for the proposal of a new nucleation theory termed the Ti transition zone theory. It suggests that when Al-Ti-C is added to pure Al in liquid form, a Ti transition zone forms at the interface of TiC. This serves as an ideal prenucleus on which α-Al can nucleate. The Ti transition zone will then transform to the chrysanthemum-like structures observed in solid state.

The solute effects of Ti has been widely researched regarding its role in grain refining [29, 30, 31]. Solute elements such as Ti segregate to the inoculant/melt interface which affects the growth of dendrites in addition to affecting the constitutional undercooling at the solid/liquid interface. The segregating power of a solute element can be described by the growth restriction factor, Q shown in equation 2, and the segregating power of Ti in Al is very high. Li et al. [29] suggested that the powerful segregating effect of Ti creates a strongly undercooled zone in front of the growing interface where nucleation can occur on nucleants present. Kashyap et al. [30] even concluded that the duplex nucleation theory of $TiAl_3$ layers forming on borides could be inconsequential as solute Ti anyway is required for nucleation to occur.

A 2021 study by Liu et al. [32] investigated the grain refinement by TiC-TiH_2 inoculation in selected area melted AA2025. The observed grain refining effect was mainly attributed to fine $TiAl_3$ particles precipitating in the melt and nucleating α-Al. The nucleation mechanism was suggested to most likely follow the Ti transition zone theory. In a 2005 crystallographic study, Zhang et al. [33] applied the edge-to-edge matching crystallographic model to study and predict the efficiency of nucleating substrates in Al-based alloys. They found atom matching between $TiAl_3$ and α-Al occurring in the closest packed directions and on closest packed planes in terms of the orientation relationships. Interatomic spacing misfit along matching directions, and interplanar spacing mismatch between matching planes were both found to be very small for the predicted orientation relationships. From a crystallographic point of view it was concluded that $TiAl_3$ was a more effective grain refiner than TiC and TiB_2 for α-Al.

A newer study conducted by Zhao et al. [34] investigating the grain refining effect of a Al-Ti-C master alloy rich in TiC NPs on a 7050 alloy. They attributed the prominent grain refining effect to a combination of heterogeneous nucleation and the growth restriction effect. The TiC particles showed a clear inclination of distributing along the GBs rather than within the grain matrix during solidification. As such, the growth restriction effect stood out as the most decisive effect. This is due to the NPs amassing at the growth interfaces of the newly formed phases during solidification. These serve as a barrier, physically inhibiting the transfer of solute atoms. This conclusion is also supported by a 2016 study by Wang et al. [35] investigating inhibition of growth of primary aluminum in Al-Si10 using NPs. They found the majority of the TiCN NPs to distribute along GBs forming layers which inhibit grain growth. While some were found within both the primary aluminum and the eutectic phase.

Both studies assume that the TiC NPs to some extent played the role as heterogeneous nucleation sites. Due to the orientation relationship between TiC and α-Al, TiC particles possess a high potency for nucleation. This is however a rather difficult hypothesis to prove, simply due to the size of the particles and sensitivity of the equipment required to do so. It is also virtually impossible to disprove in practice due to the promising theoretical evidence.

Two sets of work from 2019 by Sokoluk et al. [2] and Zou et al. [36] investigated the effect of TiC nano-treated FW on the weldability of AA7075. They found it to refine the microstructure to small equiaxed grains, which would remain almost the same even after heat treatment. They suggested a solidification process where the TiC NPs would first act as heterogeneous nucleation sites for α-Al. They would then act as physical barriers for the solidifying front and restrict the growth of grains. Finally they would modify the secondary, eutectic phases from continuous to fine dispersed features.

A similar work by Murali et al. [37] investigated the viability of using TiC nano-treated FW to enable arc-welding of Al alloys with traditionally low arc-weldability. The TIG welded AA2024, AA5083, AA6061 and AA7075 samples all exhibited no defects such as hot cracks and the homogeneous WM microstructures contained small, spherical grains. They attributed the effect to the weld pool liquid being able to maintain a higher degree of undercooling which promotes a continuous formation of new α-Al grains. The effective nucleation and growth restriction by TiC NPs promoted the small grains.

2.4 Metal screw extrusion

MSE is a relatively new process developed as a collaboration project between NTNU and Norsk Hydro ASA. This culminated in a patent issued in 2008 by Werenskiold et al. [14]. It is a process for continuous extrusion of high viscosity materials like Al and its alloys. A prototype screw extruder has since been situated at NTNU in Trondheim and has been subject to continuous modification and improvement through various studies.

The screw extruder consists of an Archimedes screw inside a screw housing, an inlet for feeding material, an extrusion chamber and a die forming the shape of the extruded product. The basic principle of the extruder is that feeding material is continuously fed into the screw housing where the Archimedes screw transports it towards the extrusion chamber. The material will there be consolidated and heated in the preheated extrusion chamber, and extruded through the die opening at the end of the extrusion chamber. A conceptual sketch of the process is shown in figure 4 below.

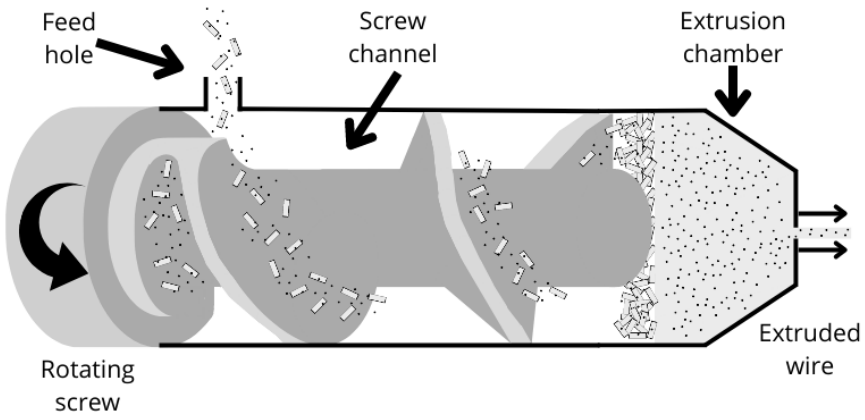

Figure 4: Conceptual sketch of the screw extrusion process illustrating feeding of material which is transported forward by a single flight screw, consolidation in the extrusion chamber and extrusion. Adapted from Langelandsvik [15].

Due to the deformation characteristics and material flow in the screw extrusion process, a high degree of mixing occurs in the consolidated region, as has been shown by Widerøe and Welo [38]. Therefore, the process is rather suitable for mixing particles into the extruded profile. This was first proven by Skorpen et al. [39] in 2014, mixing AA6063 and magnesium granules. It has later been shown by Langelandsvik [40, 16], as a viable method for mixing TiC NPs into Al FW.

2.5 Transmission Electron Microscope(TEM)

2.5.1 Interaction of electrons with matter

Several different signals are created when the incident electron beam hits and interacts with the sample. The most used and important terms for differentiating these electron-scattering phenomena are elastic and inelastic. These terms are defined by whether or not the scattered electrons lose energy. In either case, both the incident electrons and the atoms in the sample can be considered being particles. A sufficient analogy for the scattering of these incident electrons is as one billiard ball colliding with another [41].

Another way to differentiate the scattered electrons is as coherently and incoherently scattered, though there are some correlation with the elastic and inelastic scattering. This way of thinking takes the wave-like nature of electrons into consideration. Coherently scattered electrons remain in phase with one another and has a fixed wavelength, which is also how elastically scattered electrons usually behave. Incoherently scattered electrons have no phase relationship, which is also how inelastically scattered electrons usually behave [41].

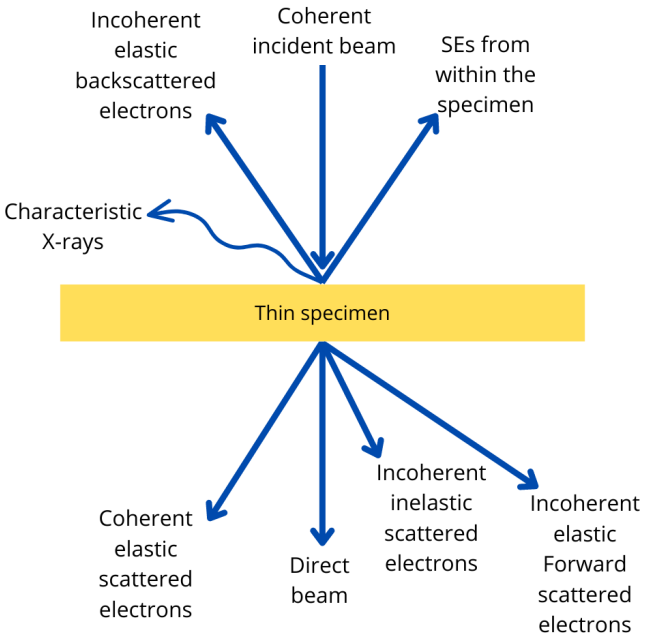

Figure 5: The different kinds of electron signals generated when the high energy electron beam hits a thin specimen. Adapted from Williams and Carter [41].

The scattered electrons exit the specimen at different angular distributions with respect to the direct beam. This gives rise to another set of terms, forward scattered and backscattered electrons (BSEs). If an electron is scattered at an angle less than 90^o, it is considered forward scattered. If an electron is scattered at an angle more than 90^o, it is considered backscattered [41].

The scattering probability can be explained by looking at a certain cross section of the specimen. The electrons are first accelerated, forming the high energy electron beam. They reach electron energies of 100-400 keV before hitting the specimen. The cross section it interacts with in the specimen can be considered to contain N atoms/unit volume. Each of these N atoms have a cross section defined by the effective radius (r has different values for each scattering process) of each respective single electron, r [41].

$$\sigma_{atom} = \pi r^2 \tag{8}$$

From this we can elucidate the total cross section for scattering as σ_{total} in m $^{-1}$.

$$\sigma_{total} = N\sigma_{atom} \tag{9}$$

In addition, N=$N_0\rho$/A, so the equation can be rewritten as

$$\sigma_{total} = \frac{\sigma_{atom} N_0 \rho}{A} \tag{10}$$

Where N_0 is Avogadros number, A is the atomic weight of the scattering atoms in the specimen and ρ is the density of the same scattering atoms.

As σ_{total} is the number of scattering events per the distance the electron travels through the specimen, then the probability of scattering from a specimen of thickness t, is given by

$$\sigma_{total}t = \frac{\sigma_{atom}N_0\rho t}{A} \tag{11}$$

2.5.2 Diffraction

Diffraction is a term used to describe a special form of elastic scattering of waves. The wave-like nature of electrons was first theorized by Louis de Broglie in 1925, by showing the correlation between the wavelength of electrons and their energy, E: [42]

$$\lambda = \frac{1.22}{E^{1/2}} \tag{12}$$

However, the TEM produces very high electron energies, causing the electrons, considered particles, to reach velocities greater than half the speed of light. As such, the equation must be modified to take into account the relativistic effects: [41]

$$\lambda = \frac{h}{[2m_0eV(1+\frac{eV}{2m_0c^2})]^{1/2}} \tag{13}$$

Where h is Plancks constant, m_0 is the rest mass of an electron, e is the elementary charge of an electron, V is the accelerating voltage and c is the speed of light in a vacuum.

In 1913, the father-son team of Sir William H. Bragg and W. Lawrence Bragg proposed the idea that waves reflected off adjacent scattering centers, as shown in figure 6, would need to have a path difference equal to an integer number to remain in phase. In other words, the path difference between an electron wave reflected from the upper, and an electron wave reflected from the lower plane in figure 6 is equal to (AB + BC). As the upper and lower hkl planes are spaced by a distance d, and knowing the incident wave and reflected wave entering and leaving at angle Θ_B, known as the Bragg angle. Thus, it is apparent that both AB and BC equals d sin Θ_B, which means the total path difference, (AB + BC), equals 2d sin Θ_B. Thus, Bragg's law can be formed: [41]

$$n\lambda = 2dsin\Theta_B \tag{14}$$

Where n is an integer number.

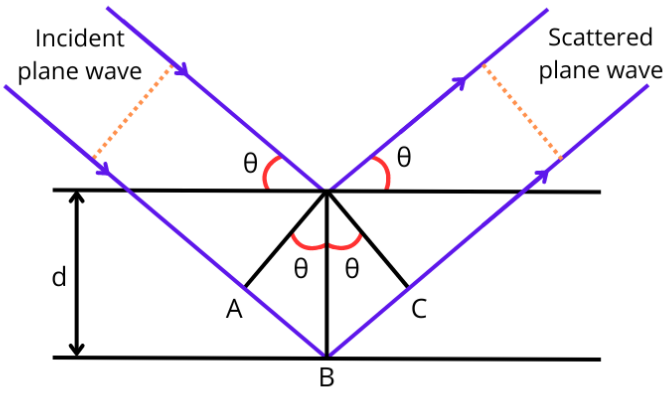

Figure 6: Bragg description of diffraction with respect to reflection of a plane wave with wavelength λ, at an incident angle Θ to atomic planes with spacing d. The resulting path difference between the reflected waves is AB+BC. Adapted from Williams and Carter [41].

This is a very simple and understandable way to describe diffraction. However, due to how the TEM operates, diffraction cannot be treated as reflection, as electrons do not exit the same surface as which it entered. Thus, another way to describe the diffraction of the transmitted electron the TEM utilizes must be found. A way to do so, is by applying the Laue conditions [41].

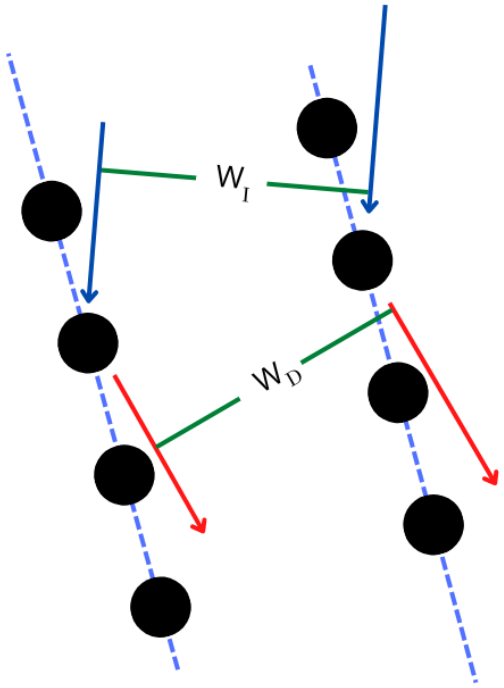

Figure 7: W_I, the incident wavefront and W_D, the diffracted wavefront illustrating scattering from two different planes. Adapted from Williams and Carter[41].

Figure 7 shows two atomic planes with an initial wavefront W_I and a diffracted wavefront W_D. For W_D to correspond to a diffracted beam, the atoms are required to scatter in phase. This is determined by the angles between incident and diffracted beam, in addition to the diffracting planes. The conditions for determining whether individual beams are in phase with each other are known as the Laue conditions.

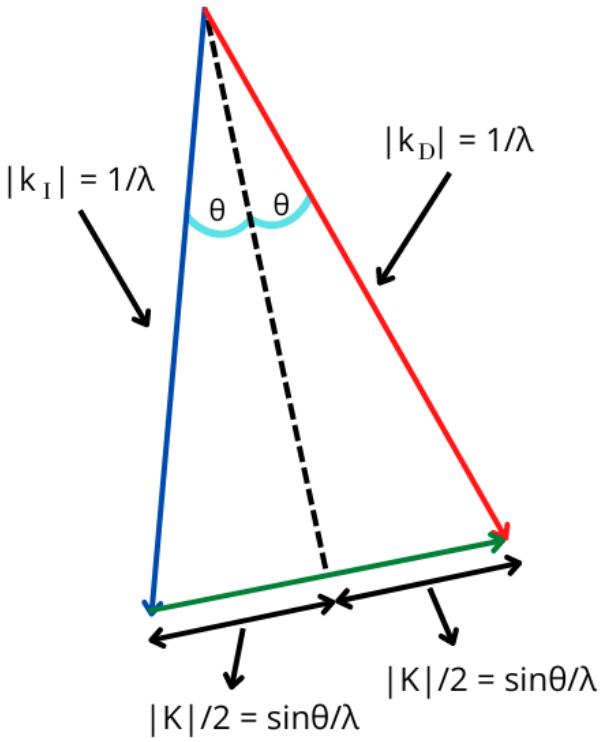

Figure 8: Illustration of the scattering vectors k_I (the incident wavefront normal) and k_D (the diffracted wavefront normal) and the difference vector K, with geometric relationships between k-vectors, the angle between them Θ and the wavelength λ. Adapted from Williams and Carter [41].

If an incident electron wave, defined by the k-vector k_I, is scattered elastically, with a resulting diffracted wave, defined by the k-vector k_D, then the relation between them is: [41]

$$|k_I| = |k_D| = |k| = \frac{1}{\lambda} \tag{15}$$

The change in direction between them due to scattering, defined by K, is

$$K = k_D - k_I \tag{16}$$

Looking at figure 8, simple trigonometry gives

$$|K| = \frac{2sin\Theta}{\lambda} \tag{17}$$

Applying Bragg's law (see equation 14), gives

$$|K_B| = \frac{1}{d} \tag{18}$$

At the Bragg angle Θ_B, K gets a special value K_B, which is defined so that

$$K_B = g_{hkl} \tag{19}$$

Where g_{hkl} is the reciprocal lattice vector where h, k and l are all integers and define the plane (hkl). This equation represents the Laue conditions and the occurrence of constructive interference is dependent upon whether or not it is fulfilled.

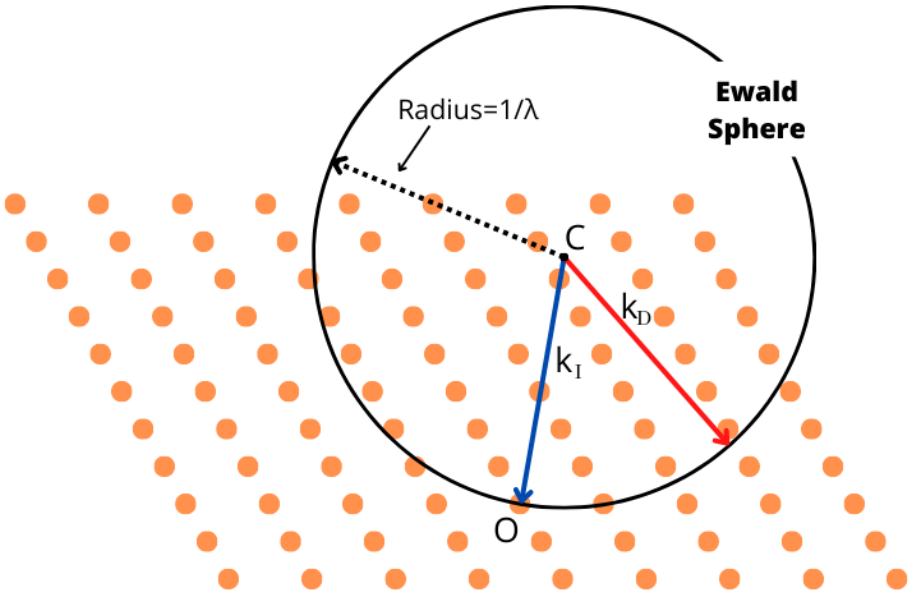

Figure 9: An Ewald sphere with radius $1/\lambda$ shown intersecting a non-cubic array of reciprocal-lattice points. O represents the origin of the reciprocal lattice, C is the center of the Ewald sphere, the CO represents k_I and k_D is any radius vector. Adapted from Williams and Carter [41].

The Ewald sphere of diffraction is a simple way of visualizing the three-dimensional array of points constructing the reciprocal lattice and why diffraction patterns occur. By constructing a sphere with a radius $1/\lambda$ which passes through the origin of reciprocal space, usually represented as a two-dimensional figure of a circle overlaying a two-dimensional cross-section of the reciprocal lattice, as seen in figure 9 above. Any reciprocal lattice points cutting through the surface of the sphere will have a corresponding set of planes that satisfy the Bragg condition. Due to the dimensions of the TEM sample and the fact that the real crystals considered in the TEM are not perfect, infinitely large crystals, some additional effects take place. Comparing the planes of the specimen with the unit cell dimensions, it is clear that the specimen is much thinner in the plane parallel to the beam, than the plane perpendicular to the beam(which can be considered infinitely

large). This leads to points present in the plane where the sample is thin being stretched into rods in reciprocal space. As opposed to the points, these reciprocal-lattice rods, relrod for short, will have a width. Thus, in reciprocal space there is a range of angles where the sphere can cut through a relrod and produce a diffraction spot, even though the Bragg condition is not truly met [41].

As of such, one can say that the Laue condition is relaxed in one dimension in the TEM, due to the effect caused by the shape of the specimen. Due to this shape effect, there will be some deviation from the Laue condition which must be taken into consideration. This can be defined by the deviation parameter, s, so that

$$K = g + s \tag{20}$$

The diffracted beam intensity will naturally be strongest when K=g, with less and less intensity the higher the deviation. As illustrated in figure 10, in reciprocal space, s is the vector distance away from the Bragg condition. This point G must not be mixed up with the reciprocal space lattice vector, g. It is simply any reciprocal lattice point which can be located both on the inside and outside of the Ewald sphere at any distance away it. Though, the further away G lies, the larger the deviation s and the lower the intensity. The sign of s is defined in such a way that it is positive when G is located on the inside of the Ewald sphere and negative when G is located on the outside. It is then intuitive that when s=0 the sphere passes through the exact centre of the relrod at the reciprocal lattice point [41].

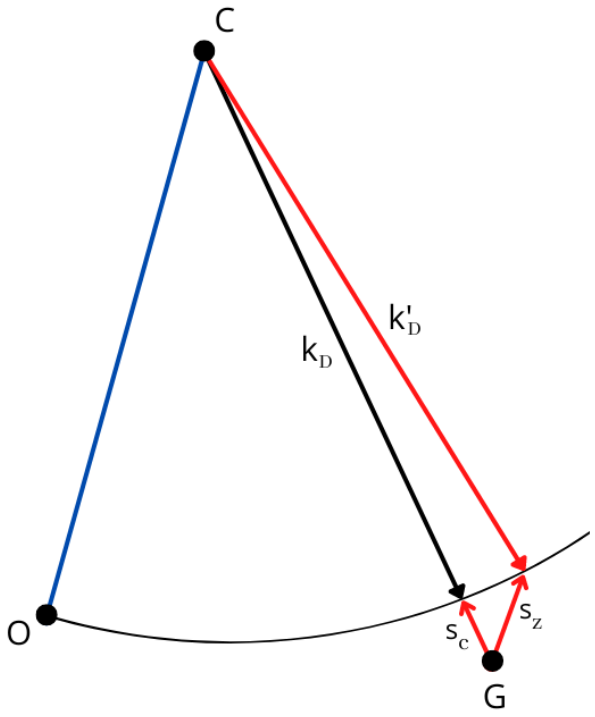

Figure 10: Illustration of the deviation parameter s with the two special values s_C and s_Z. The value s_C arises when k_D lies along CG and and thus s is parallel to CD. The value s_Z arises when we choose s to be parallel to the incident beam direction CO, for which k_D becomes k'_D. Adapted from Williams and Carter [41].

2.5.3 Spectroscopy

As the energetic electron beam strikes the specimen surface, the atoms in the specimen are stimulated to emit X-ray photons. There are two types of X-ray radiation which is produced, the bremsstrahlung, which produces a continuous X-ray spectrum, and more interestingly the characteristic X-ray photons. These specific energies are, as the name suggests, characteristic for each atom species. The bremsstrahlung will not be further elucidated, but it produces a "background" radiation which affects the accuracy in the measurements of characteristic peaks.

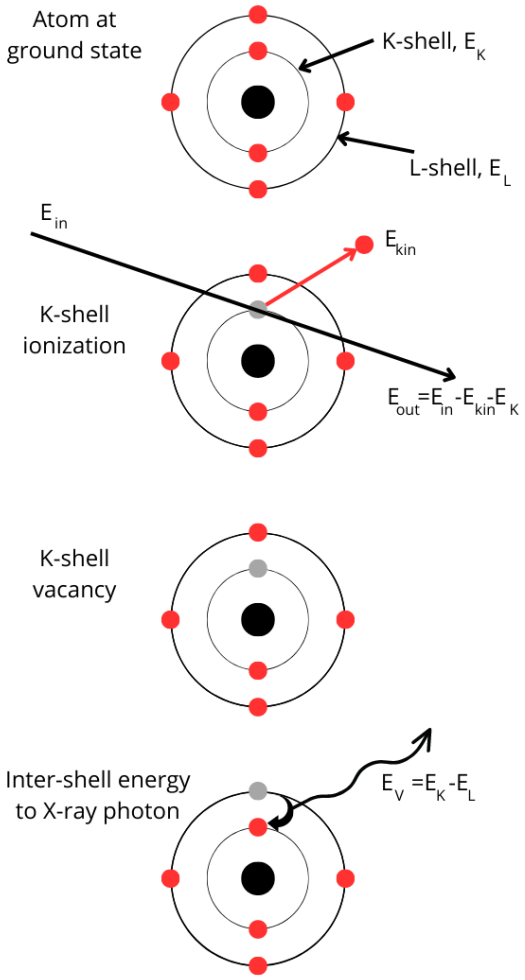

Figure 11: Schematic sketch of the process of X-ray generation with the carbon atom used as an example. An atom in an inner shell is ionized by inelastic scattering of an energetic beam electron. This leaves the atom at an elevated energy state which can be lowered by an L-K inter-shell transition and subsequent creation of an X-ray photon to carry of the inter-shell transition energy, E_K-E_L, which expresses the characteristic energy of the X-ray photon. Adapted from Williams and Carter [41].

2.5.4 TEM hardware

In general the TEM can be conveniently divided into three main components, The illumination system, the objective lens/stage and the imaging system. These three components put together are often referred to as the column. The illumination system is comprised of the gun and condenser lenses. Simply put, the parts of the instrument with the role of transferring and focusing electrons from the source to the specimen. This systems two main modes of operation (illustrated in figure 12 below) are parallel beam, mainly used for TEM imaging and selected area diffraction (SAD), and convergent beam, mainly used for X-ray and electron spectroscopy, scanning (STEM) imaging and convergent beam electron diffraction.

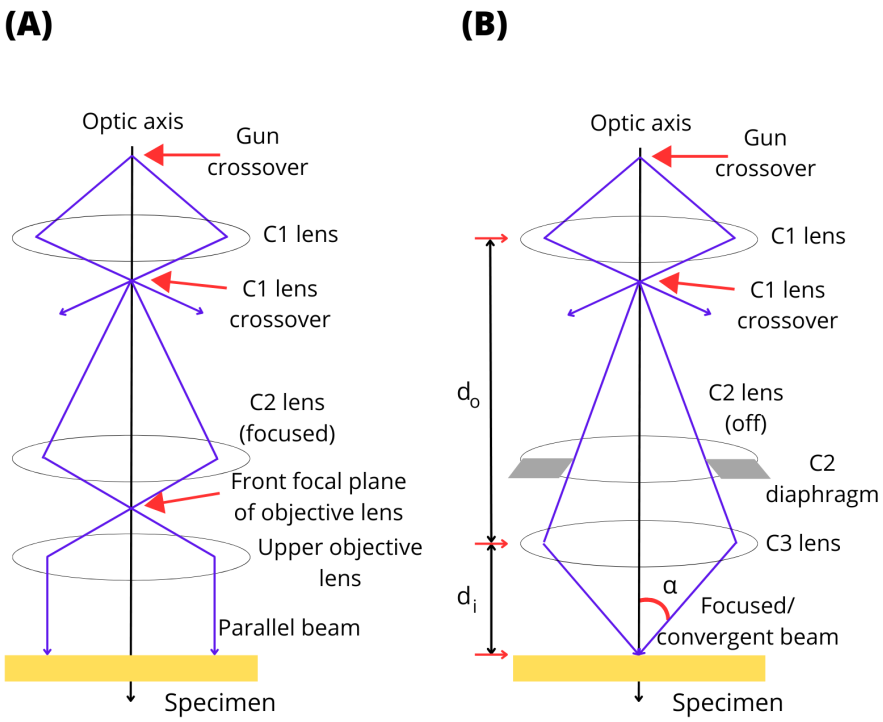

Figure 12: The two main modes of the illumination system. (A) The basic principle of parallel-beam mode in the TEM. Using the C1 and C2 lenses to image the source at the front focal plane of the objective lens, thus creating a parallel beam at the specimen plane. (B) The basic principle of the convergent-beam/probe mode in the TEM. The largest possible d_o/d_i ratio yields the maximum demagnification of the image of the gun crossover. The largest possible convergence angle α yields the smallest possible probe. As such, effectively turning the C2 lens off and using the upper-objective polepiece as C3 lens yields the best convergent beam. Adapted from Williams and Carter [41].

The parts comprising the objective lens and stage/specimen holder system is given in the name. This is the part of the instrument where all the interactions between beam and specimen occur. The two fundamental operations of this component is creating images and diffraction patterns. The objective lens is considered as the most important lens in the TEM, as the quality of which will determine the quality of all the information the system is able to gather from the sample.

The final main component, the imaging system is comprised of several lenses, a viewing screen and/or a computer display via a detector, TV-camera or CCD. The lenses are simply magnifying lenses, often referred to as the intermediate and diffraction lenses. In addition to the final lens, often referred to as the projector lens as it is this lens that projects the image or diffraction pattern onto the detector or viewing screen [41]. A schematic of a TEM column is shown below.

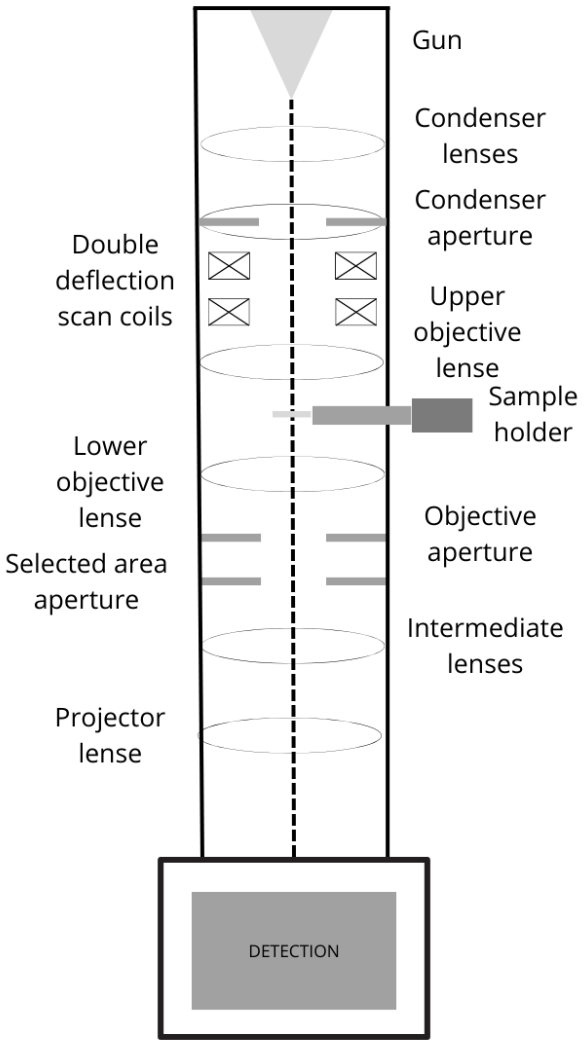

Figure 13: Schematic sketch of a TEM column showing the three main components and their distribution. Adapted from Williams and Carter [41].

2.5.5 STEM hardware

In STEM mode, a convergent beam kept parallel to the optical axis by the double deflection coils is scanned across the specimen. There are two different STEM detectors, both situated in a conjugate plane to the back focal plane and differed by the angle at which the electrons are scattered. The bright field detector collects electrons scattered at angles $\Theta < 10$mrad, and the annular dark field detector collects electrons scattered at higher angles. STEM mode is the preferable way of performing EDS analysis in the TEM, through acquisition of spectra of characteristic x-rays from each position it is scanned over [41].

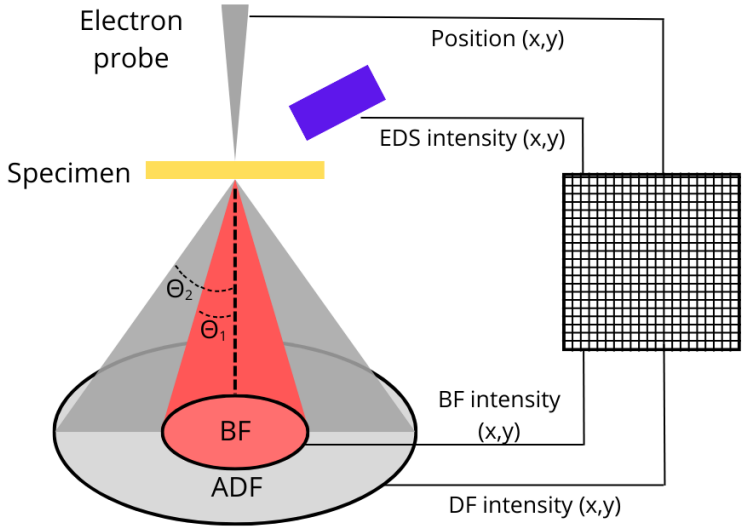

Figure 14: Schematic drawing of signal generation and detection in STEM mode. For each position the condensed electron probe is scanned across, the scattered electrons can be detected either by the BF detector ($\Theta < 10$ mrad) or the ADF detector ($\Theta > 10$ mrad). An EDS detector can also be used to acquire EDS spectra from each position the probe is scanned across. Adapted from Williams and Carter [41]

2.6 Focused Ion Beam(FIB)

2.6.1 Interaction of ions with matter

As a beam of high-energy particles strike a solid surface, several interactions may occur. Some particles will be reflected or backscattered, and some will slow down within the solid. Compared to an electron an ion is significantly larger, heavier and more massive, in addition to possibly carrying a positive charge. This means that an ion will have much greater difficulty of penetrating the surface of the solid as they struggle to pass through the voids between individual atoms. This means that the probability of interacting with the atoms increases significantly, leading to a rapid loss of energy. Because of this, the main ion-atom interaction is atomic ionization and breaking of bonds between surface atoms. These interactions are usually accompanied by an emission of secondary electrons (SEs), accompanied by a change in the chemical state of the material. Due to this more direct effect on the target sample, it can affect it in several ways; localized heating, removal of atoms beneath focus, implanting ions into the surface and depositing atoms above focus [43].

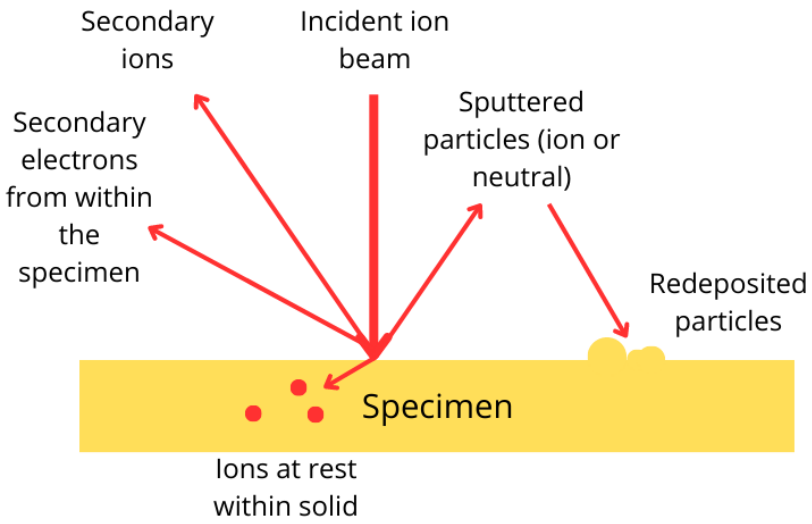

Figure 15: The different kinds of interactions occurring when the high energy ion beam hits a specimen. Adapted from Giannuzzi [44].

2.6.2 Gas assisted focused ion beam etching

Due to their ability to precisely mill away material from localized areas, FIB systems are widely used as a micro-machining tool. In order to assist these milling processes, a fine capillary tube is used to introduce a reactive, neutral gas to the milling site. Through the introduction of this gas the etching rate compared to just sputtering of the material is enhanced. In addition, it reduces the amount of redeposited material resulting from sputtering from the sample. The aim of the gas is for it to react with the sample and create a volatile compound, which in turn can be removed by the vacuum system. This process of gas assisted FIB etching can be divided into three steps as follows: [43]

1) Introduction of a reactive, chemically neutral gas through a gas nozzle which is adsorbed or chemisorbed on the sample surface.

2) The gas will either react with the sample spontaneously, or decompose in the presence of the ion beam and react with the sample.

3) Desorption, the volatile products leave the surface.

The most important milling process for this work is the cross-section. Two different types of it is available, both with advantages and disadvantages. The regular cross-section will mill away

horizontal layers laterally down into the sample. This is the most time-effective cross-section, however, by milling in this fashion the sample surface will be exposed to sputtering which affects the composition of the sample surface. The cleaning cross section however mills away lateral slices horizontally towards the resulting surface, leaving a sample surface not affected by sputtering, however it is a much slower process. Both cross-sections are illustrated in the figure below.

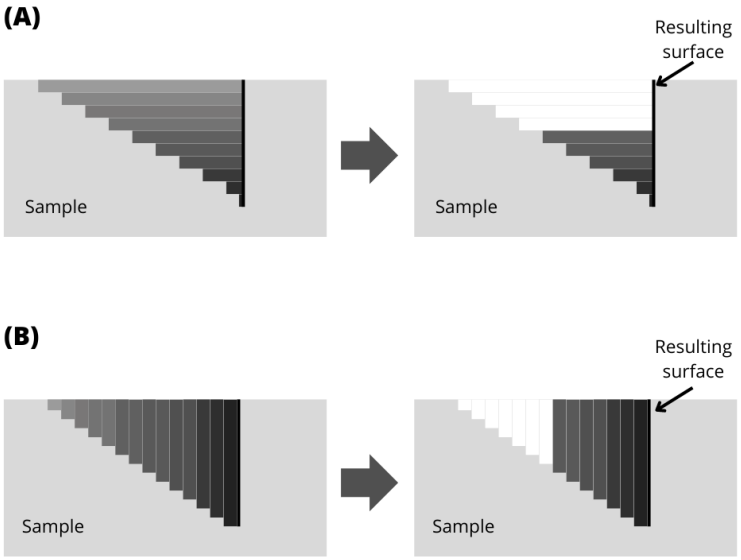

Figure 16: Illustration of how the different cross-section types remove material. (A) Regular cross-section. (B) Cleaning cross-section

2.6.3 Gas assisted focused ion beam deposition

In general, FIB induced deposition is a very local process, depositing only where the ion beam is scanning. Gas assisted FIB deposition is a direct form of deposition, utilizing only the ion beam along with a gas. This deposition process can be described by three steps as follows: [43]

1) Introduction of gaseous compound precursor through fine gas nozzles inserted close to the sample surface which then adsorbs on the surface.

2) Decomposition of the gas molecules adsorbed on the surface into volatile and non-volatile products by the incident energetic ion beam where the ion beam is scanning. This energetic beam will simultaneously cause sputtering of the sample surface.

3) Volatile products such as oxygen and hydrogen leave the surface, while non-volatile products remain on the surface, producing deposition layers.

As the gas molecules adsorbs on the surface, the precursor compound needs to have a high enough sticking probability to remain on the surface for a sufficient time before it decomposes. In addition, the remaining precursor compound on the surface must be easily decomposed by the incident ion beam in order for any deposition to occur. While the incident ion beam decomposes the precursor

on the surface, it also sputters or mills material on the surface of the sample. So one can define the total deposition yield, Y_{dep}, in other words the number of atoms deposited per incident ion, as a function of the decomposition yield of the precursor gas, Y_{decomp}, and the sputtering yield on the surface, Y_{sputt}:

$$Y_{dep} = Y_{decomp} - Y_{sputt} \tag{21}$$

In general, the FIB is dependent on many beam parameters to be adjusted correctly for successful deposition to occur. The total deposition rate will depend on a combination of local pressure or local gas flux, ion beam current, dwell time per pixel, pattern size, beam overlap and raster refresh time.

2.6.4 FIB hardware

Using only a FIB system has its disadvantages, mainly due to the damage it causes to your sample. Due to the growing complexity of materials and its accompanying challenges, the two-beam system has been developed. Through the combination of an ion beam and an electron beam in the same system, it has the same wide range of applications as an ordinary FIB, with the added benefits of high resolution and non-destructive imaging of the scanning electron microscope (SEM) [43].

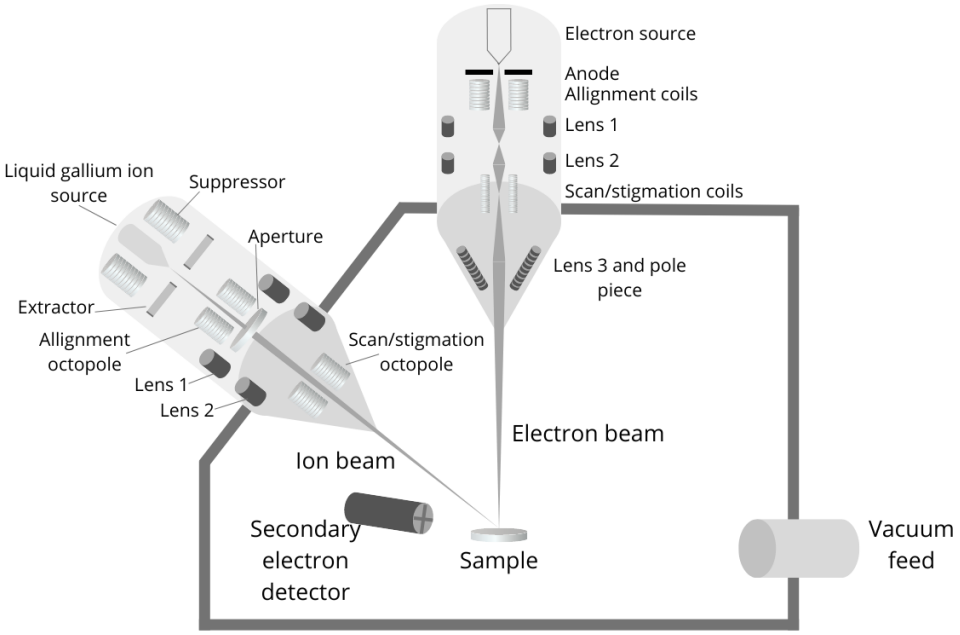

Figure 17: Schematic illustration of a Focused ion beam two-beam system. Adapted from Yao [43].

Both the FIB and the SEM system work in a similar fashion. Both sources emit charged particles which are focused into a beam and rastered over small areas of the sample through the usage of detection plates or scan coils. However, while the SEM uses magnetic lenses to focus the electron beam, the FIB uses electrostatic lenses. This is due to the much higher mass of the ions, with a corresponding low Lorenz force, causing them to be much slower [43].

The most usual type of ion used in a FIB are Gallium ions (Ga^+). This is due to a number of reasons. With a low melting point, it requires a low amount of heating and the low temperature minimizes interdiffusivity with the tungsten needle. It has a mass high enough to mill heavier elements, but not as heavy that it will immediately ruin the sample. The low volatility at its melting point ensures long lifetimes. It has a low vapor pressure, thus pure gallium is applicable instead of having to use an alloy. Finally, it is easily distinguished from other elements, thus when doing analysis of a sample, any implantation of Ga should not interfere with the results [43].

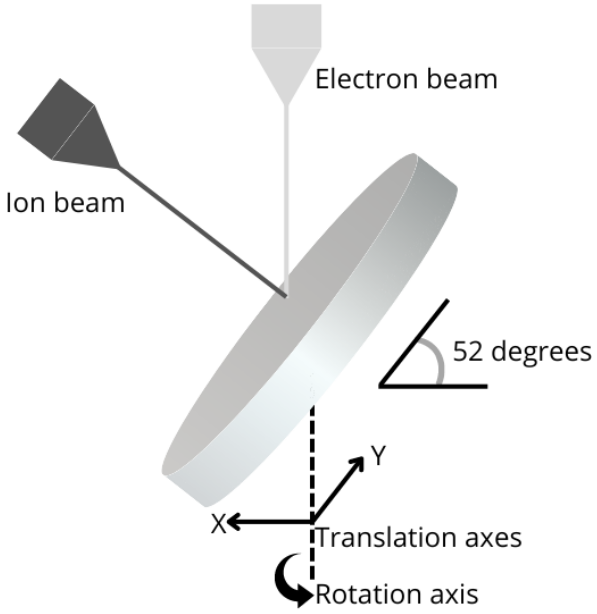

Figure 18: Schematic illustration of the primary orientation of the sample when operating the two-beam system. Adapted from Yao [43].

Both the FIB and the SEM uses SEs as the main method to form high resolution images. However, BSEs and secondary ions (for FIB) can be detected to form images. Both the ion source and the electron source have fixed positions in the system with an angle between them at 52^o. These two beams are then co-focused at a point referred to as the coincidence point. The stage on which the sample is situated can be moved and tilted in all directions, but is for most applications of the FIB tilted to an angle of 52^o so that the ion beam hits perpendicularly at the sample surface. The symbiotic effect of the combined system yields better and more extensive data collection, but it also opens to the possibility of using the SEM to precisely monitor the progress of operations with the FIB. For example with TEM sample preparation the non-destructive imaging of the SEM is crucial. As the FIB alone causes major damage to the thin sample when imaging [43].

2.7 Scanning Electron Microscope

2.7.1 Interaction of electrons with matter

The accelerating voltage in a SEM is typically 0.1-30 keV. Since the bulk specimens usually used in the SEM are relatively thick, only signals re-emerging from the incident specimen surface are

utilized. The two signals most commonly used for image formation are BSEs and SEs. BSEs are referred to as quasi-elastic signals, originating from the incident electron beam which is subjected to multiple scattering events, changing its trajectory and finally re-emerging from the surface. The yield of BSEs are most affected by the atomic number Z. The yield of the other signal, SEs, is usually several times higher. Since SEs are loosely bound outer shell electrons from the specimen atoms, they will only need a sufficient kinetic energy to be ejected from the atom. The SEs that are created will propagate through the sample in various directions and angles and thus some will escape through the surface. The depth from which these SEs can escape from is only in the order of nanometres. The SEs escaping from the surface of the specimen can be divided into two categories: SE_1, the ones created from a beam electron entering the surface, and SE_2, the ones created from BSEs escaping the specimen [45].

2.7.2 SEM hardware

In the SEM, the electron beam is scanned across the specimen. For each point (x,y) on the sample surface, at least three variables are collected, for example intensity of SE or BSE in addition to the position (x,y). This is then used to construct a image of pixels described by the intensities at each respective position creating the image contrast. The system itself is very comparable to the TEM column. The components present in the SEM is quite similar to what can be found above the sample stage in a TEM column. But the better way of illustrating the composition of a SEM system would be considering figure 17 excluding the ion beam system.

2.8 Experimental techniques

2.8.1 FIB Lift-out specimen preparation

The technology of TEM sample preparation in the FIB has evolved to a rather advanced stage, seeing automated techniques allowing for a yield in the area of hundreds of samples produced each day. On the other hand, this work will focus on the manual, site specific TEM specimen preparation method. This includes a FIB micro-sampling technique and an in-situ lift-out specimen preparation technique. The reason why it is referred to as in-situ is that the electron transparent membrane that will eventually become the TEM sample is removed from the bulk while still inside the FIB. This is opposed to ex-situ techniques where the TEM sample is removed from the bulk after the bulk is taken out of the FIB. Though these ex-situ techniques can be slightly more time-efficient than in-situ, the big advantage for the latter is the possibility of producing larger TEM samples. The in-situ lift-out technique is heavily based around the use of a micromanipulator probe. It is a motor-driven tungsten probe that can be driven in three dimensions(x, y and z). This enables it to be finely controlled and precisely positioned to be bonded to and extract the specimen from the bulk sample, which can then be transported over and bonded to a micro-sample carrier [44]. These techniques will be further elucidated in the method section.

2.8.2 Imaging and diffraction in the TEM

The TEMs two most important modes of operation is imaging and diffraction. Though the end results look widely different, the two are closely related. They are both formed using a parallel

beam, but differed by the mode of the image system. The electrons having passed through the sample are dispersed to form a diffraction pattern in the back focal plane of the objective lens and recombined to form an image at its image plane. As such, in order to see the DP, the imaging system lenses are adjusted so the BFP of the objective lens acts as the object plane for the intermediate lens. This will project the DP onto the viewing screen/CCD. This is termed diffraction mode. On the other hand, when in imaging mode, the image is projected onto the screen/CCD. This is done by adjusting the intermediate lens so that its object plane is the image plane of the objective lens. On modern TEMs this switch is done by simply pushing buttons on the console or clicking icons on the computer screen.

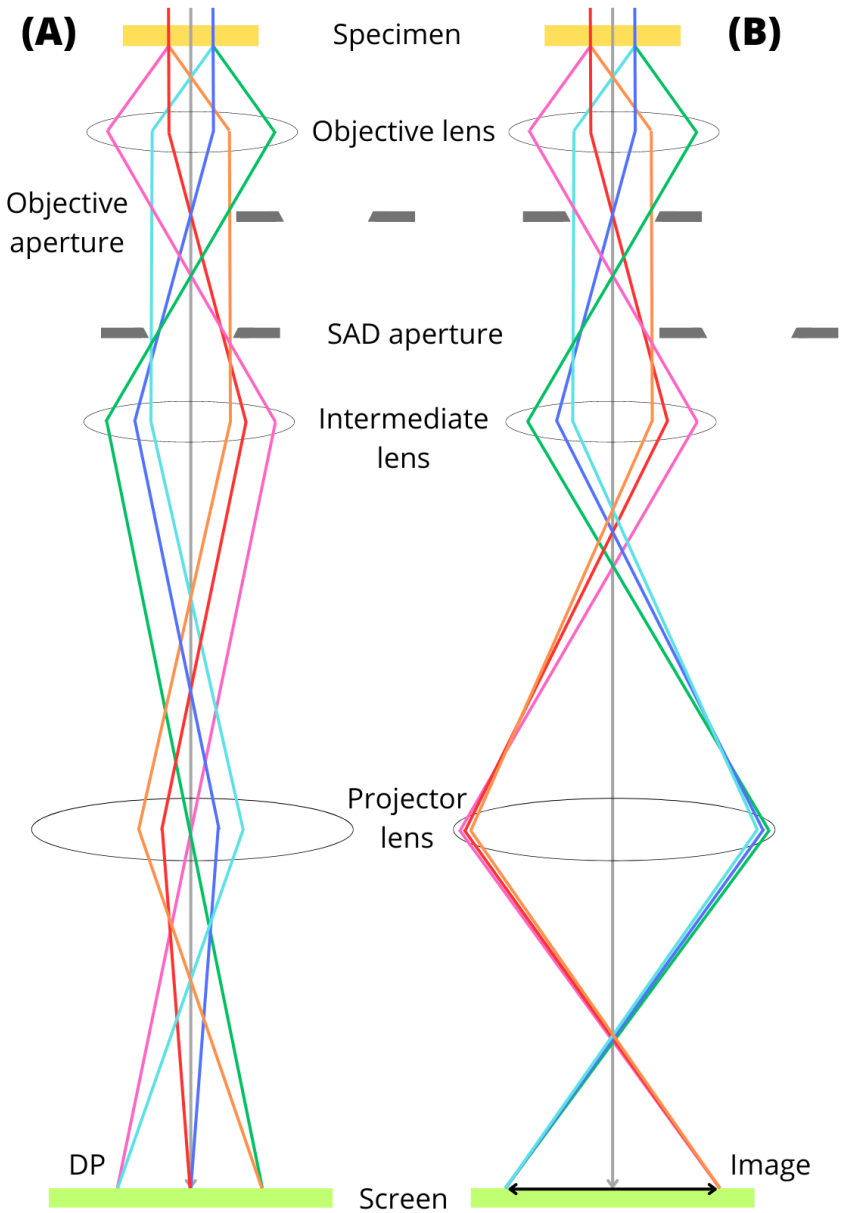

Figure 19: Schematic illustration of the two modes of the imaging system. (A) In diffraction mode, the intermediate lens selects the BFP as its object and projects the DP onto the viewing screen. (B) In image mode, the intermediate lens selects the image plane as its object and projects the image onto the image lens. Adapted from Williams and Carter [41].

In general, the DP formed from the entire illuminated area as in figure 19 is not usable. Firstly, because it forms a not very understandable mash of information, secondly, because the intensity of the direct electron beam will damage the viewing screen and/or saturate the CCD camera. Thus, some simple actions may be executed to select specific areas of the specimen and reduce the intensity of the direct beam. With figure 19 above as reference, two things may be done to achieve this: making the beam smaller, and/or inserting an aperture above the specimen to reduce the amount of electrons striking the specimen and the area of the specimen struck by electrons. The

first option however would involve converging the beam at the specimen, effectively ruining the parallelism. As such, the standard way of performing SAD is by inserting a selected-area aperture. However, try as you might, inserting an aperture in the specimen plane is not an option, as the space is occupied by the specimen. This problem may however be circumvented by inserting an aperture in a plane conjugate with the specimen, creating a virtual aperture at the specimen plane. The conjugate plane used is the image plane of the objective lens. The DP formed by doing SAD is known as a selected area DP (SADP).

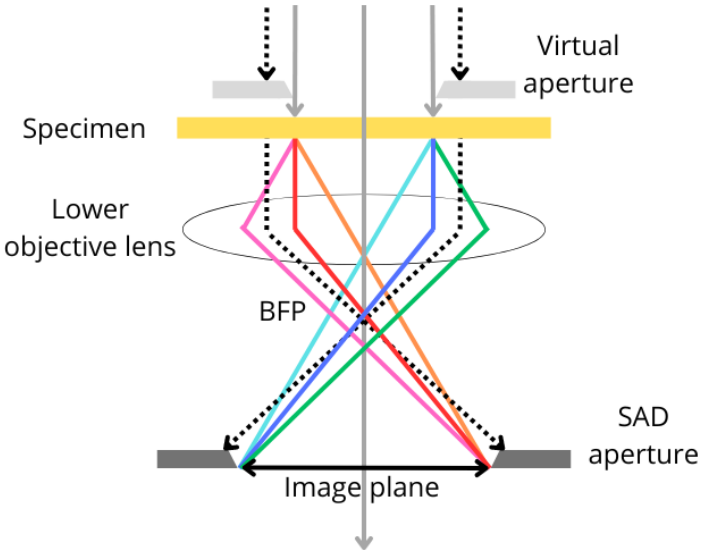

Figure 20: Schematic illustration of the effect of the selected area aperture. The ray diagram shows how SADP is formed. By inserting the selected area aperture in the image plane conjugate to the specimen plane, a virtual aperture(here depicted slightly above the specimen plane) is created in the specimen plane. Thus, only electrons falling inside the dimensions of the virtual aperture is able to travel through the imaging system. All other electrons will hit the SAD aperture(visualized by the dotted lines). Adapted from Williams and Carter [41].

The SADP formed is the basis of the two basic imaging techniques in the TEM, bright-field (BF) and dark-field (DF) imaging. BF images are formed by inserting and centering an objective aperture on the central spot in the SADP. Then, after removing the SA aperture only electrons contained in the direct beam will contribute to image formation. On the other hand, centering an objective aperture on any other spot in the SADP will result in the formation of a DF image.

2.8.3 Qualitative EDS analysis

For the optimal results in a TEM, EDS analysis should be performed in STEM mode, yielding the best resolution and area control. For the successful acquisition of an EDS map, the total counts in the qualitative spectrum should exceed 1,000,000 over the full energy range. To achieve such a number, the probe can scan across the selected area several times.

3 Experimental method

3.1 Materials and samples

The 1xxx-series welded samples examined were ready-made SEM samples produced during a previous master's thesis studying the efficiency of different inoculating particles in screw extruded aluminium composite filler wire [17]. A base alloy AA1370 with particle additions of 1.5 wt% Ti and 2 wt% TiC resulted in the filler wire. This was used to arc-weld sheets of AA1050-H14. The figure below shows macrographs of the samples and their respective mean grain sizes and porosity. Compared to the reference WM, with GMAW and GTAW producing mean grain sizes of 141 ± 79 µm and 163 ± 67 µm and porosities of 1% and 0.2% respectively [17]. It is clear to see its efficiency as a grain refiner, however porosity poses an issue.

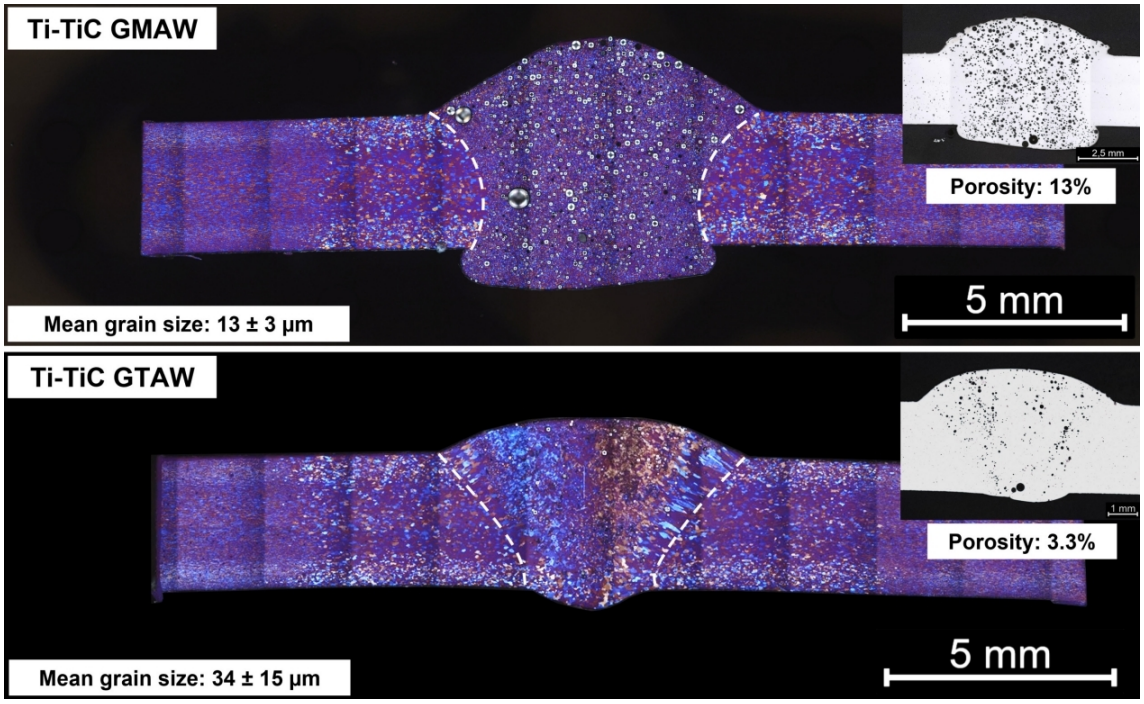

Figure 21: Figure showing macrographs of the MIG and TIG welded samples and their respective mean grain sizes and porosity. Reprinted from Kirkbakk [17].

3.2 Sample preparation

The 1xxx-series SEM samples previously sat in epoxy were cut to produce thin slices of the weld metal which subsequently were mounted on stubs using superglue. These were then polished according to table 1, this to remove the oxide layer which had built up since it was last used. Carbon-tape was then wrapped around the outline of the weld-piece to achieve good conductivity through the stub.

Table 1: The set-up for the polishing steps.

Set-up	Step 1	Step 2
Cloth	MD-Mol	MD-Nap
Suspension	DiaPro Mol3	DiaPro Nap R1
Rpm	200	150
Number of manual rotations	150	50

3.3 Scanning electron microscopy

The SEM used in this study is a Zeiss ULTRA 55 FEG SEM. The SEM was used as a tool for pinpointing the most promising areas for producing TEM lamellas in the FIB. This because the SEM in the dual-beam FIB yields lower quality images. Initially this was not used as a preparatory measure, thus increasing the time spent at the FIB identifying these promising areas. As the resolution and quality of image in the SEM was much better, this time spent was lowered drastically, yielding a more efficient overall process. An example of such a promising area is shown below:

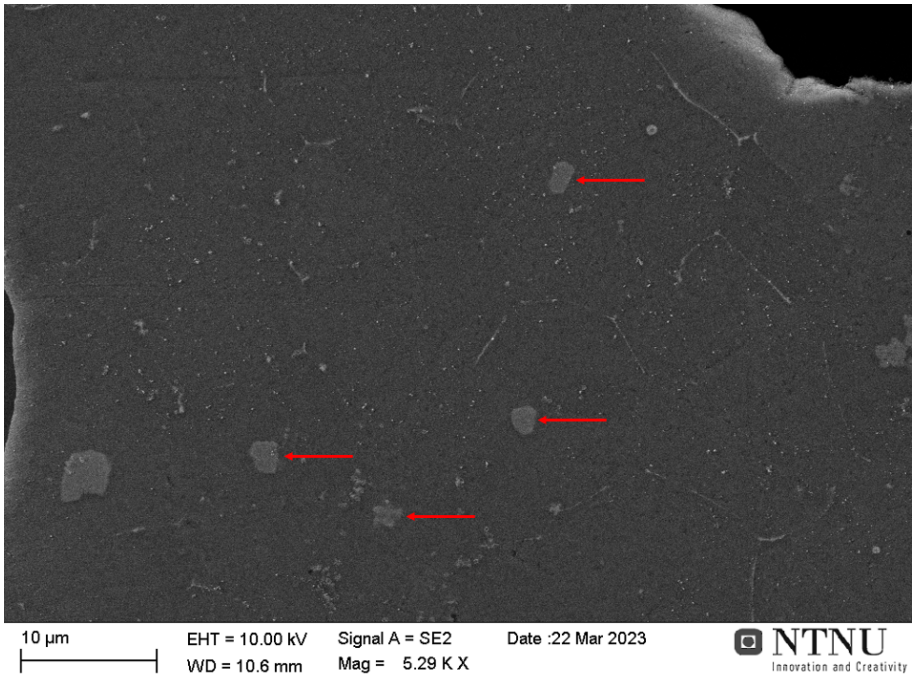

Figure 22: SEM image showing a promising region containing four smaller $TiAl_3$ particles(red arrows) laying approximately at the centers of their respective grains.

3.4 Focused ion beam

This part of the method section is in large parts based on an unpublished project assignment used as a preparatory work for establishing methods. These were established due to the need of an alternative production route to electropolishing for TEM samples. This is due to the method's difficulties of producing viable samples from porous metals, in addition to little to no area control. The following part may as such be considered the most important result for anyone in need of a

method for selected area production of TEM samples from porous metals.

The FIB used in this study is a FEI Helios NanoLab DualBeam FIB as a tool for producing site-specific TEM samples. After several attempts at making viable samples from whole $TiAl_3$ particles laying visible at the surface, it was found that very small parts of the $TiAl_3$ would be to be found as part of the resulting TEM sample. Thus an alternative technique was established in order to obtain samples containing the centers of these particles. By finding several grains containing just a small $TiAl_3$ spot in the middle and hoping that some of them would be just the "tip of the iceberg", allowing almost an entire $TiAl_3$ particle to be extracted as part of the TEM lamella. The in-situ lift-out specimen preparation technique was used according to the following steps:

After locating a promising area, a protective Pt-layer is deposited on top of the $TiAl_3$ particle.

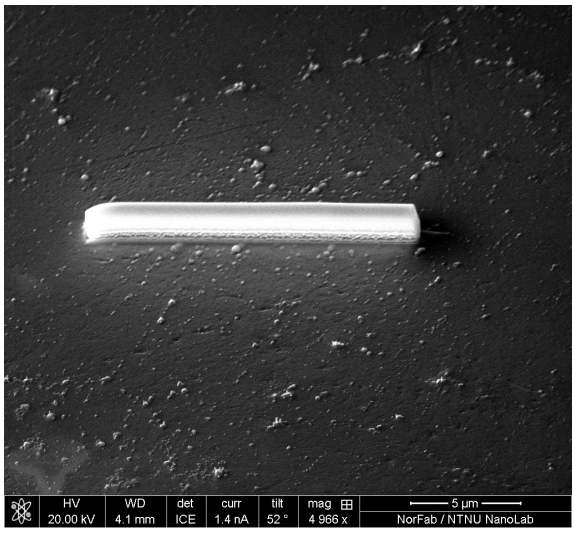

Figure 23: SEM image taken in the FIB showing Pt-layer deposited in the center of a grain.

To check whether the $TiAl_3$ particle continues below and the sample is worth investigating a regular cross-section is cut out on one side of the Pt-layer, unveiling the area below.

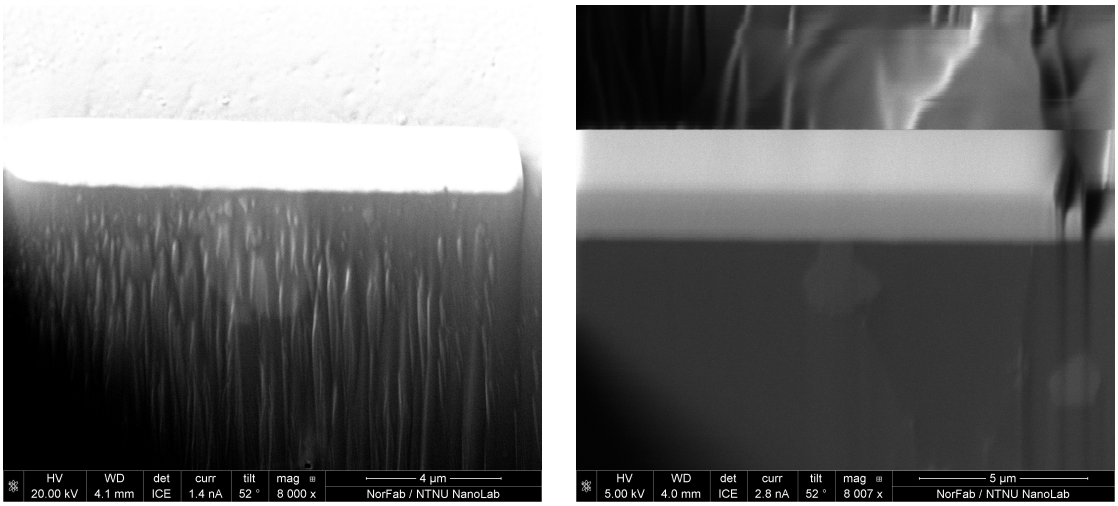

Figure 24: SEM images taken in the FIB. Showing on the left, a sample worth pursuing with a large contrasting $TiAl_3$ particle visible. On the right, a sample not worth working on with a small part of the $TiAl_3$ visible.

Once a sample worth working with is uncovered, regular cross sections are milled out on each side of the sample. A rectangle is also milled out at one end of the sample in order to ease the placement of the lift-out finger. Upon completion, cleaning cross-sections are milled out on each side leaving a clean sample surface with a sample thickness of approximately 1 micron. The surface uncovered after the cleaning cross-section is performed will also give a final confirmation regarding the quality of sample.

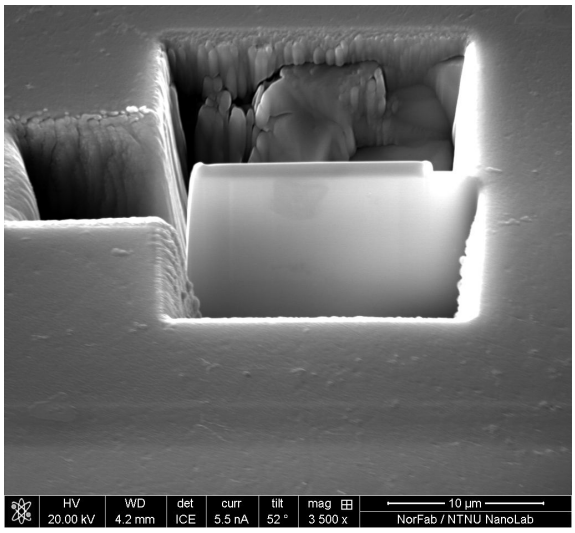

Figure 25: SEM image taken in the FIB. Showing the sample after a full bulkout.

To ease the removal and transferal of the sample a U-cut is performed. By milling away the bottom and parts of the other side of the sample, it will then hang on only a small section.

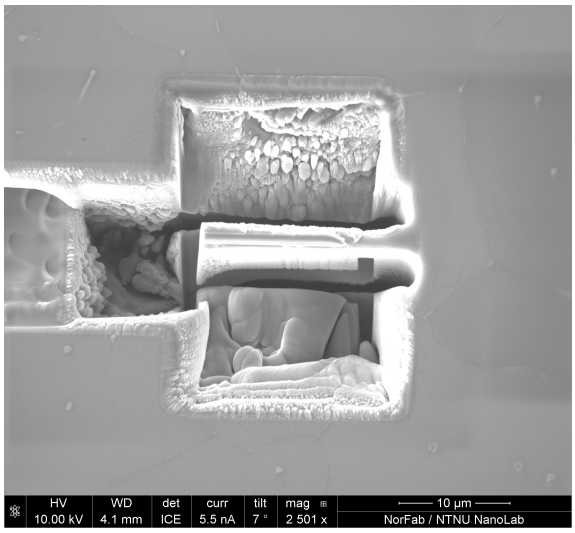

Figure 26: SEM image taken in the FIB showing u-cut of the sample.

Then it is time to introduce the Omniprobe lift-out finger. It is placed next to the upper edge of the sample and fastened to it by depositing Pt. Then the small section that is still connecting the sample and the bulk is cut away. Now the sample is fastened only to the finger and can be lifted out and transported to the other holder with the TEM lift-out grid.

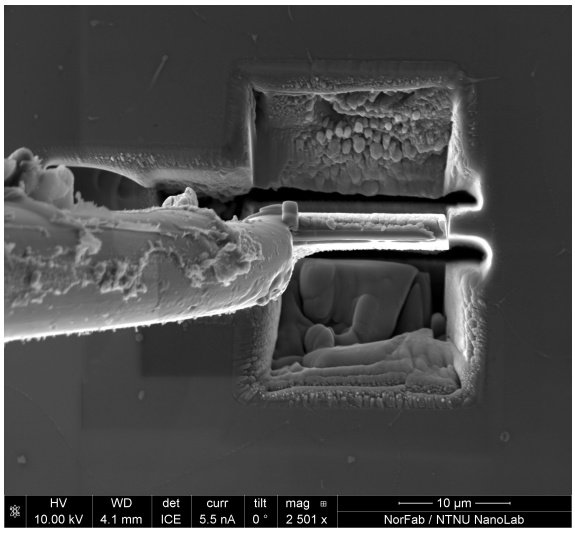

Figure 27: SEM image taken in the FIB showing the Omniprobe lift-out finger lifting the sample out after fastening.

The sample is placed next to one of the teeth of the lift-out grid and fastened to it by depositing Pt as a weld. After it is properly fastened to the lift-out grid, the Pt-layer connecting the finger to the sample can be cut away, and the finger can be driven back to default position.

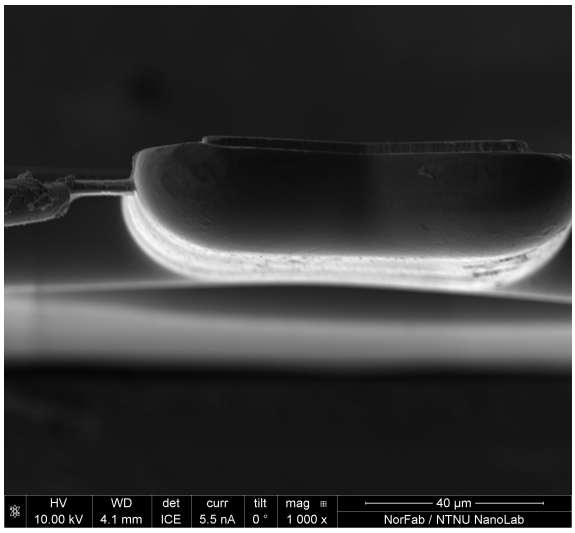

Figure 28: SEM image taken in the FIB showing the sample positioned with the Omniprobe lift-out finger and fastened.

It is now time to thin the sample enough to make it electron transparent, requiring a thickness of approximately 100 nm. This is done by performing a series of thin cleaning cross sections on each side of the sample.

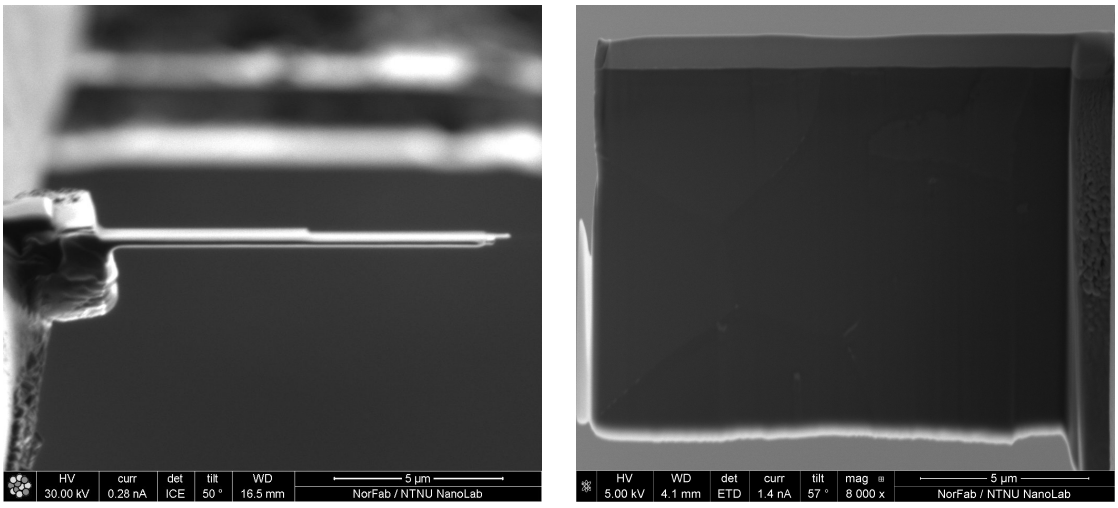

Figure 29: SEM images taken in the FIB. Showing on the left, a thinned out sample from above. On the right, a thinned out sample from the side.

When the required thickness is reached, the sample was carefully removed first from the FIB, and then from the sample holder. It was then placed directly into a membrane box in between two pieces of cigarette paper, example shown below, as further protection for the sample.

Figure 30: Image of the sample box used for transferring the sample from the FIB to the TEM. It is a membrane box with the sample having been placed between two pieces of cigarette paper.

Table 2: The set-ups for the different ion beam operations used during FIB TEM lamella preparation. Some deviations in the sizes given below was applied depending on size and shape of the lamella.

Operation	**Application**	**Tilt**	**Shape**	**Size (X,Y,Z)** [μm]
Protective Pt-layer	Pt-dep	52^o	Rectangle	15x1.5x1.5
Bulk-out coarse	Si	52^o	Regular cross-section	20x12x6
Omniprope cut-out	Si	52^o	Rectangle	10x10x6
Bulk-out fine	Si	52^o	Cleaning cross-section	20x1.5x6
U-cut	Si	7^o	Rectangle	1.5 wide, overlapping
Weld Omniprobe-sample	Pt-dep	0^o	Rectangle	1x3x0.5
Cut loose sample	Si	0^o	Rectangle	1.5x3x2
Weld sample-grid	Pt-dep	0^o	Rectangle	1.5x4x1
Cut Omniprobe-sample	Si	0^o	Rectangle	1x3x1
Thinning coarse	Si	52 ± 2^o	Cleaning cross-section	12x1x3
Thinning fine	Si	52 ± 2^o	Cleaning cross-section	12x0.4x3
Thinning end	Si	52 ± 2^o	Cleaning cross-section	6x0.2x3
Cleaning	Si	52 ± 4^o	Rectangle	6x2x0.05

Table 3: Applied currents and voltages for the different ion beam operations used during FIB TEM lamella preparation.

Operation	Current	Voltage
Protective Pt-layer	93pA	30kV
Bulk-out coarse	21nA	30kV
Omniprobe cut-out	21nA	30kV
Bulk-out fine	6.5nA	30kV
U-cut	2.8nA	30kV
Weld Omniprobe-sample	48pA	30kV
Cut loose sample	2.8nA	30kV
Weld sample-grid	93pA	30kV
Cut Omniprobe-sample	2.8nA	30kV
Thinning coarse	0.92nA	30kV
Thinning fine	93pA	30kV
Thinning end	93pA	30kV
Cleaning	46pA	5kV

3.5 Transmission electron microscopy

The samples produced were examined in a JEOL JEM LaB6 2100 FEG TEM and a JEOL JEM 2100F FEG TEM for a few applications. In order to orientate the samples inside the TEM a JEOL dual tilt Beryllium holder was used. All operations done in both TEMs were performed at an accelerating voltage of 200 kV. Bright field images were acquired to find the location, size and shape of interesting features.

3.6 EDS analysis

Both the 2100 and 2100F is equipped with an Oxford X-Max 80 SDD EDX which was used for all EDS analysis performed in this work. All EDS map data were acquired in STEM mode, with a spectral range 0-20 keV, process time setting of 6 and with an analytical probe of 2 nm. The camera length was set to 20 cm and a condenser aperture of 50 μm was used. The detector was controlled through the AZtecEnergy software. All samples were tilted in the x-direction in a manner as to maximize the signal acquired. Scan time depended on the quality of the signal ranging from 0.5-2 hours.

3.7 Data processing

All acquisition of TEM images were performed using Digital Micrograph, with ImageJ used to set scale bar. The EDS data acquired by the AZtecEnergy software was exported as a file format readable for Python(.msa used for a single spectrum for energy calibration, .raw and .rpl used for the map data, and a .txt file used for spatial calibration information). In order to analyze the EDS data, the Python library HyperSpy was utilized. In order to save the data as the standard HyperSpy file format hdf5, the script presented in Appendix B.1 was applied. The scripts created by Tor Inge Thorsen shown in Appendix B.2 and Appendix B.3 were used to produce qualitative

EDS maps and ”line scans” by binning all pixels in one direction from selected areas of the the EDS maps respectively.

4 Results

4.1 Morphology

4.1.1 Grains

The initial TEM analysis and acquired TEM BF images shown in this section indicates a pattern in grain morphology shown in figure 31 below. Grains consists of a $TiAl_3$ particle in the center of the grain with surrounding α-Al. Though the grains were of relatively equal size and shape, the $TiAl_3$ particles occurred in a variety of sizes and shapes. Smaller particles are mostly distributed along the GBs, with some found located within the α-Al matrix. The one exception shown in figure 32 below, showed a large agglomeration of smaller particles within a grain, with the grain itself being on the larger side.

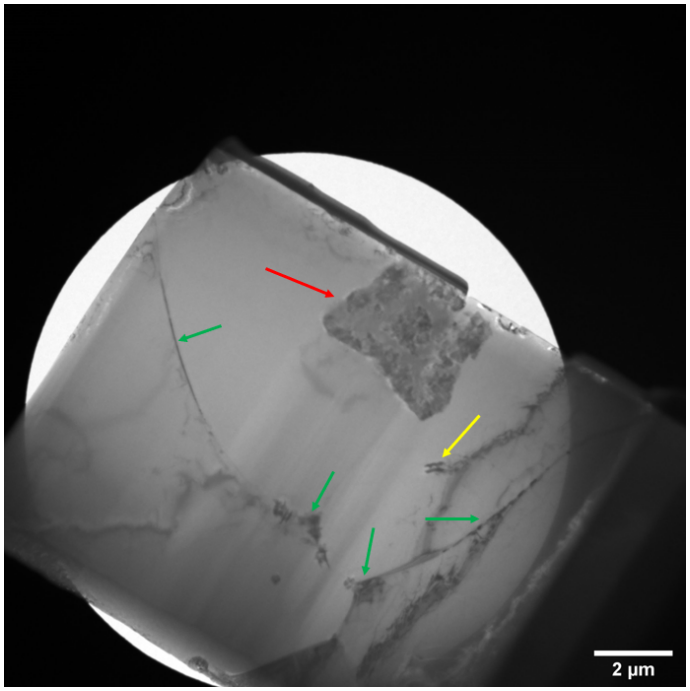

Figure 31: TEM BF image showing an overview of the typical grain morphology found. Red arrow points to the $TiAl_3$ particle in the center of the grain, yellow arrow points to a particle located inside the Al matrix, green arrows point to smaller particles located along the GB.

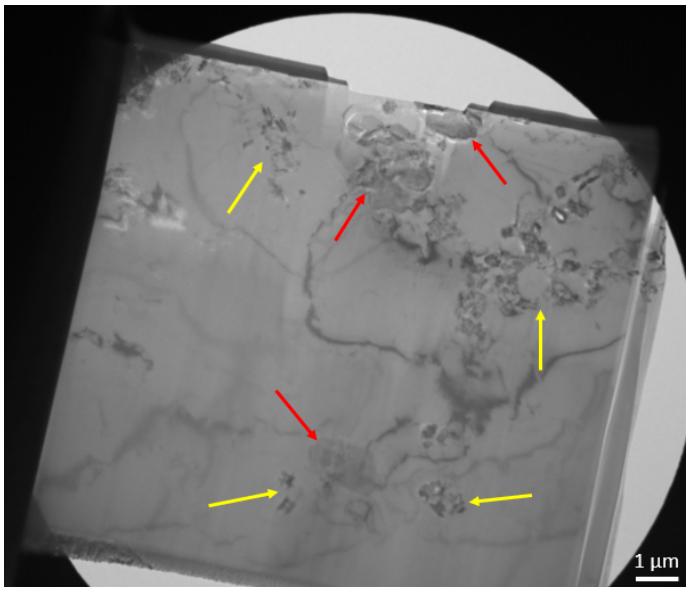

Figure 32: TEM BF image showing an overview of the untypical grain morphology found. Red arrows points to the $TiAl_3$ particles located at different sites in the Al matrix, yellow arrows points to the particle clusters located inside the Al matrix.

4.1.2 $TiAl_3$ particles

As mentioned above, the $TiAl_3$ particles found in the different samples were of a variety of sizes and shapes. Some had a visible core and shell, some were large, uniform particles, some seemed to be composed of smaller conjoined particles and some had irregular/incomplete shapes. An example of each is shown in the figure below.

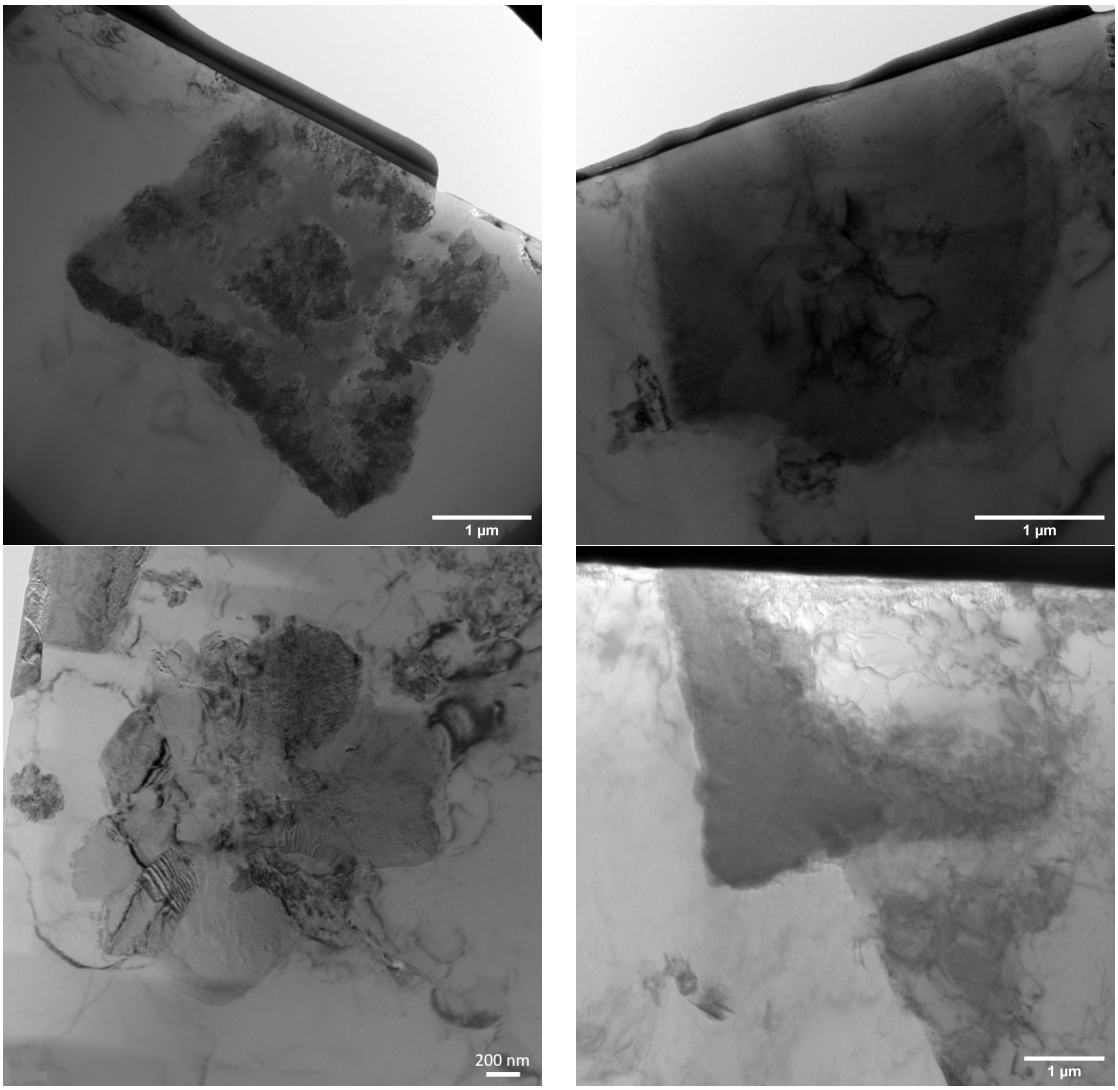

Figure 33: TEM BF images showing different types of $TiAl_3$ particles encountered. Top left: particle with a visible core and shell. Top right: large uniform particle. Bottom left: particle consisting of several smaller particles. Bottom right: irregular/incomplete particle.

4.1.3 Smaller particles

The smaller particles present in the samples were all of relatively similar size. The shape and composition however vary. They can in general be divided into five different shapes: butterfly-shaped particles, eye-shaped particles, square-shaped particles, plate/staff-shaped particles or particle agglomerations. The butterfly-shaped particle is characterized by a set of curved or straight "wings" grown from a center containing a smaller, bright particle (some of these are not visible, but this is most likely due to it having been removed during cleaning in the FIB). The eye-shaped particle is characterized by an oblong shape with a bright center and a darker shell. The size of the center relative to the shell varies, but this is most likely an effect caused by how far through the three-dimensional particle is reached during cleaning in the FIB. The square-shaped particle is characterized by four rounded staffs forming a square. The length of the staffs do in some particles exceed the limits of the square, forming a hashtag-like shape. The contents of the center vary, most likely due to the same effect mentioned for the

particle-types above. This type of particle seem closely related to the butterfly-shaped particle as some particles look to be somewhere in the middle between the two. The plate/staff-shaped particles are characterized by rectangles growing together parallel to each other. They were only found growing in groups. The particle agglomerations have no distinct shape. It is a collective term for the particles not complying to any of the particle-types mentioned above. They may be put together by several types of particles smudged together, obscuring any clear visible traits. They may be the remains of only the shell of other particles after cleaning. Or they might be an agglomeration of small particles not adhering to any clear shape. There was no clear preference found for where the different particles-types would locate themselves in the grain/GB. They were however rarely found as lone particles, they were most often found in groups or even conjoined, regardless of particle type and whether or not they were located in the Al matrix or along the GB.

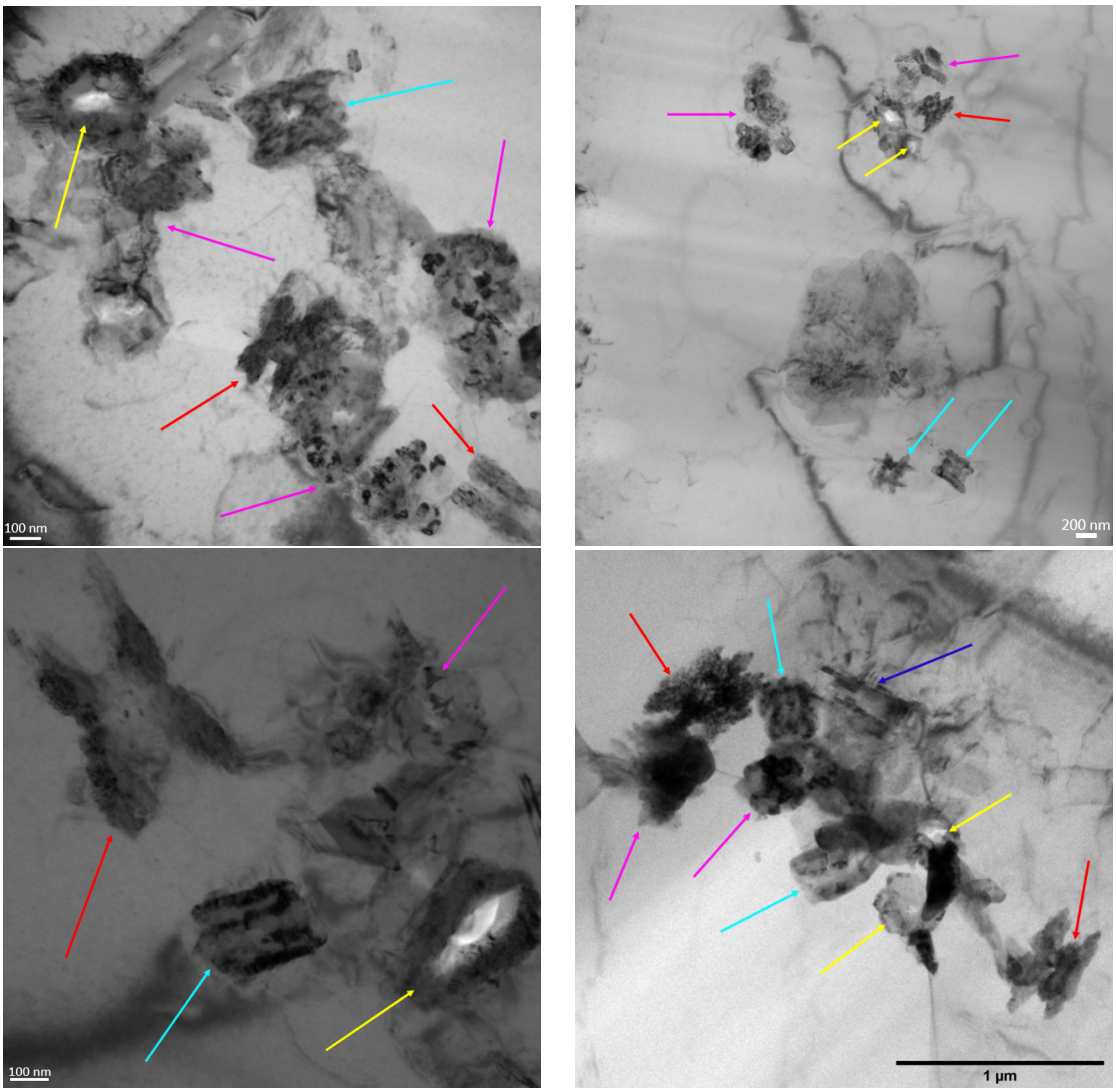

Figure 34: TEM BF images showing a variety of particles. Red arrows show butterfly-shaped particles. Yellow arrows show eye-shaped particles. Green arrows show square shaped particles. Blue arrows show plate/staff-shaped particles. Pink arrows show particle agglomerations.

4.2 EDS analysis

4.2.1 Qualitative maps

Qualitative EDS maps of selected particles showing the presence of Al, Ti, C, oxygen (O), iron (Fe), silicon (Si), manganese (Mn), magnesium (Mg), gallium (Ga) and copper (Cu) is shown below.

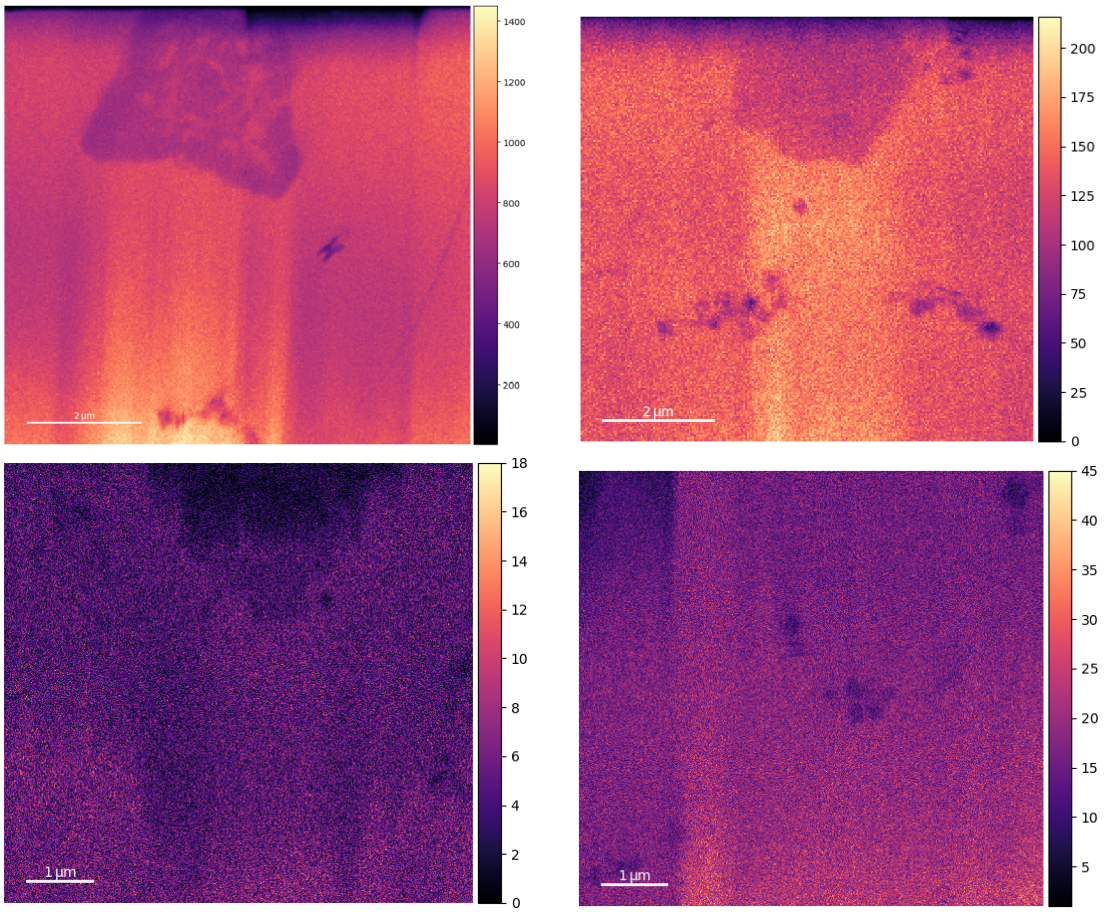

Figure 35: EDS maps showing intensity of Al Kα at 1.49 keV in different samples.

The figures above shows the presence of Al in the samples. It is found as α-Al in the grains and as part of the $TiAl_3$ particles.

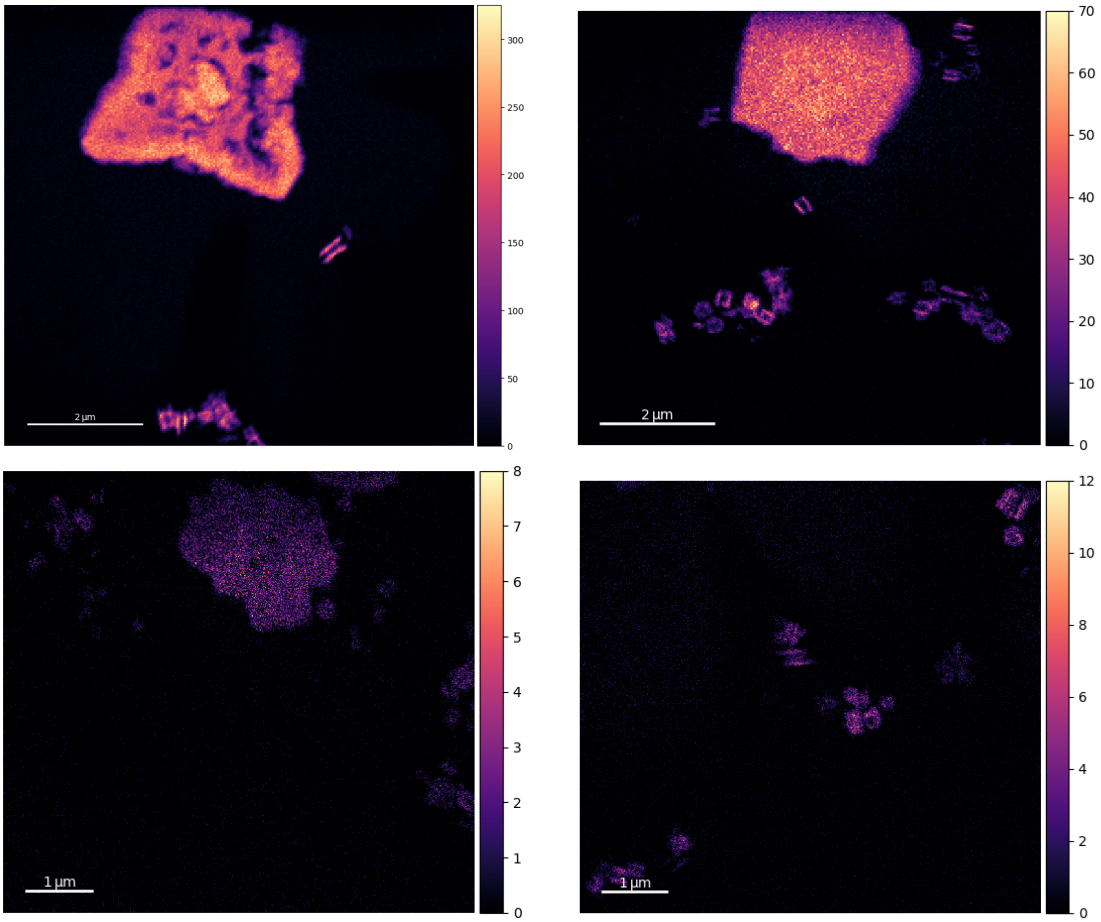

Figure 36: EDS maps showing intensity of Ti Kα at 4.51 keV in different samples.

The figures above shows the presence of Ti in the samples. It is found as part of the $TiAl_3$ particles in addition to being the element with highest intensity in most of the smaller particles both along GBs and within grains.

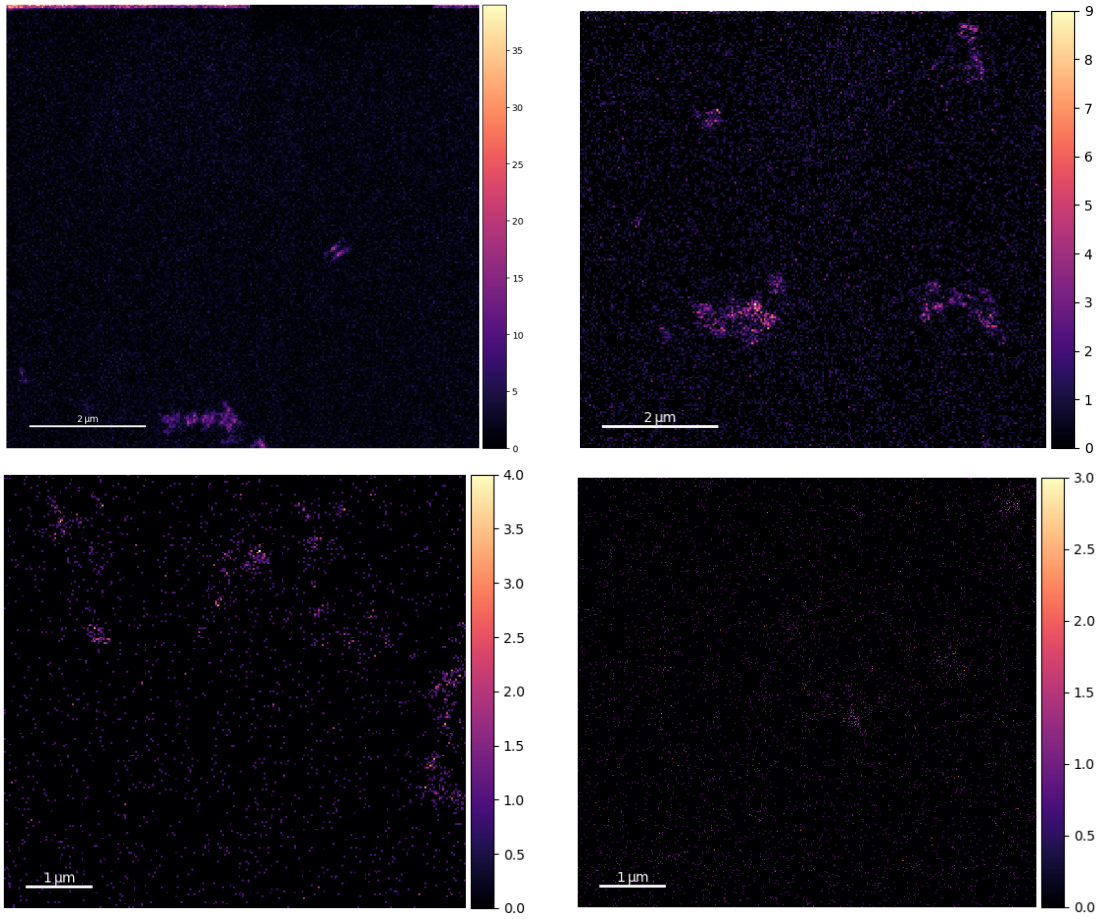

Figure 37: EDS maps showing intensity of C Kα at 0.28 keV in different samples.

The figures above shows the presence of C in the samples. It is found as part of the same smaller particles where Ti is found. In addition one sample showed a $TiAl_3$ particle which contained a high concentration of C in its center.

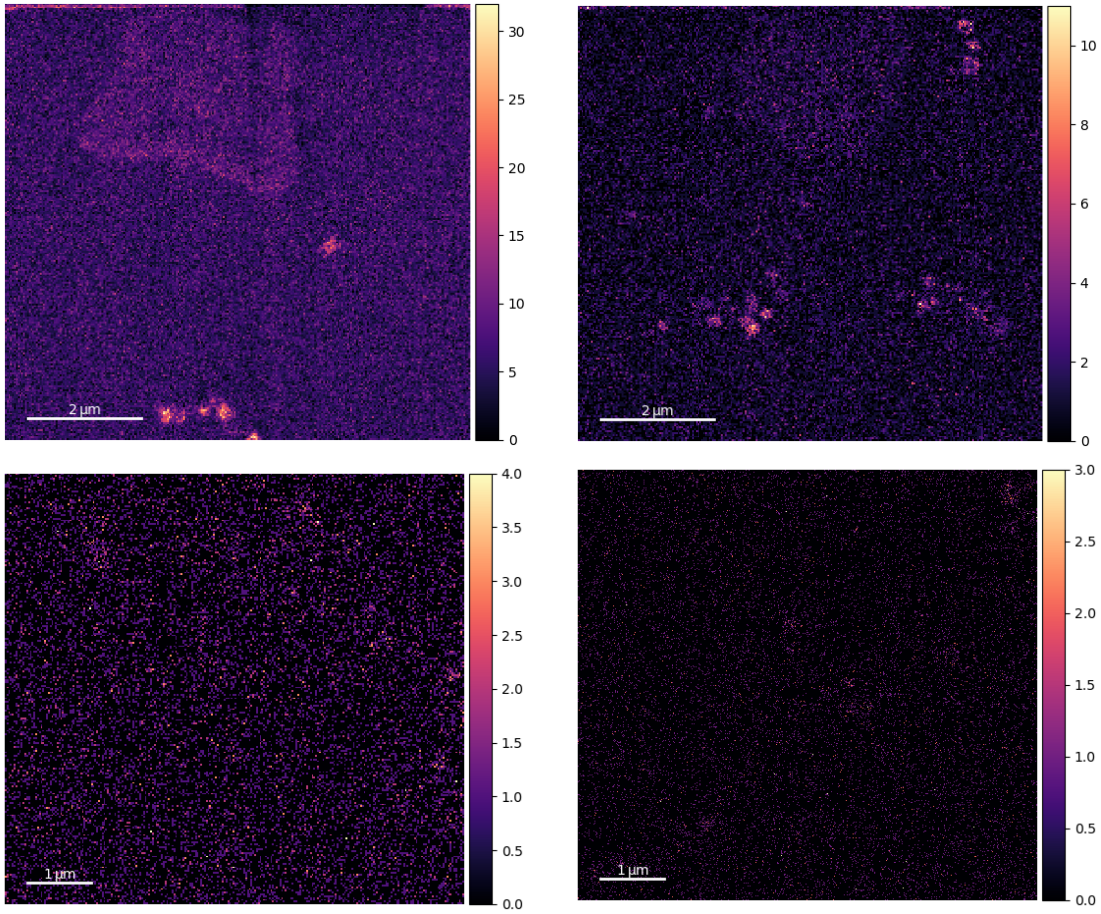

Figure 38: EDS maps showing intensity of O Kα at 0.52 keV in different samples.

The figures above shows the presence of O in the samples. It is found as part of the same smaller particles where Ti is found, in addition to having some intensity within the $TiAl_3$ particles.

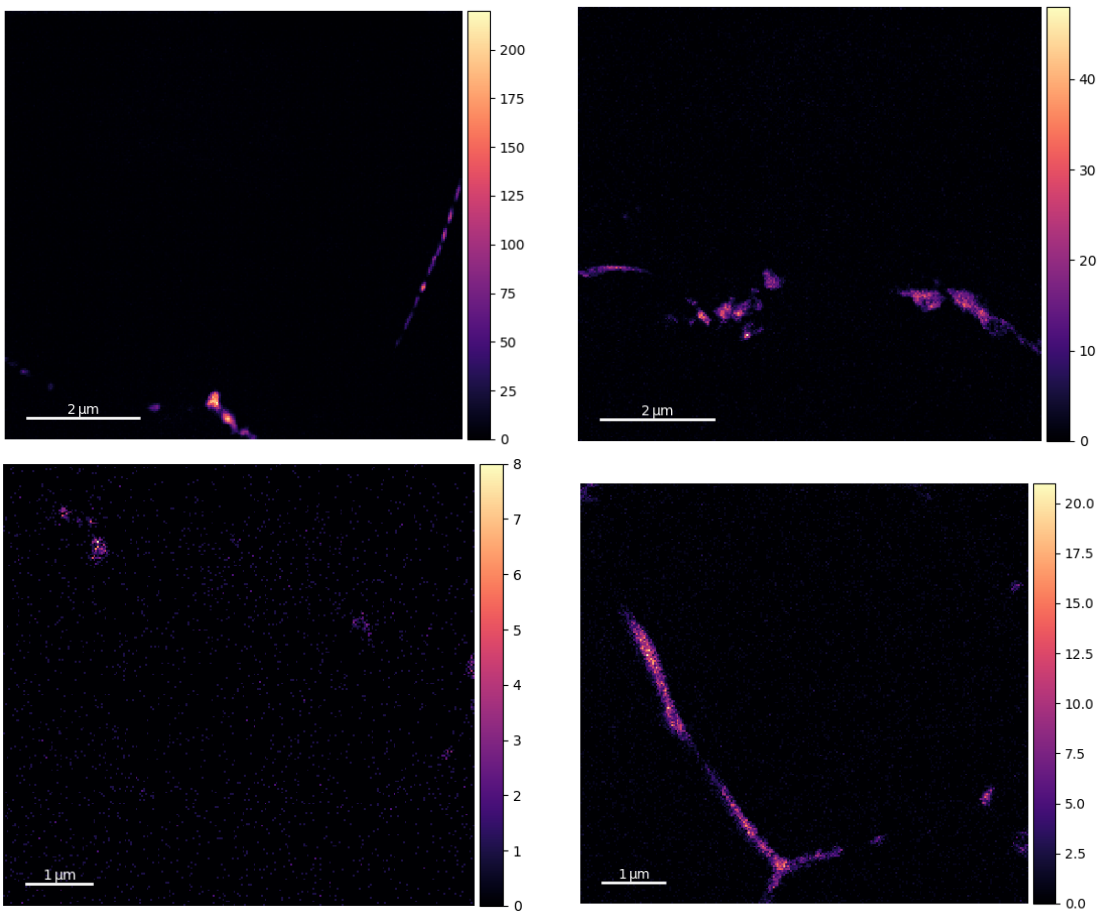

Figure 39: EDS maps showing intensity of Fe Kα at 6.40 keV in different samples.

The figures above shows the presence of Fe in the samples. It is found as a thin layer along GBs in addition to in smaller particles both along GBs and within grains.

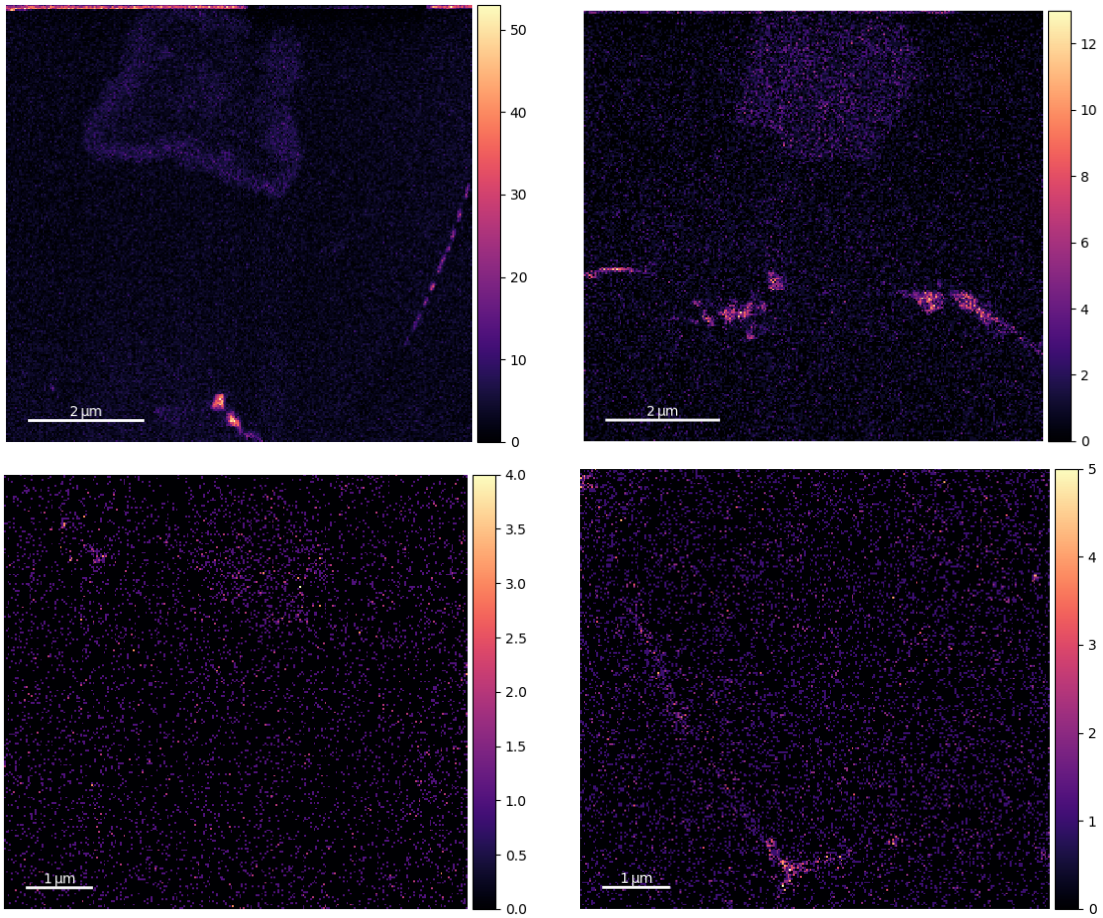

Figure 40: EDS maps showing intensity of Si Kα at 1.74 keV in different samples.

The figures above shows the presence of Si in the samples. It is found both in the same thin layers along GBs and in the smaller particles where Fe is found. There is also some intensity seen in the $TiAl_3$ particles.

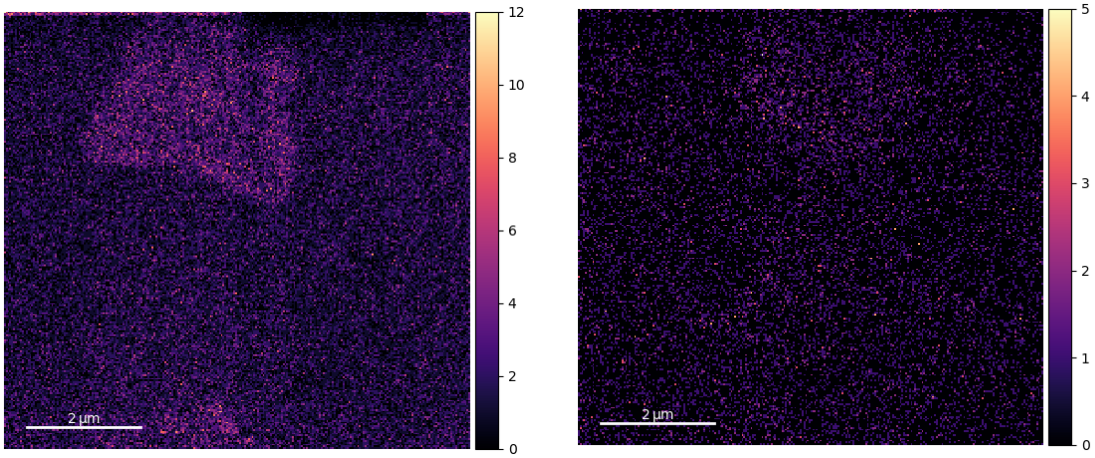

Figure 41: EDS maps showing intensity of Mn Kα at 5.90 keV in different samples.

The figures above shows the presence of Mn in the samples. It is found with slight intensity in both the $TiAl_3$ particles and some smaller particles.

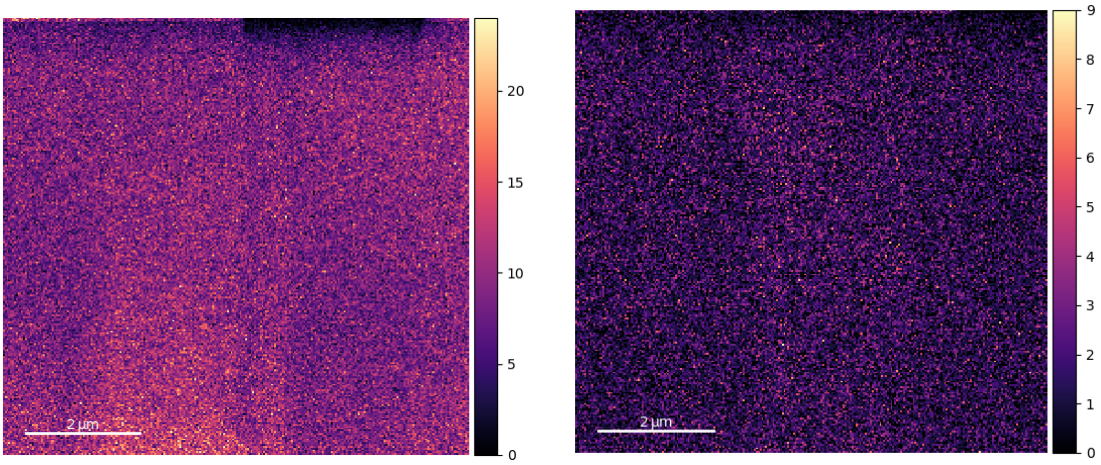

Figure 42: EDS maps showing intensity of Mg Kα at 1.25 keV in different samples.

The figures above shows the presence of Mg in the samples. It is found all around the sample with no clear preference towards any of the particles or the grain matrix.

Some of the elements found in the EDS scans are not naturally a part of the sample, at least not in the abundancy showed.

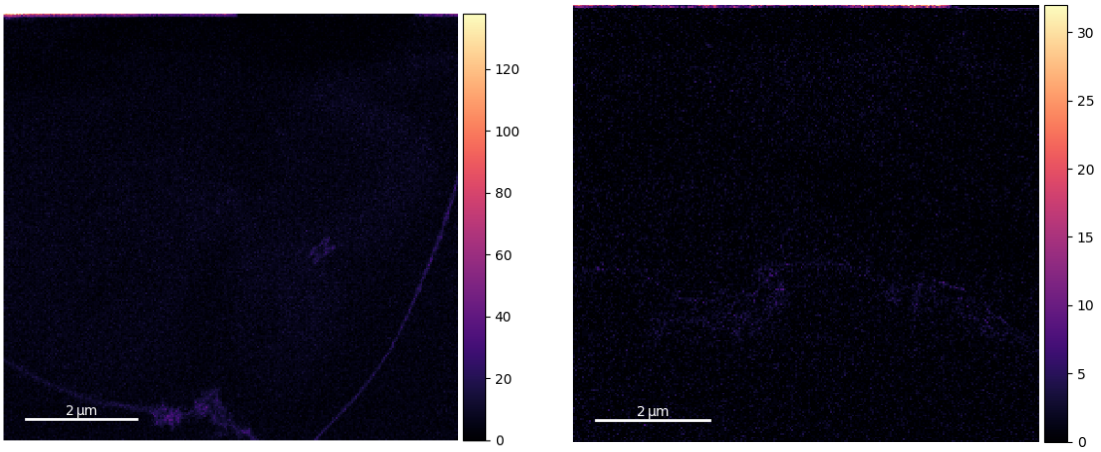

Figure 43: EDS maps showing intensity of Ga Kα at 9.25 keV in different samples.

The figure above shows the presence of Ga in the samples. The Ga present is a consequence of Ga poisoning that has occurred in the FIB. It is well known that this affects GBs, however it can also be seen to have affected the smaller particles.

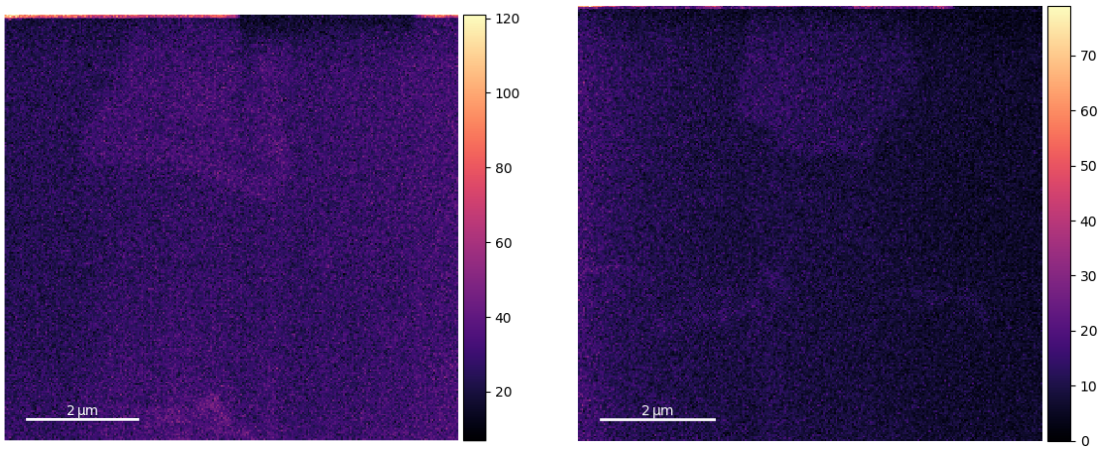

Figure 44: EDS maps showing intensity of Cu Kα at 8.05 keV in different samples.

The figure above shows the presence of Cu in the samples. There is a visible gradient with lower and lower intensity the further away from where the sample is connected to the Cu lift-out grid. This is probably a consequence of sputtering from the Cu grid having settled onto the sample.

4.2.2 Line scans

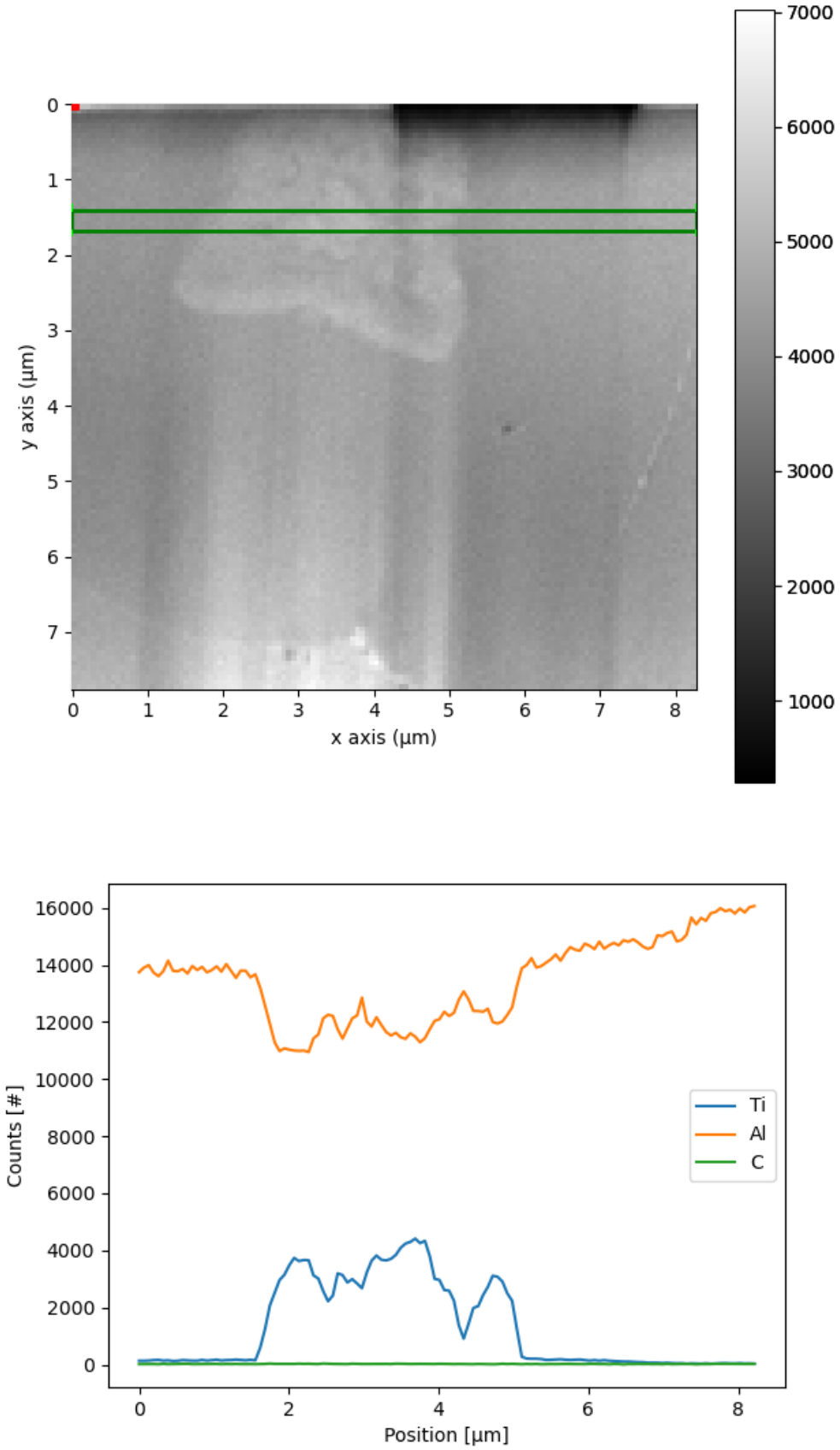

Figure 45: Line scan across shell and $TiAl_3$ particle showing intensity of Al, Ti and C.

Figure 45 above shows a line scan from within the green box in the upper figure. The line scan shown in the lower figure shows how the intensity of Al, Ti and C varies across the shell and core $TiAl_3$ particle. Ti has visible peaks in intensity at the shell and in the core, while the intensity of Al is lower. In the area in between the shell and the core, Al has visible peaks in intensity and the intensity of Ti is lower. The intensity of C shows no variation. This corresponds to the intensities visible in the EDS maps of the same particle.

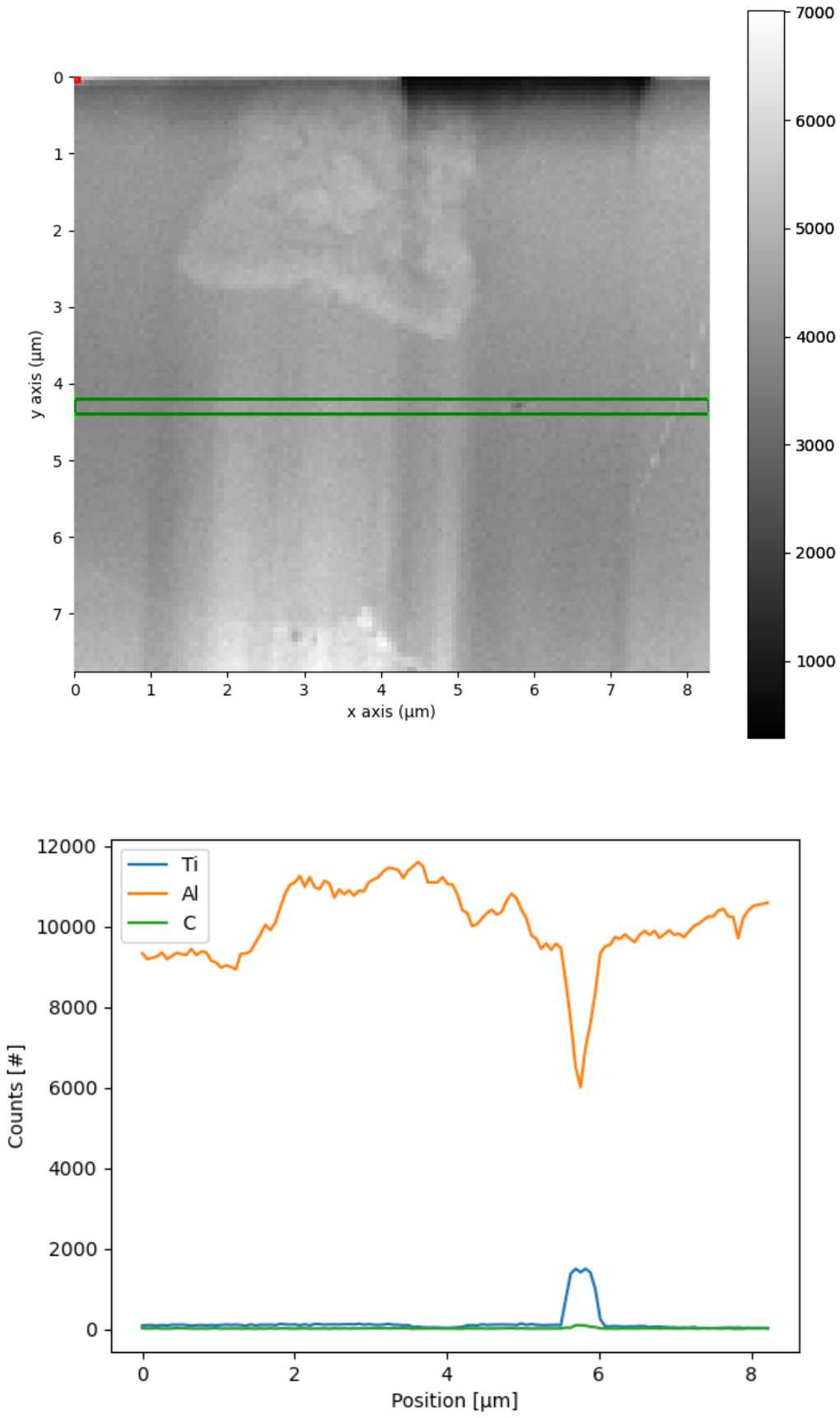

Figure 46: Line scan across a small particle particle showing intensity of Al, Ti and C.

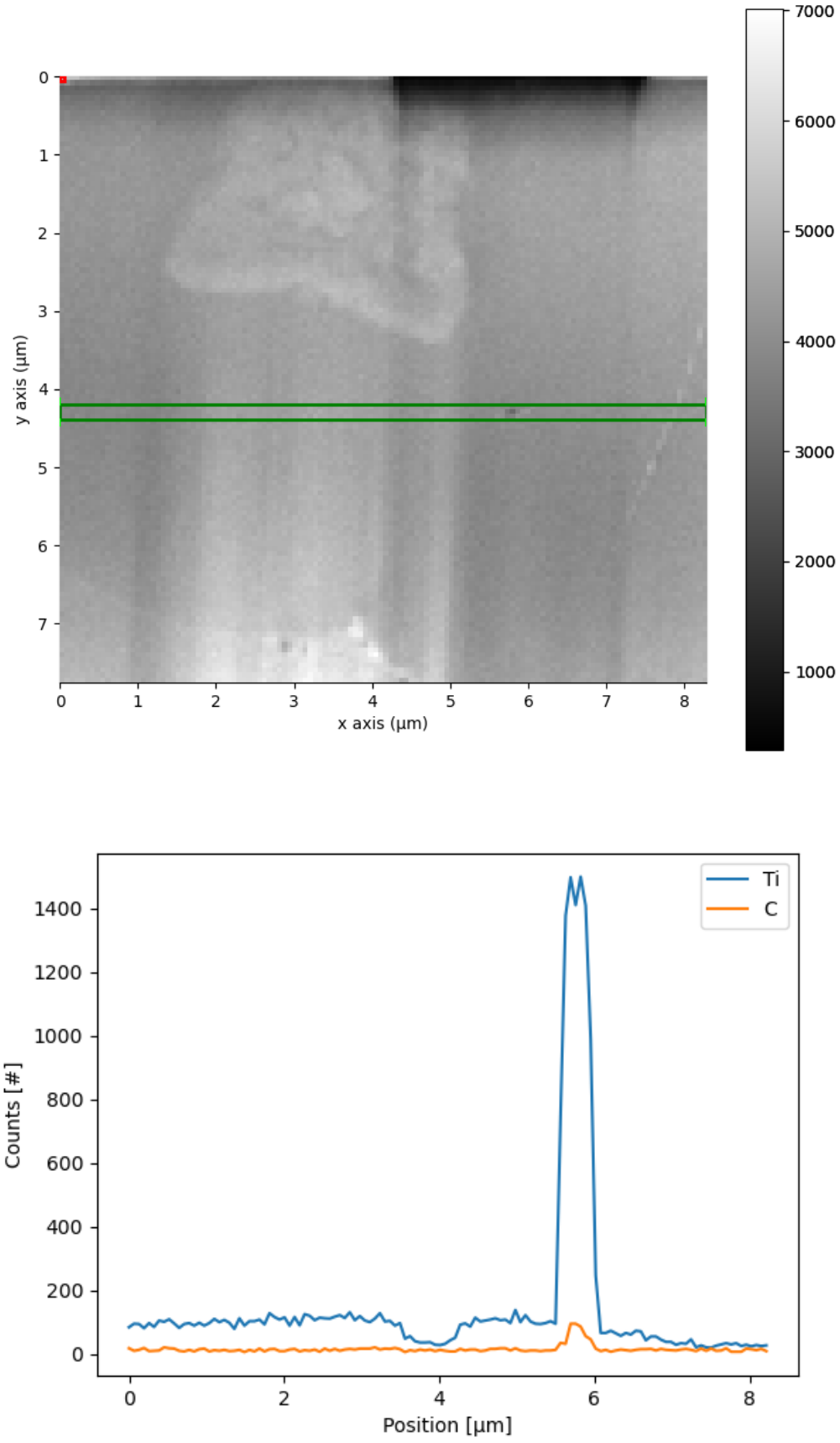

Figure 47: Line scan across a small particle particle showing intensity of Ti and C.

Figure 46 and 47 above shows a line scan from within the green box in the upper figure. The upper line scan shows how the intensity of Al, Ti and C varies and the lower line scan shows how the intensity of Ti and C varies across a small particle exhibiting C signals in the EDS maps. There is a large fall in intensity of Al and visible peaks in intensity of both Ti and C at the particle.

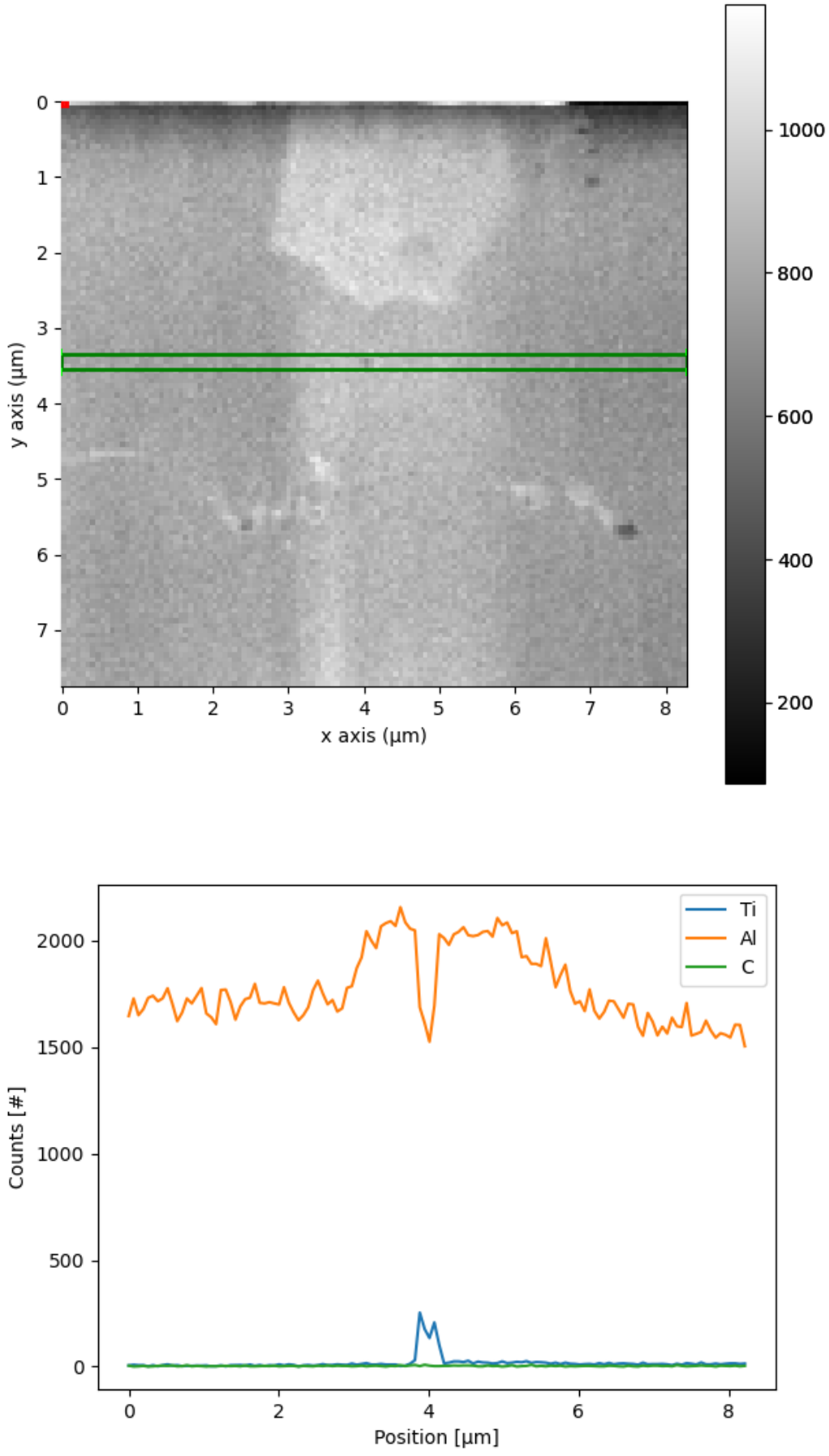

Figure 48: Line scan across a small particle showing intensity of Al, Ti and C.

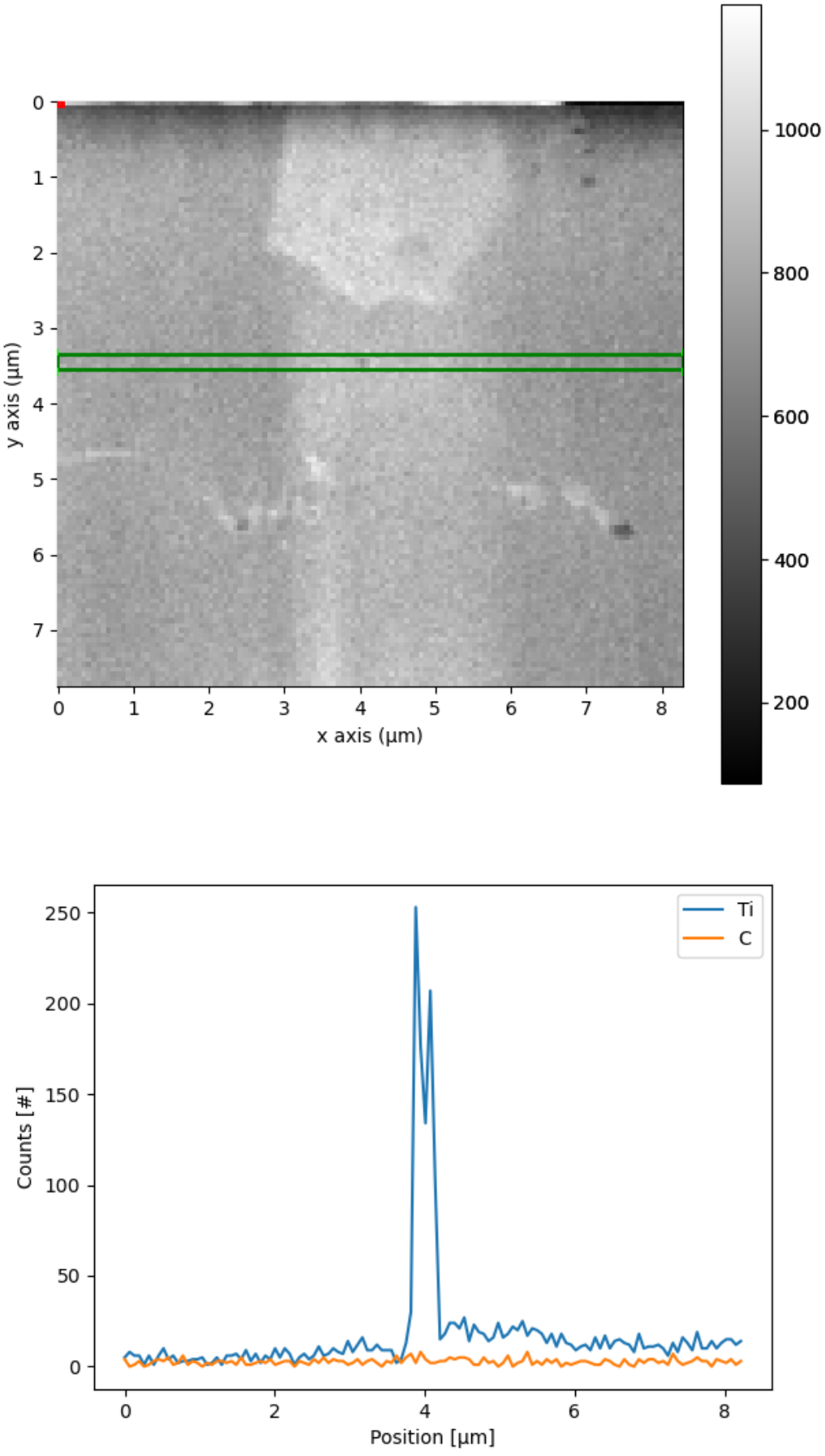

Figure 49: Line scan across a small particle showing intensity of Ti and C.

Figure 48 and 49 above shows a line scan from within the green box in the upper figure. The upper line scan shows how the intensity of Al, Ti and C varies and the lower line scan shows how the intensity of Ti and C varies across a small particle exhibiting no C signals in the EDS maps. There is a visible peak in intensity of Ti and no clear signal from C at the particle. There is also a fall in intensity of Al, however not as drastic as in the line scan across the particle exhibiting C signals.

5 Discussion

5.1 Morphology

5.1.1 Grains

Both the findings in the previous work by Kirkbakk [17] and the observations made during initial SEM inspection in this work, point to a typical grain morphology. It consists of α-Al with a $TiAl_3$ particle in the center, with most parts of smaller particles found along GBs, but some laying inside the Al matrix.

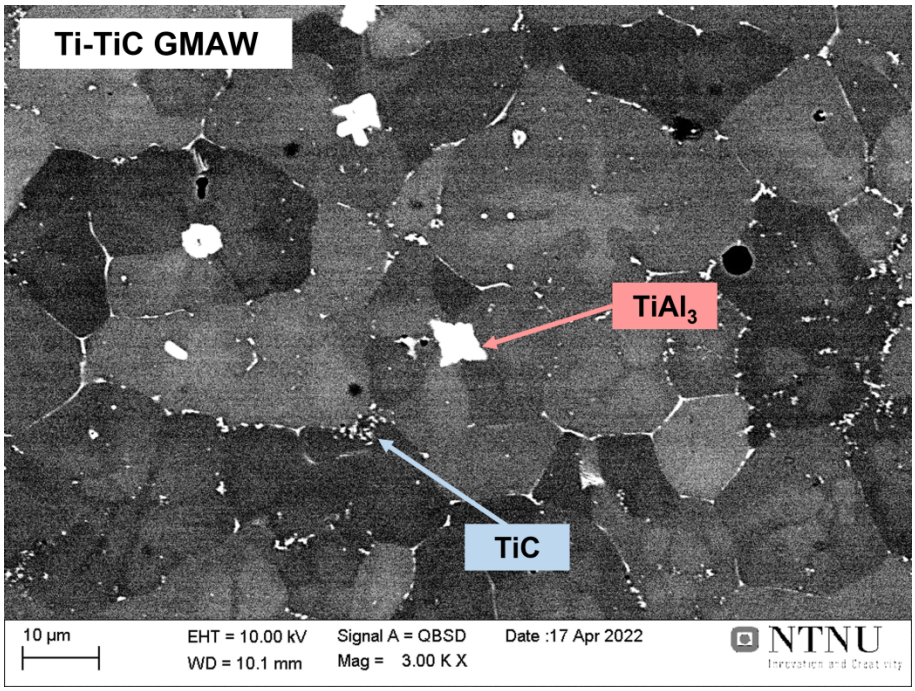

Figure 50: SEM BSE image showing the typical grain morphology. Reprinted from Kirkbakk [17].

However, some exceptions have been found. The first and most notable is the sample shown to the left in the figure below. In this sample there are no visible GBs, thus the grain from which the sample has been extracted is abnormally large. In addition, there are several smaller $TiAl_3$ particles spread around the sample with large amounts of smaller particles inside the Al matrix.

Another anomaly found is shown on the right in the figure below. This $TiAl_3$ particle resembles the core and shell particle in shape, though only half of it. There is also a GB running straight through the particle, and interestingly there is a smaller $TiAl_3$ particle laying on the other side of the grain running through the particle. Thus it is possible to assume that it at some point was a whole particle which was torn apart by the growth of the central grain.

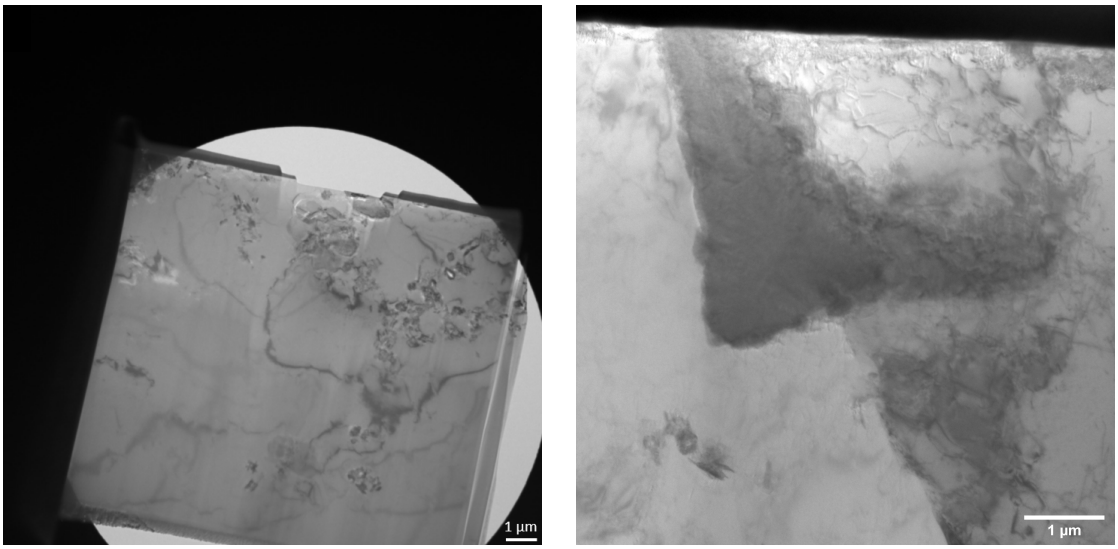

Figure 51: TEM BF images of the samples found to not adhere to the typical grain morphology.

5.1.2 $TiAl_3$ particles

A 2016 study by Zhao et al. [46] investigated the varying $TiAl_3$ morphologies in commercial-purity Al with additions of Al-4Ti master alloy. They found three different morphologies, petal-like particles, blocky particles and flaky particles. Their formation were closely related to the melt temperature and cooling rate. Petal-like particles were more likely to form at low melt temperatures and high cooling rates, blocky particles were more likely to form at low melt temperatures and medium cooling rates and flaky particles were more likely to form at high melt temperatures and low cooling rates. No flaky particles have been found in this work, which is logical considering the high cooling rates in welding.

The shape of the core and shell particle is visible in the figure below. The shape coheres well with the petal-like particles noted by Zhao et al. [46]. The EDS maps for the variation of Al and Ti is shown below. The full EDS map shown in Appendix A.1 shows the complexity of the core and shell $TiAl_3$ particle. The core and shell appear to have a very similar composition. They contain a concentrated amount of both Cu, Mn, O and Si, in addition to the highest concentration of Ti and lowest concentration of Al. The area in between the core and shell is an area containing a non-uniform mix of Al and Ti, the concentration of Cu, Mn, O and Si appear to be approximately at which the concentration they exist in the surrounding Al matrix.

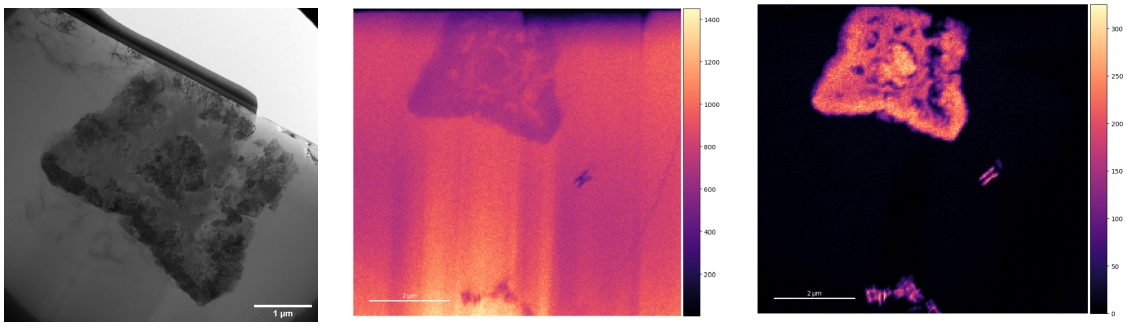

Figure 52: TEM BF image of the shell and core $TiAl_3$ particle with its EDS maps containing Al and Ti respectively.

The shape of the uniform particle is visible in the figure below. The particle shape is similar to the blocky particles found by Zhao et al. [46]. The EDS maps for the variation of Al and Ti is shown below. The full composition is seen in Appendix A.2. It is evident that the entire particle is composed of the same elements as those found in the core and shell of the particle discussed above. There is also a visible gradient of Ti and Al from the center and out of the particle. Ti has its highest intensity at the center of the particle which fades towards the edge. Al has its lowest intensity at the center of the particle and intensifies towards the edge.

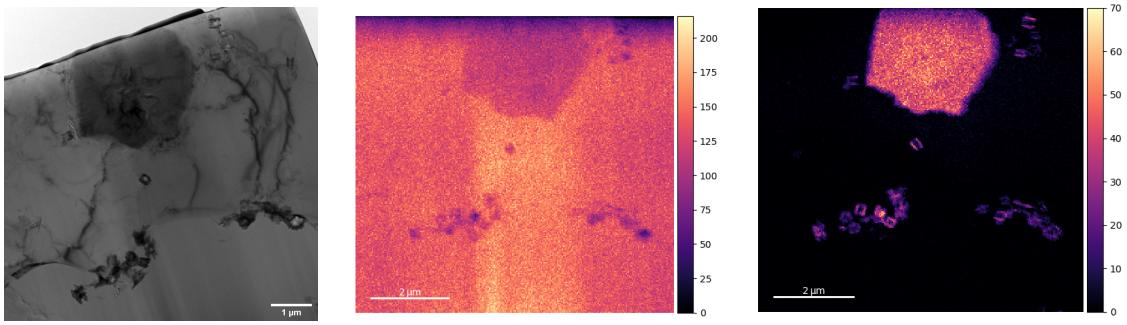

Figure 53: TEM BF image of the uniform $TiAl_3$ particle with its EDS maps containing Al and Ti respectively.

The shape of the conjoined particle is visible in the figure below. The petal-like particles described by Zhao et al. [46] also describes the shape of this particle. Some of the particles they found were on the smaller side. And since they are three dimensional objects, by cutting into them at skewed angles the number of "petals" visible in the two dimensional slice is misleading. Though this does not account for the other, smaller $TiAl_3$ particles found in the sample. The EDS maps for the variation of Al and Ti is shown below. The full composition can be seen in Appendix A.3. It shows signals similar to the particle discussed above, however with no clear gradients. It also exhibits clear C signals from within the center of the $TiAl_3$ particle agglomeration.

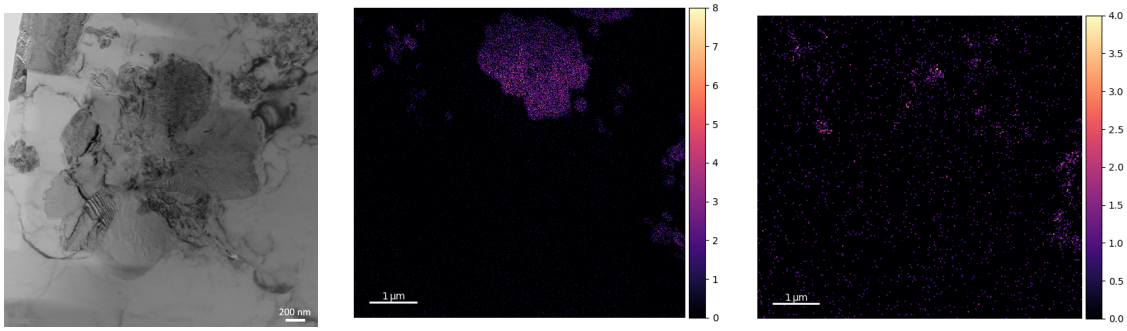

Figure 54: TEM BF image of the uniform $TiAl_3$ particle with its EDS maps containing Ti and C respectively.

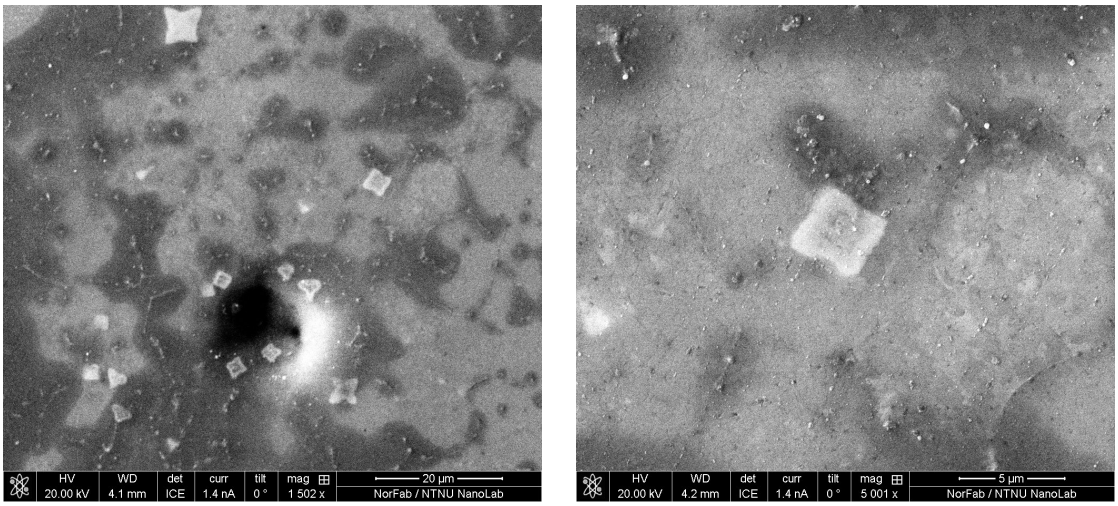

Figure 55: FIB SEM images of $TiAl_3$ particles.

The figure above shows SEM images taken in the FIB. Many of the particles present has the same petal-like shape as the shell and core particle. The right side image shows one of the particles at higher magnification, there is a visible dark outline of a square within the particle. This is most likely a phase rich in aluminium, same as was found in the shell and core particle. Almost all these petal-like particles has a dark square inside it, thus it logical that they have all been formed in the same way.

5.1.3 Smaller particles

As mentioned earlier, the smaller particles across all samples show a tendency of appearing in clusters. This is seen both along GBs and within the matrix, with lone particles being a rare occurrence. This does most likely stem from a non-uniform dispersion of particles in the FW, however it is possible that they have agglomerated further in the weld pool.

Most of the smaller particles found across all samples show signals of both Ti and C, which is a clear sign that these are TiC particles. These do also show O signals, example shown in the figure below, however this is probably a result of the TiC NPs having been contaminated during the production process. It shows that there is still a way to go in the aim of keeping the entire production process as inert as possible with regards to the method developed in the previous thesis by Kirkbakk [17]. However, this will not be elucidated further in this thesis.

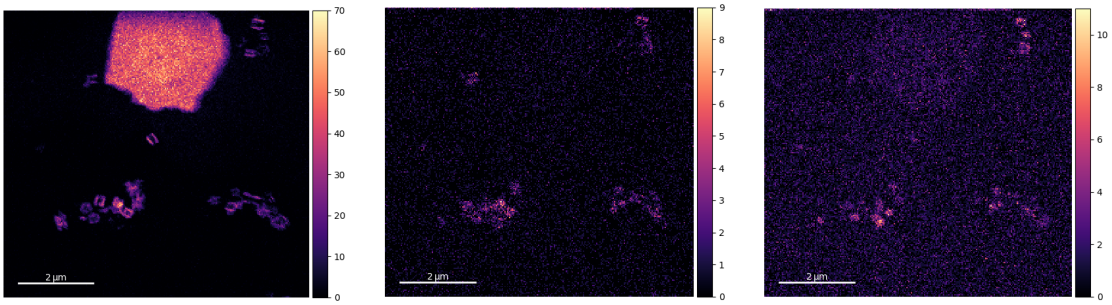

Figure 56: EDS maps showing the presence of Ti, C and O in small particles.

Another observation from the EDS maps is the variable intensity of Ti and Al in the smaller particles, indicating the presence of $AlTi_3$. As shown in the line scans below, some of these particles show C signals, and some do not, indicating both $AlTi_3$ present as small, lone particles and $AlTi_3$ growing on TiC particles. Though the signs of $AlTi_3$ growing on TiC particles may be a result of slight overlapping in the particle agglomerations.

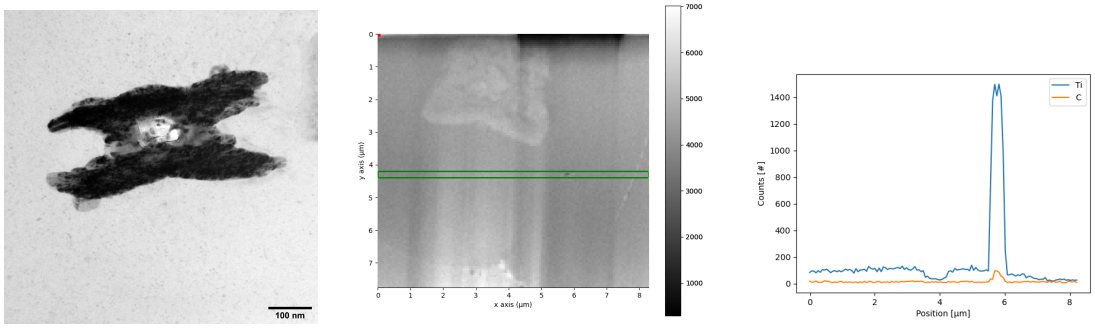

Figure 57: TEM BF image of a small particle with line scans showing the presence of Ti and C.

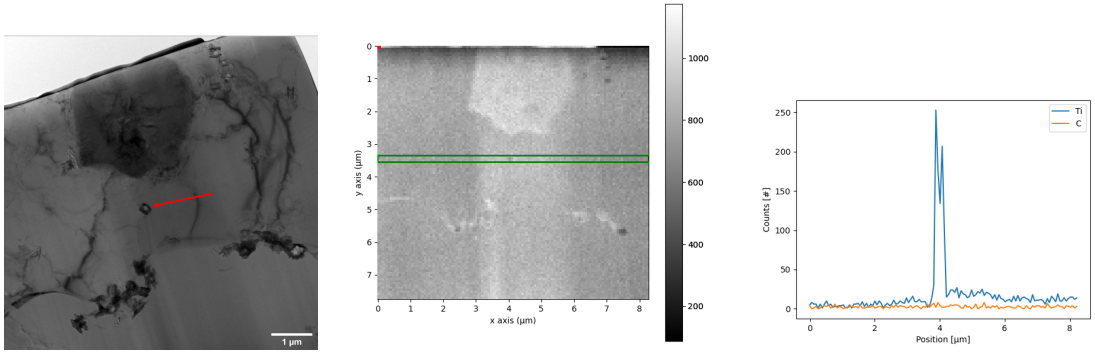

Figure 58: TEM BF image of a small particle with its line scans showing the presence of Ti and C.

Besides the TiC particles, Fe particles containing Si were also found. Fe and Si are the most abundant alloying elements in both the base alloy for the FW AA1370 and in the AA1050 weld sheets. They do however occur in two different forms, as near continuous, thin layers along GBs and as particles in the size range of the TiC particles.

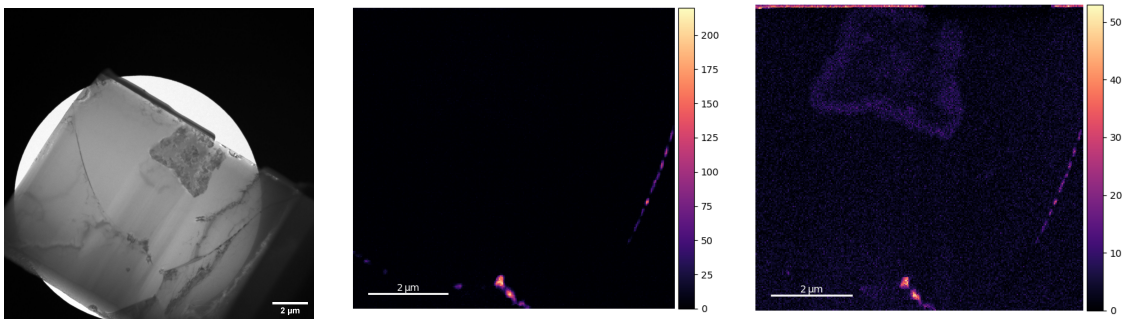

Figure 59: TEM BF image of an area containing both continuous layers and particles consisting of Fe and Si in addition to EDS maps containing Fe and Si from the same area.

These particles are also found in all the same regions as the TiC particles can be found, though they

seem to have a clearer tendency to situate themselves along GBs. These particles also show slight Mn signals which are not found in the layers. This suggests that there is difference in the origin of the two types of particles. The thin layer is composed of the Fe and Si originally present in the base alloy and weld sheets which has formed iron precipitates along the GBs during solidification. Meanwhile, the other particles might have been introduced during the screw extrusion process. As it is possible that small steel particles from the die has come loose and become part of the FW. Thus, their behavior resembles more that of the TiC particles.

5.2 Role of TiC NPs

In the thesis by Kirkbakk [17], during which the samples used in this thesis was produced, the TiC NPs were added supported by Ti powder with the intent of them functioning as nucleating particles. As an EDS scan in a SEM showed the presence of C in the center of a $TiAl_3$ particle surrounded by a chrysanthemum-like structure, the nucleation mechanism was suggested to most likely follow the Ti transition zone theory [27]. However, there were also samples produced with only Ti added in the FW. Also here were chrysanthemum-like structures around $TiAl_3$ particles present, though not to the same degree as in the TiC/Ti samples, in addition to containing considerably larger grains. Thus, the segregating effect of Ti in the melt [29] is clearly an important part of the grain refining effect, however without the added effect of the TiC particles it is less effective.

Worth noting is the amount of TiC NPs added to the original FW compared to that found in the samples, which is a lot less. This means that much of the TiC has dissolved in the weld pool forming more solute Ti and possibly some C phases (not found specifically). In addition, during the work by Kirkbakk [17], the TiC NPs were found to agglomerate within pores. Thus, very few of the added NPs actually contribute to the grain refining effect.

Recently, there have been works on improving the arc-weldability of heat treatable Al alloys using TiC nano-treated FW [2, 36, 37]. Similarly to those, this work has found the addition of TiC NPs to promote small, equiaxed grains. The effect was attributed to the TiC NP's ability to promote a higher degree of undercooling, nucleate grains and restrict the growth of grains during solidification.

In this work, no decisive evidence of TiC having nucleated a large $TiAl_3$ particle has been found. However, as mentioned earlier, there are signs of $TiAl_3$ on TiC particles given the variable intensity of Ti and Al across some smaller particles. This does point to the fact that $TiAl_3$ can nucleate on TiC particles which can further nucleate α-Al, as the Ti transition zone theory suggests. There are also the weak C signals present inside the conjoined $TiAl_3$ particle, which could lead to think that the particle had nucleated on a TiC particle agglomeration. Though given the weakness of the signal and the abnormalities in the sample in general, there is not enough evidence to give a clear answer. However, as there are small $TiAl_3$ particles present which has formed without the assistance of TiC, it also suggests that not all large $TiAl_3$ particles have nucleated on TiC particles.

Most of the TiC particles found in this work has been located along GBs. Thus, it is logical to assume that they have restricted the growth of grains during solidification. This is supported by the work by Zhao et al. [34], suggesting that the primary role of TiC NPs in grain refining

is growth restriction. Though they did attribute some of the effect to TiC NPs with preferable orientation to have acted as nucleating particles, however without experimental evidence. They found a relatively thick layer of TiC NPs along GBs with very few contained inside the Al matrix, contrary to the dispersed particles found in this work. Another similar work by Wang et al. [35] also found their TiCN NPs to primarily situate themselves as layers along GBs and reached the same conclusion. However, these works investigated castings, in which cooling is a much slower process than for welding. Thus, it is natural to assume that the amount of smaller particles found within the matrix during this work got caught within it during the rapid solidification.

A newer study by Wang et al. [47] investigated laser welded 6061 Al alloy joints with a Ti_3AlC_2 additive. The Ti_3AlC_2 additive was found to break down and form Al, $TiAl_3$ and TiC upon contact with the Al melt. They found TiC particles distributed along GBs and $TiAl_3$ phases inside grains. Thus, they concluded that the nucleation of Al grains would occur on $TiAl_3$ prior to TiC and the growing grains would push the TiC particles to the GBs while the $TiAl_3$ phase would remain at the grain center. This is a reasonable conclusion with regards to the more preferable orientation relationship between α-Al and $TiAl_3$ than that of α-Al and TiC [33]. Considering the similar morphology found during this work, in addition to the smaller $TiAl_3$ particles present in the sample, it is likely that the grains have grown in a similar fashion.

The pinning effect is further strengthened by the presence of the iron precipitates. As is evident in the work by Langelandsvik et al. [48] investigating heat treated AA1370 wire conductors produced via MSE. They found Fe-rich precipitates to form at GBs during heat treatment and refine grains through growth restriction. This is the same Al alloy used in the FW in this work, and though the extent of iron precipitation during solid solution heat treatment can be expected to be much higher, the EDS results show similar iron precipitates present in the samples produced during this work.

6 Conclusion

This study examined the nucleation and effect of TiC NPs in Al WM inoculated using a FW containing TiC NPs supported by Ti powder produced by MSE. In order to investigate, several site specific FIB TEM lamellas were produced. These samples were characterized using different TEM techniques.

The α-Al grains were found to have nucleated on 3-5 µm $TiAl_3$ particles which had precipitated and grown as petal-like and blocky particles. According to the Ti transition zone theory, the $TiAl_3$ particles should have nucleated on TiC particles. Though no decisive evidence of this was found, it is a highly likely scenario that some preferably orientated TiC NPs have nucleated $TiAl_3$ particles, as most of the literature discussed suggests. However, given the finds of smaller $TiAl_3$ particles in the samples and their higher potency as nucleating particles compared to TiC particles, the large $TiAl_3$ particles are more likely to have grown from smaller, precipitated $TiAl_3$, which have then nucleated the α-Al.

Another important contribution to the grain refining effect can be attributed to the segregating effect of Ti in the melt and the resulting strong constitutional undercooling in the solid/liquid interface. This zone containing high concentrations of solute Ti is also likely to have contributed to the growth of the petal-like and blocky $TiAl_3$ particles.

The TiC NPs were primarily found along GBs. The NPs were thought to have been relatively uniformly distributed in the FW, however the clustering found does not conform to that theory. During growth of the α-Al they seem to have been pushed outward by the solidifying front, settling at and pinning the GBs. Thereby restricting the growth of grains during solidification. This pinning effect was further strengthened by the formation of Fe precipitates.

Through comparison with similar studies, the grain refining effect of TiC NPs supported by Ti powder can be thought to stem from a combination of the segregating effect of Ti, the precipitation of small $TiAl_3$ particles in the weld pool and their orientation relationship with α-Al creating ideal nucleation sites, and the growth restricting effect of TiC NPs. Though the primary role of TiC NPs seem to have been growth restriction, some preferably oriented particles have most likely nucleated $TiAl_3$ particles which in turn has nucleated α-Al grains.

7 Future work

Though this work found some signs of smaller $TiAl_3$ particles growing on TiC NPs, this was inconclusive due to the high likelihood of this simply being overlapping particles. This is worth looking into further, as finding $TiAl_3$ growing on TiC NPs in "small scale" shows the feasibility of the phenomena. In addition, the probability of finding a single TiC particle inside a large $TiAl_3$ particle at the exact plane uncovered while producing a TEM lamella is very low. To solve these issues, more statistics is important. Thus, the efficient production of samples is the most important parameter. This would be much easier to achieve using a more modern, more time-efficient FIB, as the one used during this work is on the older side and has its quirks.

Bibliography

[1] T. Dursun and C. Soutis. 'Recent developments in advanced aircraft aluminium alloys'. In: *Materials Design (1980-2015)* 56 (2014). DOI: https://doi.org/10.1016/j.matdes.2013.12.002.

[2] S. Pan M. Sokoluk C. Cao and X. Li. 'Nanoparticle-enabled phase control for arc welding of unweldable aluminum alloy 7075'. In: *Nature communications* 10 (2019). DOI: https://doi.org/10.1038/s41467-018-07989-y.

[3] J. Galos et al. 'Reducing the energy consumption of heavy goods vehicles through the application of lightweight trailers: Fleet case studies'. In: *Transportation Research Part D: Transport and Environment* 41 (2015), pp. 40–49. DOI: https://doi.org/10.1016/j.trd.2015.09.010.

[4] D. Blanco et al. 'Sustainable Processes in Aluminium, Magnesium, and Titanium Alloys Applied to the Transport Sector: A Review'. In: *Sustainable Manufacturing of Light Alloys* 12 (2022). DOI: https://doi.org/10.3390/met12010009.

[5] F. Czerwinski. 'Lightweight Structural Materials for Automotive and Aerospace'. In: *Sustainable Manufacturing of Light Alloys* 12 (2022). DOI: https://doi.org/10.3390/ma15207089.

[6] G. Mathers. *The Welding of Aluminium and Its Alloys*. Woodhead publishing limited, 2002.

[7] et al. K.B. Nie. 'Microstructure and tensile properties of micro-SiC particles reinforced magnesium matrix composites produced by semisolid stirring assisted ultrasonic vibration'. In: *Mater. Sci. Eng. A* 528 (2011), pp. 8709–8714. DOI: https://doi.org/10.1016/j.msea.2011.08.035.

[8] J. I. Rojas et al. 'Viscoelastic behavior of a novel aluminum metal matrix composite and comparison with pure aluminum, aluminum alloys, and a composite made of Al–Mg–Si alloy reinforced with SiC particles'. In: *Journal of Alloys and Compounds* 744 (2018), pp. 445–452. DOI: https://doi.org/10.1016/j.jallcom.2018.02.103.

[9] K. H. Reddy and V. K. Chintamreddy. *Advances in Material Science and Mechanical Engineering*. Trans Tech Publications Ltd, 2021.

[10] R. Palanichamy et al. 'Investigation of Microstructural, Mechanical and Tribological Properties of Al8011-TiC Metal Matrix Nano-Composites'. In: *International Journal of Vehicle Structures Systems* 14 (2022), pp. 323–327. DOI: https://doi.org/10.4273/ijvss.14.3.07.

[11] Y. Cheng et al. 'Effect of TiC/TiC–TiB2 on microstructure and mechanical properties of spray formed 7055 aluminum alloy TIG welded joints'. In: *Journal of Materials Research and Technology* 15 (2021). DOI: https://doi.org/10.1016/j.jmrt.2021.08.146.

[12] M. Fattahi et al. 'Fabrication of aluminum TIG welding filler rods reinforced by ZrO2/reduced graphene oxide hybrid nanoparticles via accumulative roll bonding'. In: *Diamond and Related Materials* 99 (2019). DOI: https://doi.org/10.1016/j.diamond.2019.107518.

[13] T. Huang et al. 'Appropriate amount of TiB2 particles causes the ductile fracture of the un-weldable spray-formed 7055 aluminium alloy TIG-welded joint'. In: *Materials Research Express* 8 (2021). DOI: https://doi.org/10.1088/2053-1591/ac2194.

[14] 'Screw extruder for continuous extrusion of materials with high viscosity'. In: International patent number EP2086697B1 WO2008 06307 (2008).

[15] G. Langelandsvik. 'Wire Arc Additive Manufacturing of Aluminium Alloys: Microstructural Refinement and Alloy Development'. In: (2021).

[16] O. M. Akselsen G. Langelandsvik M. Eriksson and H. J. Roven. 'Wire arc additive manufacturing of AA5183 with TiC nanoparticles'. In: *The International Journal of Advanced Manufacturing Technology* 119 (2022), pp. 1047–1058. DOI: https://doi.org/10.1007/s00170-021-08287-6.

[17] K. M. Kirkbakk. 'Aluminum weld metal inoculation byTi/TiB2/TiC additions to screw extruded filler wires'. In: (2022).

[18] S. Kou and Y. Le. 'Nucleation mechanism and grain refining of weld metal'. In: *Welding Journal* 65 (1986), pp. 65–70.

[19] P. Schempp et al. 'Influence of grain size on mechanical properties of aluminium GTA weld metal'. In: *Welding in the World* 57 (2013), pp. 293–304. DOI: https://doi.org/10.1007/s40194-013-0026-6.

[20] W. Kurz and D. J. Fisher. *Fundamentals of solidification*. 1984.

[21] D. H. StJohn M. A. Easton A. Prasad and M. Qian. 'The Contribution of Constitutional Supercooling to Nucleation and Grain Formation'. In: *Metallurgical and Materials Transactions A* 46 (2015), pp. 4868–4885. DOI: https://doi.org/10.1007/s11661-015-2960-y.

[22] M. A. Easton and D. H. StJohn. 'A model of grain refinement incorporating alloy constitution and potency of heterogeneous nucleant particles'. In: *Acta Materialia* 49 (2001), pp. 1867–1878. DOI: https://doi.org/10.1016/S1359-6454(00)00368-2.

[23] K. Toshiro K. Akio O. Atsushi and T. Hiroyuki. 'Compounding of nano-sized SiC particles into aluminum alloys by molten metal stirring method'. In: *J. Jpn. Inst. LightMet.* 49 (1999), pp. 149–154. DOI: https://doi.org/10.2464/jilm.49.149.

[24] S.C. Tjong. 'Novel Nanoparticle-Reinforced Metal Matrix Composites with Enhanced Mechanical Properties'. In: *Advanced engineering materials* 9 (2007), pp. 639–652. DOI: https://doi.org/10.1002/adem.200700106.

[25] A. Cibula. 'The mechanism of grain refinement of sand castings in aluminium alloys'. In: *Journal of the Institute of Metals* 76 (1949).

[26] A. Banerji and W. Reif. 'Development of Al-Ti-C grain refiners containing TiC'. In: *Metallurgical Transactions A* 17 (1986), pp. 2127–2137. DOI: https://doi.org/10.1007/BF02645911.

[27] L. Yu and X. Liu. 'Ti transition zone on the interface between TiC and aluminum melt and its influence on melt viscosity'. In: *Journal of materials processing technology* 182 (2007), pp. 519–524. DOI: https://doi.org/10.1016/j.jmatprotec.2006.09.011.

[28] Z. Wang et al. 'Microstructure and its influence on refining performance of AlTiC master alloys'. In: *Materials science and technology* 19 (2003), pp. 1709–1714. DOI: https://doi.org/10.1179/026708303225008257.

[29] Y.M. Lam H. Li T. Sritharan and N.Y. Leng. 'Effects of processing parameters on the performance of Al grain refinement master alloys Al-Ti and Al-B in small ingots'. In: *Journal of Materials Processing Technology* 66 (1997), pp. 253–257. DOI: https://doi.org/10.1016/S0924-0136(96)02536-8.

[30] K. T. Kashyap and T. Chandrashekar. 'Effects and mechanisms of grain refinement in aluminium alloys'. In: *Bulletin of Materials Science* 24 (2001), pp. 345–353. DOI: https://doi.org/10.1007/BF02708630.

[31] K. Svynarenko et al. 'Microstructure and refinement performance of al-ti-C master alloy: Effect of excess ti on the growth and nucleating ability of TiC particles'. In: *Metals and Materials International* 23 (2017), pp. 994–1001. DOI: https://doi.org/10.1007/s12540-017-6716-7.

[32] X. Liu et al. 'Grain refinement and crack inhibition of selective laser melted AA2024 aluminum alloy via inoculation with TiC–TiH2'. In: *Materials Science and Engineering: A* 813 (2021). DOI: https://doi.org/10.1016/j.msea.2021.141171.

[33] M. A. Easton M. X. Zhang P. M. Kelly and J. A. Taylor. 'Crystallographic study of grain refinement in aluminum alloys using the edge-to-edge matching model'. In: *Acta Materiala* 53 (2005), pp. 1427–1438. DOI: http://doi.org/10.1016/j.actamat.2004.11.037.

[34] K. Zhao et al. 'Enhanced grain refinement and mechanical properties of a high–strength Al–Zn–Mg–Cu–Zr alloy induced by TiC nano–particles'. In: *Materials Science and Engineering: A* 806 (2021). DOI: https://doi.org/10.1016/j.msea.2021.140852.

[35] K. Wang et al. 'Nanoparticle–inhibited growth of primary aluminum in Al–10Si alloys'. In: *Acta Materialia* 103 (2016), pp. 252–263. DOI: https://doi.org/10.1016/j.actamat.2015.10.005.

[36] M. Zou et al. 'Microstructure Control and Performance Evolution of Aluminum Alloy 7075 by Nano-Treating'. In: *Scientific Reports* 9 (2019). DOI: https://doi.org/10.1038/s41598-019-47182-9.

[37] M. Sokoluk N. Murali and X. Li. 'Study on aluminum alloy joints welded with nano-treated Al-Mg-Mn filler wire'. In: *Material Letters* 283 (2021). DOI: https://doi.org/10.1016/j.matlet.2020.128739.

[38] F. Widerøe and T. Welo. 'Using contrast material techniques to determine metal flow in screw extrusion of aluminium'. In: *Journal of Materials Processing Technology* 213 (2013), pp. 1007–1018.

[39] O. Reiso K. G. Skorpen E. Mauland and H. J. Roven. 'Novel method of screw extrusion for fabricating Al/Mg (macro-) composites from aluminum alloy 6063 and magnesium granules'. In: *Transactions of Nonferrous Metals Society of China* 24 (2014), pp. 3886–3893.

[40] G. Langelandsvik et. al. 'Development of Al-TiC Wire Feedstock for Additive Manufacturing by Metal Screw Extrusion'. In: *Metals* 10 (2020). DOI: https://doi.org/10.3390/met10111485.

[41] D. B. Williams and C. B. Carter. *Transmission Electron Microscopy: A Textbook for Materials Science*. Springer, 2009.

[42] L. de Broglie. 'Recherches sur la théorie des quanta (Researches on the quantum theory)'. In: *Ann. de Physique* 22 (1925).

[43] N. Yao. *Focused Ion Beam Systems: Basics and Applications*. Cambridge University Press, 2007.

[44] L. A. Giannuzzi and F. A. Stevie. *Introduction to Focused Ion Beams: Instrumentation, Theory, Techniques and Practice*. Springer, 2005.

[45] J. I. Goldstein. *Scanning Electron Microscopy and X-Ray Microanalysis*. Springer, 2018.

[46] J. Zhao et al. 'Grain refinement efficiency in commercial-purity aluminum influenced by the addition of al-4Ti master alloys with varying TiAl3 particles'. In: *Materials* 9 (2016). DOI: https://doi.org/10.3390/ma9110869.

[47] C. Wang et al. 'Formation, microstructure, and performance of laser-welded 6061 Al alloy joint with Ti3AlC2 additive'. In: *Journal of Materials Science* 57 (2022), pp. 8978–8986. DOI: https://doi.org/10.1007/s10853-022-07244-2.

[48] O. Reiso G. Langelandsvik T. Furu and H. J. Roven. 'Effects of iron precipitation and novel metal screw extrusion on electrical conductivity and properties of AA1370 aluminium'. In: *Materials Science and Engineering: B* 254 (2020). DOI: https://doi.org/10.1016/j.mseb.2020.114505.

A Appendix A Full EDS maps

A.1

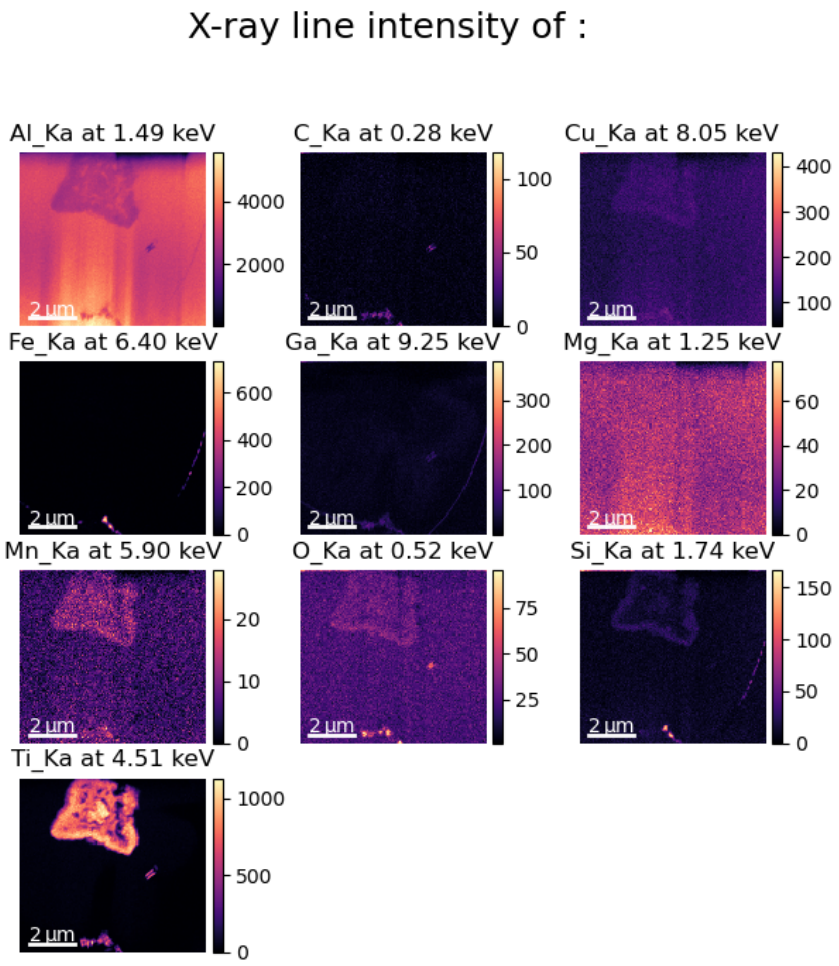

Figure 60: EDS map showing the presence of Al, C, Cu, Fe, Ga, Mg, Mn, O, Si and Ti in a grain with a $TiAl_3$ particle with core and shell.

A.2

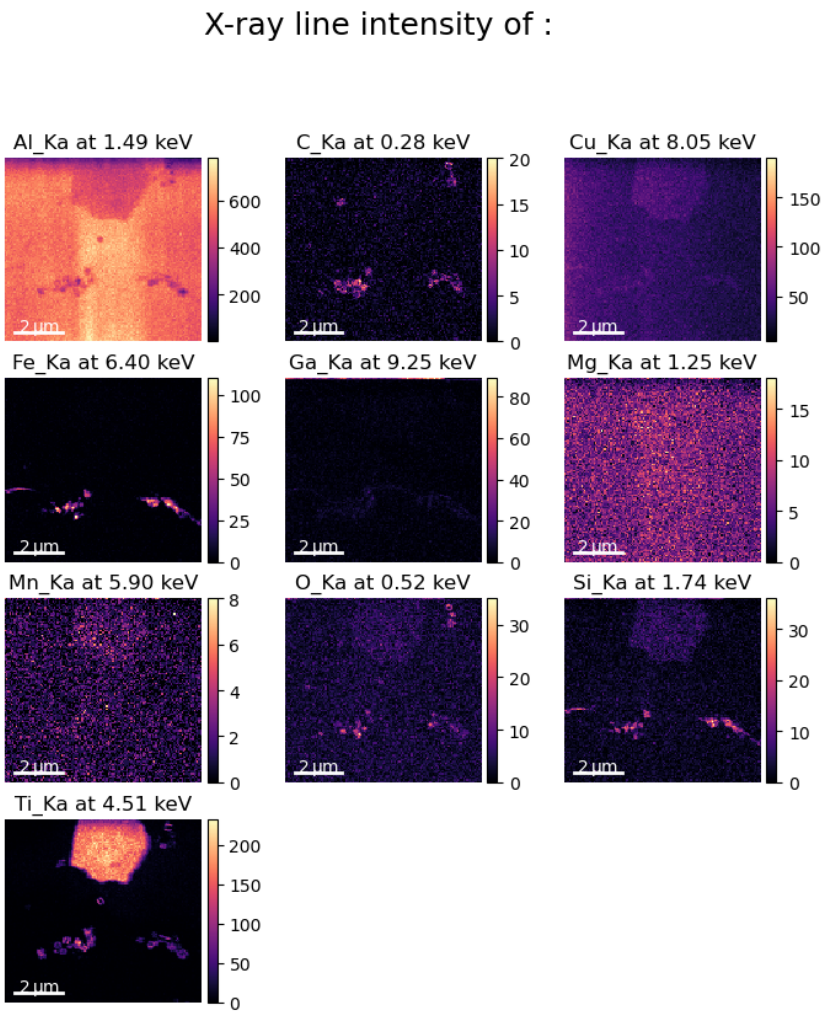

Figure 61: EDS map showing the presence of Al, C, Cu, Fe, Ga, Mg, Mn, O, Si and Ti in a grain with a uniform $TiAl_3$ particle.

A.3

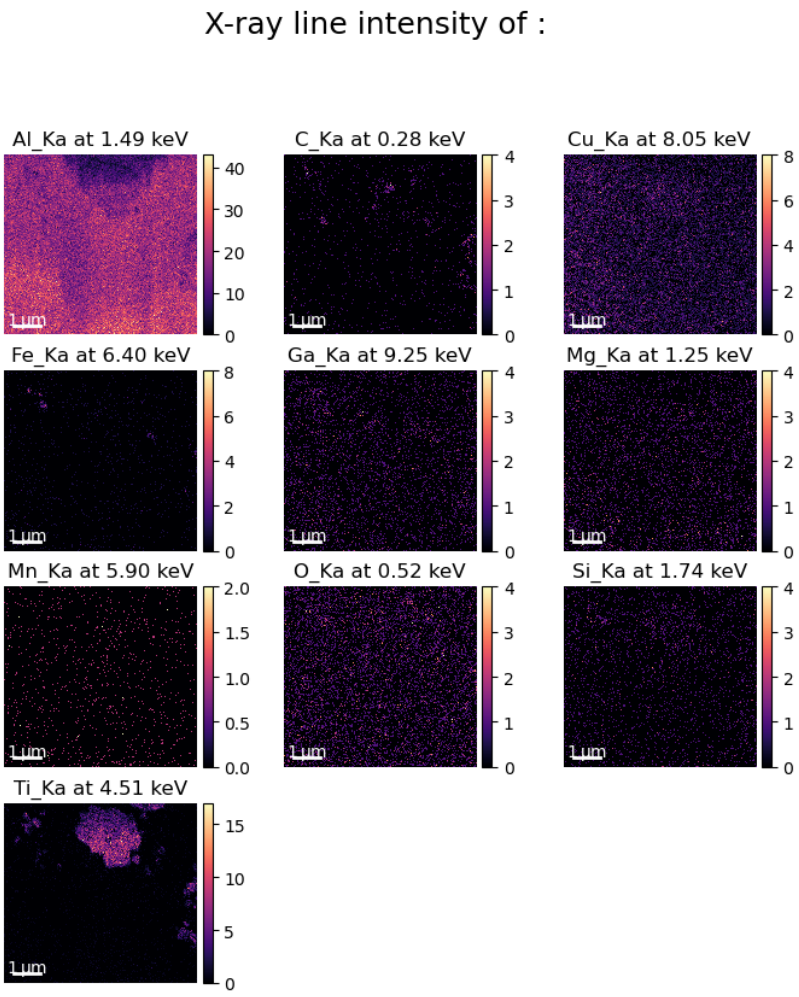

Figure 62: EDS map showing the presence of Al, C, Cu, Fe, Ga, Mg, Mn, O, Si and Ti in a grain with a conjoined $TiAl_3$ particle.

A.4

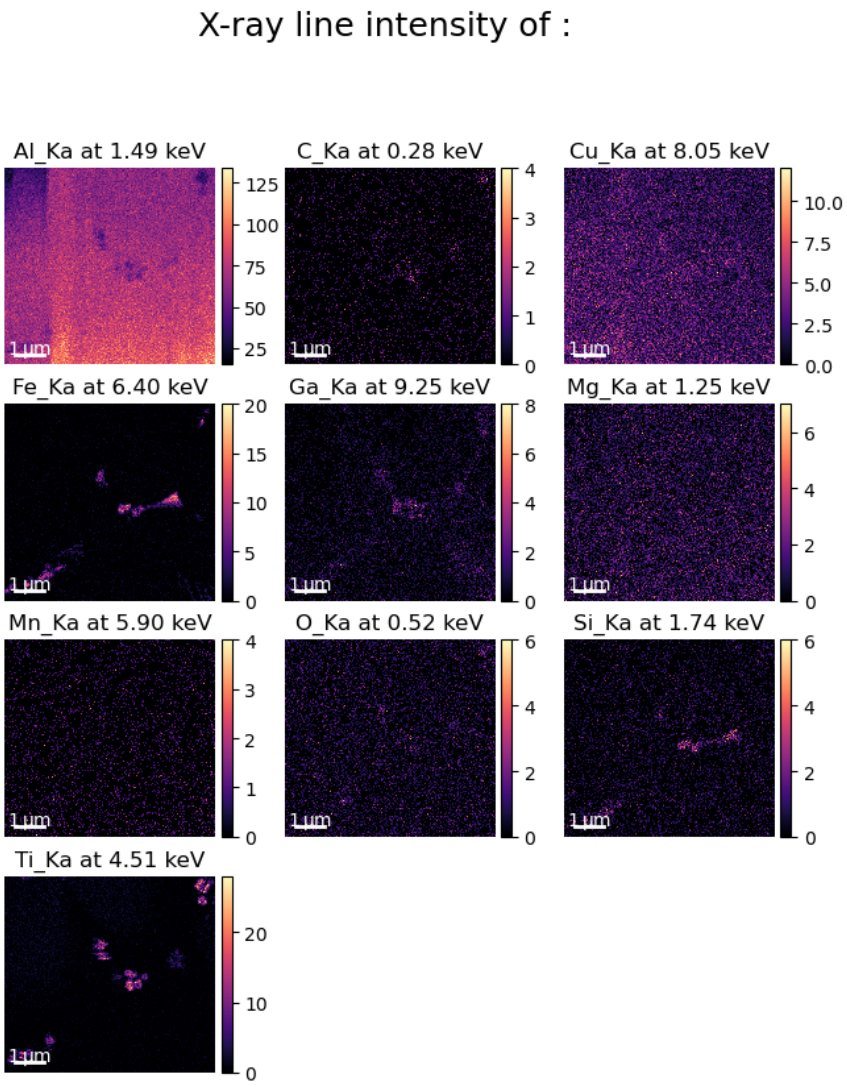

Figure 63: EDS map showing the presence of Al, C, Cu, Fe, Ga, Mg, Mn, O, Si and Ti at a GB conjunction.

A.5

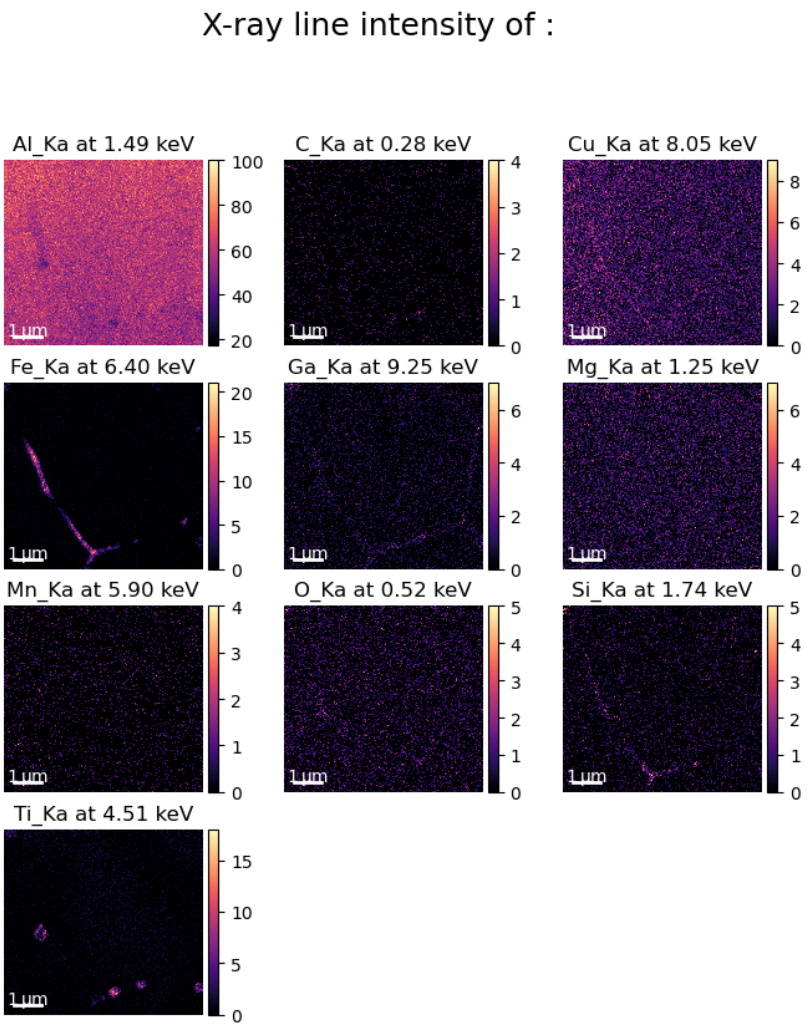

Figure 64: EDS map showing the presence of Al, C, Cu, Fe, Ga, Mg, Mn, O, Si and Ti at a GB conjunction.

B Appendix B Code used for EDS analysis

B.1 Code used for converting the raw data to hdf5

```
##################################################
# Script for exporting EDX maps from AZtec
##################################################

print('Loading Python libraries')

import os
import sys
import hyperspy.api as hs
import numpy as np
import json

print()

path = '.\\'

for arg in sys.argv[1:]:
    if not arg.startswith('-'):
        path = arg.rstrip('\\') + '\\'
        break


transpose = False
if '--transpose' in sys.argv:
    transpose = True

flipx = False
if '--flipx' in sys.argv:
    flipx = True

flipy = False
if '--flipy' in sys.argv:
    flipy = True

def main():
    labels = []
    contents = os.listdir(path)
    for filename in contents:
        fn_spl = filename.split('.')
        if len(fn_spl) == 1:
            continue
        label, filetype = ''.join(fn_spl[:-1]), fn_spl[-1]
        if filetype == 'raw':
            labels.append(label)

    for label in labels:
        print('Processing', label)
        pathlabel = path + '\\' + label
        convert_aztec_to_hdf5(pathlabel, transpose, flipx, flipy)

    if len(labels) == 0:
        print('Couldn\'t find any files to process')


def convert_aztec_to_hdf5(pathlabel, transpose=False, flipx=False, flipy=False):
    """
    Convert AZtec EDX map referenced by `pathlabel` to an `.hdf5` file, and save this file
    to the same folder.
```

```
59
60      The function assumes the following files exist:
61
62      * `.raw`: The raw EDX data.
63      * `.rpl`: Information about the structure of the raw data.
64      * `.emsa`: Sum spectrum, with calibration data and metadata.
65      * `.txt`: Additional metadata.
66
67      :param pathlabel: Full path of the files containing EDX information, including label
68      but without extension. Example: `C:/Users/john/Documents/EDX/A1`. In this case, `A1`
69      is the label and the following files are assumed to exist:  `A1.raw`, `A1.rpl`, `A1.emsa`,
70      `A1.txt`.
71      :param transpose: Whether to interchange the `x` and `y` axes.
72      :param flipx: Whether to make the `x` axis reversed.
73      :param flipy: Whether to make the `y` axis reversed.
74      :return: The `.hdf5`signal which has been created.
75      """
76
77      fn_rpl = pathlabel + '.rpl'
78      fn_emsa = pathlabel + '.emsa'
79      fn_txt = pathlabel + '.txt'
80
81
82      # Load spectrum
83      # The .rpl file uses data from the .raw file.
84      # For some reason, the signal needs to be transposed.
85      s = hs.load(fn_rpl, signal_type='EDS_TEM').T
86
87      # Load sum spectrum
88      # The sum spectrum contains some metadata which is not contained in the .rpl file
89      s_sum = hs.load(fn_emsa, signal_type='EDS_TEM')
90      s.get_calibration_from(s_sum)
91
92      # The EDX detector real time and live time needs to divided by the number of pixels
93      pixels=1
94      for axis in s.axes_manager.navigation_axes:
95          pixels *= axis.size
96      s.metadata.Acquisition_instrument.TEM.Detector.EDS.real_time /= pixels
97      s.metadata.Acquisition_instrument.TEM.Detector.EDS.live_time /= pixels
98
99      # Some properties are not transfered by s.get_calibration_from
100     def transfer(item):
101         s.metadata.set_item(item, s_sum.metadata.get_item(item))
102     transfer('General.date')
103     transfer('General.time')
104
105     # Load metadata
106     meta_np = np.genfromtxt(fn_txt, encoding='utf-8-sig', delimiter=':\t', dtype='str')
107     meta = dict(meta_np)
108
109     # Set properties from metadata
110     ax_ids = ['width', 'height']
111     ax_names = ['x', 'y']
112     sizes_id = ['Image Width', 'Image Height']
113     pxs_id = ['Resolution (Width)', 'Resolution (Height)']
114
```

```
    for ax_id, ax_name, size_id, px_id in zip(ax_ids, ax_names, sizes_id, pxs_id):
        ax = s.axes_manager[ax_id]
        size, size_unit = split_property(meta[size_id])
        px, px_unit = split_property(meta[px_id])
        ax.scale = float(size.replace(',', '.')) / float(px)
        ax.units = size_unit
        ax.name = ax_name

    if transpose:
        s = s.transpose(signal_axes=[2], navigation_axes=[1, 0])
        s.axes_manager[0].name = ax_names[0]
        s.axes_manager[1].name = ax_names[1]

    if flipx:
        s.data = np.flip(s.data, axis=1)

    if flipy:
        s.data = np.flip(s.data, axis=0)

    s.save(pathlabel, extension='hdf5', overwrite=True)

    return s


def split_property(text):
    lim = None
    for i in range(len(text) - 1, -1, -1):
        if text[i].isnumeric():
            lim = i + 1
            break
    return text[:lim], text[lim:]


def get_index(string):
    s = ".".join(string.split('.')[:-1]).split('-')[0]
    start = -1
    for i in range(len(s)-1, -1, -1):
        if not s[i].isdigit():
            start = i
            break
    return s[start+1:]


def load_json(path):
    with open(path) as file:
        return json.load(file)

main()

input('Press Enter to exit')

```

B.2 Code used for plotting EDS maps

```
%matplotlib qt5
```

```
import numpy as np
import matplotlib.pyplot as plt
import hyperspy.api as hs
#import pyxem as pxm
import os
```

Python

```
filename = 'Samplename'
EDS = hs.load(filename+'.hdf5', signal_type="EDS_TEM")
EDS_avg = hs.load(filename+'.emsa')
```

Python

```
x_ax = EDS.axes_manager[0].size
y_ax = EDS.axes_manager[1].size
while (x_ax%4):
    x_ax -=1
while (y_ax%4):
    y_ax -= 1
print(x_ax, y_ax)

EDS = EDS.inav[0:x_ax, 0:y_ax]
EDS
```

Python

```
EDS = EDS.rebin(scale=(4,4,1))
x_rebin = EDS.axes_manager[0].size
y_rebin = EDS.axes_manager[1].size
EDS
```

Python

```
EDS.add_elements(['Ti', 'Al', 'C', 'Cu', 'Mn', 'Mg', 'O', 'Si', 'Ga', 'Fe'])
eds_maps = EDS.get_lines_intensity()
hs.plot.plot_images(eds_maps, axes_decor='off', scalebar='all',cmap='magma')
```

Python

B.3 Code for creating line scans

```
def getHorizontalLineTrace(Xray, EDSmap, top, bottom, kVrange):
    ''''
    Parameters
    -------
    Xray : Characteristic Xray energy of element of interest
    EDSmap : EDS map data, example: <EDSTEMSpectrum, title: , dimensions: (128, 120|2048)>
    top : top y coord to include in line scan
    bottom : bottom y coord to include in line scan
    kVrange : integration window for counting Xrays

    Returns
    -------
    lineTrace : 1D array with counts
    '''
    EDS_line = EDSmap.inav[:,top:bottom].sum(axis=1)
    kV_scale = EDS_line.axes_manager[1].scale
    offset = EDS_line.axes_manager[1].offset

    Xray_i = int(Xray/kV_scale + abs(offset/kV_scale))

    start = Xray - kVrange
    stop = Xray + kVrange

    EDS_Xray = EDS_line.isig[start:stop]
    lineTrace = EDS_Xray.sum(axis=1)
    return lineTrace

def presentLineTraces(EDSmap, Xrays, Xray_names, top, bottom, kVranges):
    ''''
    Parameters
    -------
    EDSmap : EDS map data, example: <EDSTEMSpectrum, title: , dimensions: (128, 120|2048)>
    Xrays : 1D array of characteristic Xray energies of elements of interest
    Xray_names : 1D array of elements included in Xrays
    top : top y coord to include in line scan
    bottom : bottom y coord to include in line scan
    kVrange : integration window for counting Xrays
    '''
    EDSmap.plot()
    roi = hs.roi.RectangularROI(left=0, top=top, right=EDSmap.axes_manager[0].size, bottom=bottom)
    roi.add_widget(EDSmap)
    EDS_lineTrace = EDSmap.inav[:,top:bottom].sum(axis=1)
    EDS_lineTrace.plot()

    plt.figure()
    xaxis = np.arange(0, EDS_lineTrace.axes_manager[0].size, 1)*EDS_lineTrace.axes_manager[0].scale
    for i, Xray in enumerate(Xrays):
        integration_window = hs.roi.SpanROI(left=Xrays[i]-kVranges[i], right=Xrays[i]+kVranges[i])
        integration_window.add_widget(EDS_lineTrace, axes=1)
        plt.plot(xaxis, getHorizontalLineTrace(Xray, EDSmap, top, bottom, kVranges[i]), label=Xray_names[i])
    plt.xlabel('Position ['+EDS_lineTrace.axes_manager[0].units+']')
    plt.ylabel('Counts [#]')
    plt.legend()
```

```
EDS.plot()
roi = hs.roi.RectangularROI(left=0, top=6, right=EDS.axes_manager[0].size*EDS.axes_manager[0].scale-0.1, bottom=7.78)
roi.add_widget(EDS)
```

```
roi
```

```
Xray_Ti = hs.material.elements.Ti.Atomic_properties.Xray_lines.Ka['energy (keV)']
Xray_Al = hs.material.elements.Al.Atomic_properties.Xray_lines.Ka['energy (keV)']
Xray_C = hs.material.elements.C.Atomic_properties.Xray_lines.Ka['energy (keV)']

Xrays = np.array([Xray_Ti, Xray_Al, Xray_C])
Xray_names = np.array(['Ti', 'Al', 'C'])
kVranges = np.array([0.15, 0.15, 0.05])
# I added this because the C peak is narrower and closer to other peaks than Al and Ti
presentLineTraces(EDS, Xrays, Xray_names, roi[2], roi[3], kVranges)
```

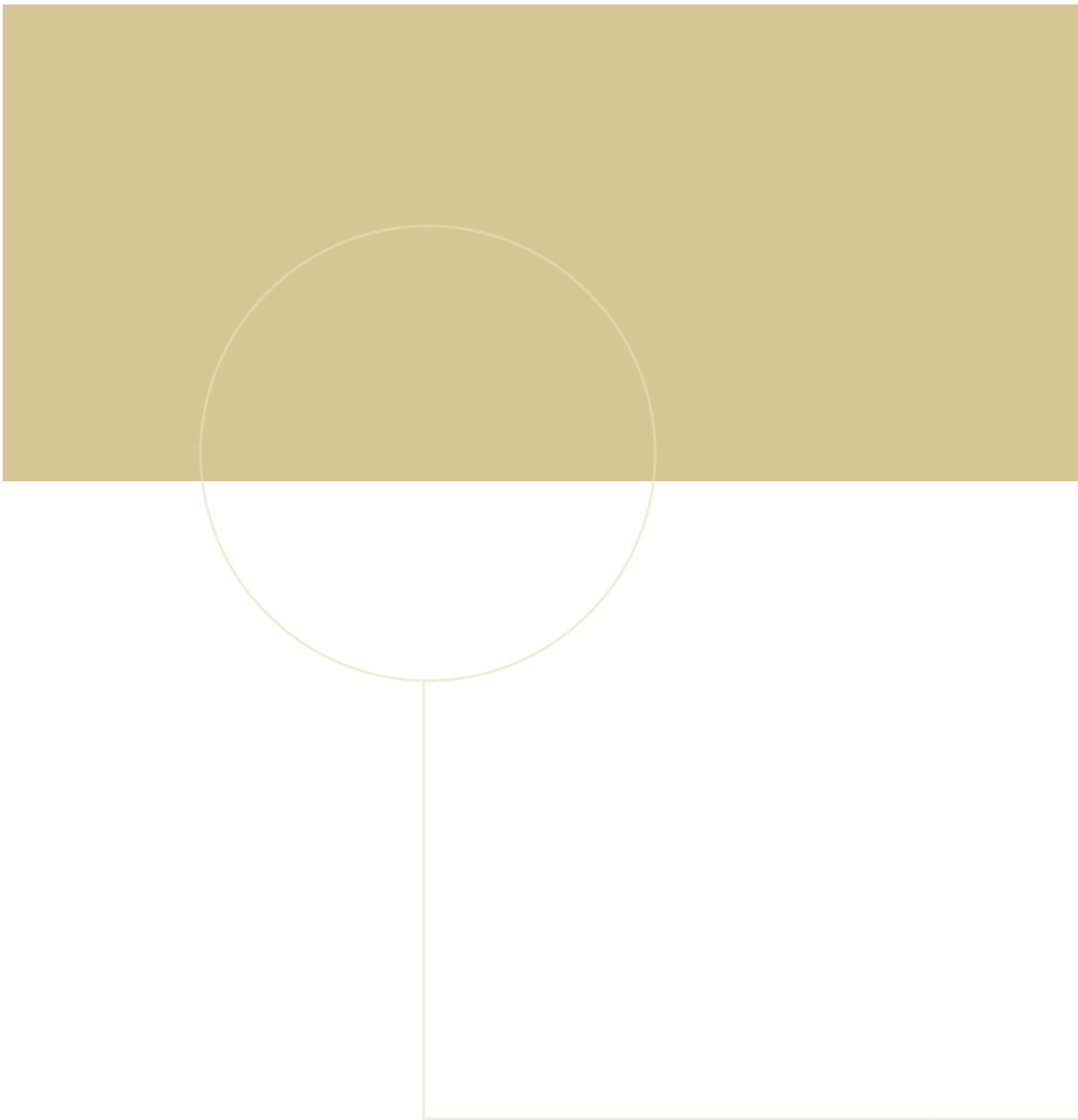

NTNU

Norwegian University of
Science and Technology